Scalar-Induced Gravitational Waves from Supercool(ed) Cosmological Phase Transitions

Masterarbeit

zur Erlangung des akademischen Grades
Master of Science (M.Sc.) in Physik
am Institut für Theoretische Physik
der Goethe-Universität Frankfurt am Main

vorgelegt von

Tamara Caldas Cifuentes

aus Mörfelden-Walldorf

am 5. März 2026

Erstgutachterin: Prof. Dr. Laura Sagunski
Zweitgutachter: Dr. Daniel Schmitt

Abstract

In this work, we explore the unique gravitational wave signatures from a supercooled, QCD-sourced tachyonic phase transition in the early Universe within the Classically Conformal $\mathrm{B}-\mathrm{L}$ extension of the Standard Model of Particle Physics. In a particular region of the parameter space spanned by the gauge coupling g_{BL} and the gauge boson mass $m_{\mathrm{Z}'}$, the QCD-induced tachyonic instability amplifies scalar fluctuations, destabilizing the false vacuum and driving a tachyonic phase transition via spinodal decomposition rather than the usual bubble nucleation mechanism. Tracing the evolution of these fluctuations in their linear *or* quantum regime, we calculate the resulting curvature perturbations, and gravitational wave energy density spectra associated to stochastic gravitational wave backgrounds. By comparing these predictions with the sensitivities of upcoming GW observatories, we reveal how future gravitational wave measurements could probe this phenomenologically-rich Standard Model extension.

Zusammenfassung

In dieser Arbeit untersuchen und analysieren wir die einzigartigen Gravitationswellensignale im Kontext der klassisch konformen $\mathrm{B}-\mathrm{L}$-Erweiterung des Standardmodells, die während der Dynamik eines supergekühlten, tachyonischen Phasenübergangs im frühen Universum entstehen. In bestimmten Bereichen des Parameterraums, aufgespannt durch die Kopplungsstärke g_{BL} und die Bosonmasse $m_{\mathrm{Z}'}$, werden durch eine QCD-induzierte tachyonische Instabilität im effektiven Potential skalare Fluktuationen amplifiziert. Diese destabilisieren das falsche Vakuum und treiben einen tachyonischen Phasenübergang durch spinodale Phasenzerlegung voran, anstelle der üblichen Vakuum-Blasenbildung und -kollisionen. Durch die Berechnung der Entwicklung dieser Fluktuationen in ihren linearen Regimen berechnen wir die daraus resultierenden Krümmungsfluktuationen und Gravitationswellenspektren. Durch den Vergleich dieser Vorhersagen mit den Empfindlichkeiten zukünftiger Observatorien zeigen wir, wie wir mit Hilfe potentieller künftiger Messungen der hier berechneten stochastischen Gravitationswellenhintergründe diese phänomenologisch interessante Standardmodelerweiterung falsifizieren können.

Selbstständigkeitserklärung

Hiermit erkläre ich, dass ich die Arbeit selbstständig und ohne Benutzung anderer als der angegebenen Quellen und Hilfsmittel verfasst habe. Alle Stellen der Arbeit, die wörtlich oder sinngemäß aus Veröffentlichungen oder aus anderen fremden Texten entnommen wurden, sind von mir als solche kenntlich gemacht worden. Ferner erkläre ich, dass die Arbeit nicht - auch nicht auszugsweise - für eine andere Prüfung verwendet wurde.

Mörfelden-Walldorf, den 5. März 2026

Tamara Caldas Cifuentes

Acronyms

B-L Baryon number minus lepton number

BD Bunch-Davies

BSM Beyond Standard Model

dofs degrees of freedom

EOM equation of motion

EOS equation of state

EWPT Electroweak phase transition

GW Gravitational wave

QFT Quantum field theory

SGWB Stochastic Gravitational Wave Background

SM Standard Model of Particle Physics

SSB Spontaneous symmetry breaking

TQFT Thermal quantum field theory

TTG Transverse-traceless (TT) gauge

VEV Vacuum expectation value

w.r.t. with respect to

Contents

Chapter 1

Theoretical Framework

Firstly, we will elaborate the basic concepts necessary to understand the research objective of this work that lies at the topical intersection of gravity theory, cosmology, and particle physics. Starting from our current understanding of the Universe as well as the theoretical description of gravitational waves, we will dive into elements of statistical physics (classical and quantum) to understand the nature and phenomenology of *cosmological phase transitions*. After introducing our BSM model of interest, the (B − L)-SM extension, we will show how we can compute possibly future-detectable stochastic gravitational wave backgrounds generated from an inflationary phase that exhibits a tachyonic instability for the fluctaution modes.

Note that all equations make use of the natural unit convention, i.e., $c = \hbar = 1$.

1.1 Elements of General Relativity & Cosmology

Einstein's theory of General Relativity (GR) has proven to be a highly successful theory to describe the dynamic interaction of matter or *energy* with spacetime. It not only accounts for the formation and dynamics of astrophysical objects like stars, planets and black holes we observe in outer space; it is also the underlying framework of our current understanding of how the Universe came about and potential gravitational wave echoes from many different process during its evolution.

The most fundamental equation is the *Einstein equations* ,

$$G_{\mu\nu} = R_{\mu\nu} - \frac{1}{2} R g_{\mu\nu} + \Lambda g_{\mu\nu} = 8\pi G T_{\mu\nu} \tag{1.1}$$

which links the energy-momentum tensor $T_{\mu\nu}(\{\phi_i\}, \{\partial\phi_i\})$ of our matter contents, i.e., classical/quantum fields $\{\phi_i\}$, with the Einstein tensor $G_{\mu\nu}(g_{\mu\nu}\,, \partial g_{\mu\nu}\,, \partial^2 g_{\mu\nu})$ which describes of curvature of the spacetime manifold whose geometry is defined through the metric tensor $g_{\mu\nu}$. The term including the *cosmological constant* Λ was initially not part of the Einstein equations, but has been added later due to the observation that confirmed today's accelerated expansion of the Universe (see Subection 1.1.2). A specific physical

system is then defined by the choice of the metric $g_{\mu\nu}$, which may or may not exhibit certain symmetries, as well as the matter/energy content in the spacetime encoded in $T_{\mu\nu}$. The concrete form of can also be written by the *line element* $ds^2 \equiv g_{\mu\nu}\, dx^\mu\, dx^\nu$, where $\{x^\mu\}$ is a chosen set of coordinates.

1.1.1 Existence and Origin of Gravitational Waves

Since the dynamics of the energy contents influence the curvature of the spacetime and vice versa, we can think about the fate of small metric perturbations. Insights are obtained through the perturbative study of a flat Minkowski metric up to linear order by introducing

$$g_{\mu\nu} \;=\; \eta_{\mu\nu} + h_{\mu\nu}\,, \quad \eta_{\mu\nu} = \mathrm{diag}(-1,1,1,1)\,, \tag{1.2}$$

where $\eta_{\mu\nu}$ is the flat Minkowski metric and $h_{\nu\mu}$ is a small symmetric ($|h_{\mu\nu}| \ll 1\,,\ h_{\mu\nu} = h_{\nu\mu}$) perturbation upon $\eta_{\mu\nu}$. Plugging this into Eq. (1.1), we find a wave-like equation of motion for the metric perturbation

$$\Box \bar{h}_{\mu\nu} = \left[-\partial_t^2 + \nabla^2\right] \bar{h}_{\mu\nu} = -16\pi G T_{\mu\nu}\,, \tag{1.3}$$

in whose derivation we made use of the tensor equation's gauge freedom.[1] Note that in vacuum (the absence of a source term $T_{\mu\nu}$), we obtain plane wave solutions. This is the reason why we call its solutions *gravitational waves* (GWs). After their first derivation in 1916 by Albert Einstein [1,2], it took almost exactly 100 years to detect them for the first time [3]. The general solution to Eq. (1.3) however is

$$\bar{h}_{\mu\nu}(t,\boldsymbol{x}) = 4G \int d^3\boldsymbol{y}\; \frac{T_{\mu\nu}(t_r,\boldsymbol{y})}{|\boldsymbol{x}-\boldsymbol{y}|}\,, \tag{1.4}$$

where $t_r = t - |\boldsymbol{x}-\boldsymbol{y}|$ is the retarded time, i.e. the time at which at the position $\boldsymbol{y}$ the gravitational wave was sourced.[2] Its structure becomes even more evident in the limit where $r = |\boldsymbol{x}| \gg d$ where d is the size of the source such that $|\boldsymbol{x}-\boldsymbol{y}| \approx r - \boldsymbol{x}\cdot\boldsymbol{y}/r$ and hence

$$\bar{h}_{ij}(t,\boldsymbol{x}) \approx \frac{4G}{r}\int_\Sigma d^3y\; T_{ij}(t-r,\boldsymbol{y}) = \frac{2G}{r}\frac{d^2 I_{ij}}{dt^2}(t_r)\,, \quad \bar{h}_{\mu 0} = \text{const.}\,, \tag{1.5}$$

$$I_{ij}(t_r) = \int_\Sigma d^3y\; T_{00}(t_r,\boldsymbol{y})\; y_i y_j = \int_\Sigma d^3y\; \rho(t_r,\boldsymbol{y})\; y_i y_j\,, \tag{1.6}$$

where $I_{ij}(t)$ is called the *mass quadrupole moment* of the source, $\rho(t,\boldsymbol{y})$ is the energy density of the source, and Σ is the volume enclosing the (localized) source. Evidently,

[1] More precisely, we have introduced the trace-reversed metric perturbation $\bar{h}_{\mu\nu} = h_{\mu\nu} - \frac{1}{2}\eta_{\mu\nu}$ and later the Lorenz gauge where $0 = \partial_\nu h^{\mu\nu} - \frac{1}{2}\partial^\mu h$.

[2] The appearance of the retarded time is a manifestation of the existence of the speed of light as the maximum velocity with which information can propagate through spacetime.

gravitational waves are being sourced by dynamical non-vanishing *spatial* components of the energy-momentum tensor, or differently put, one needs anisotropies is $T_{\mu\nu}$ to generate GWs. Note that this result is also consistent with Birkhoff's theorem [4] stating that the external gravitational field of a source with a spherically symmetric mass (or energy) distribution is equal to the one of a point particle with the same total mass, i.e., the exterior solution must be of Schwarzschild-type and is thus asymptotically *flat*.

Gravitational Waves, and How and Where to find them

As can be directly seen in to Eq. (1.3), gravitational waves are time-dependent and periodic tensor perturbations of the spacetime metric. This means that (proper) lengths change periodically whenever a gravitational wave passes by, since the spacetime is stretched and compressed either in a cross- or plus-patterns (or a linear combination of both) corresponding to the two possible tensor perturbation polarisations $\{+, \times\}$. Therefore, the key idea of gravitational wave detection is to observe this change of lengths as it reflects in the change of the time interval that light would need to travel a certain distance. The common detection techniques make use of this principle in their own way: while ground- (e.g., LIGO [5], VIRGO [6], KAGRA [7]) and future space-based *interferometers* (e.g., LISA [8]) see deviations in the arrival times of laser beams travelling a fixed distance through their interference pattern, so-called *pulsar timing arrays* (e.g., NANOGrav [9], EPTA [10], APTA [11], InPTA [12], IPTA [13]) compare and try to correlate the deviations of arrival times of the periodic light pulses from pulsars in outer space, detected with the help of ground-based radio telescopes.

Types of Gravitational Wave Signals

Generally, one distinguishes between three qualitatively distinct types of gravitational wave signals, each of which can be generated by distinct sources:

I *Transient signals* are time-dependent and come from resolved sources of astrophysical origin, e.g., compact binary coalescences (CBC) (inspiral and merger of two compact objects), and pulsars with an imperfect surface violating spherical symmetry. The signal of CBCs follows a very characteristic evolution, described as the *chirp signal*. It consists of a first simple approximately sinusodial *inspiral* part, which is then followed by a steep rise in amplitude and frequency in the *merger* part and eventually ends with the *ringdown* phase. Analysing this specific waveform gives us not only information about the size and mass of the coalescencing objects, but also potentially their inner structure (if they are not black holes).

II *Stochastic Gravitational Wave Backgrounds (SGWB)* are stationary and may originate from yet unresolved astrophysical sources, e.g., from unresolved black hole binary coalescences, or can also be of cosmological origin, e.g., generated during inflationary periods, or from anisotropies-producing cosmological phase transitions. The shape of the spectrum exhibits a peak at a specific scale, which is related to

a characteristic time scale of the microphysical process in the very early Universe. Also here we find that the analysis of the GW spectrum (peak amplitude and frequency, slopes next to the peak) yields valuable information about the underlying microphysics.

III *Burst signals* are time-dependent, hard to model, do not fit into the first two categories and originate from violent events such as supernovae.

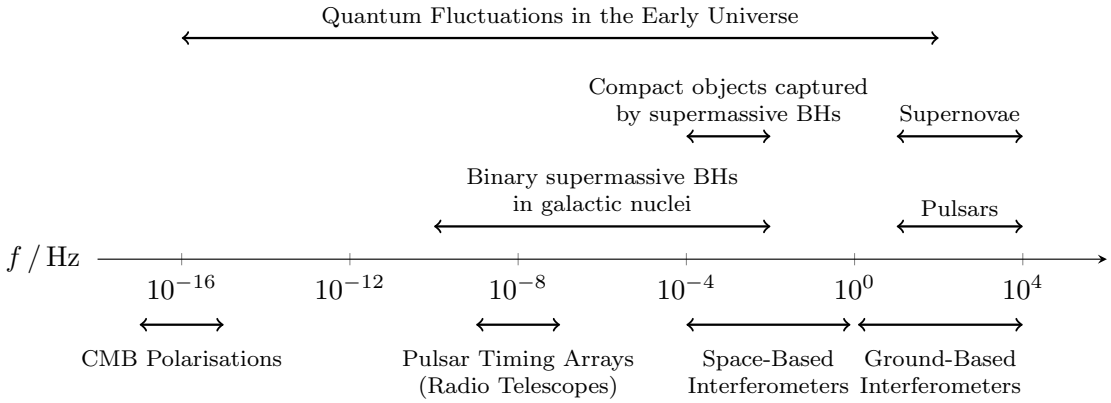

Figure 1.1: Characteristic frequency domains of different gravitational wave detectors and sources. Figure adopted from [14].

1.1.2 Cosmology of our Universe

From observation of our night sky over millenia, one of the many things we have learned about our Universe is that it seems to conform with the underlying concept of the *cosmological principle*: on large scales of about $\mathcal{O}(100\,\mathrm{Mpc})$, we find that the matter content is isotropically and homogeneously distributed. A metric for our Universe's spacetime should be constrained by these symmetries, and it turns out that a suitable choice is the *Friedmann-Lemaître-Robertson-Walker (FLRW)* metric,

$$ds^2 = dt^2 - a(t)^2 \left[\frac{dr^2}{1-kr^2} + r^2 d\Omega^2\right] = dt^2 - a(t)^2 d\Sigma_k^2\,, \tag{1.7}$$

which describes three-dimensional maximally symmetric spatial slices $\Sigma_k(t)$ with intrinsic curvature $k = \{0, \pm 1\}$ whose evolution is solely dictated by the *scale factor* $a(t)$, i.e., the extrinsic curvature. Different k-values yield different geometries of our spatial slices: $\Sigma(k=0)$ has vanishing curvature (*flat*), $\Sigma(k=+1)$ has positive curvature (*spherical*), and $\Sigma(k=-1)$ has negative curvature (*hyperboloidal*).[3]

[3]We also distinguish these Universe models as *flat* Universe ($k=0$), *closed* Universe (k=+1), and *open* Universe ($k=-1$).

The theoretical description of our Universe is completed by treating the energy contents as *perfect fluids* in which case the energy-momentum tensor is given by $T_{\mu\nu} = \mathrm{diag}(\rho, -p, -p, -p)$, where $\rho = \sum_i \rho_i$ and $P = \sum_i P_i$ are the energy density and pressure of all energy components. Using this specific spacetime geometry and energy content ansatz yields the specific form of Eqs. (1.1) also called the *Friedmann equations*,

$$H^2 = \left(\frac{\dot{a}}{a}\right)^2 = \frac{8\pi G}{3}\rho - \frac{k}{a^2} = \frac{\rho}{3M_{\mathrm{pl}}^2} - \frac{k}{a^2} + \frac{\Lambda}{3}\,, \tag{1.8a}$$

$$\dot{H} + H^2 = \left(\frac{\ddot{a}}{a}\right) = -\frac{4\pi G}{3}\left(\rho + 3P\right) + \frac{\Lambda}{3}\,, \tag{1.8b}$$

which describe the evolution of the scale factor depending on the energy content in the Universe[4]. The normalized derivative $H(t) = (\dot{a}/a)(t)$ is called the *Hubble parameter*. From the conservation of energy and momentum, i.e., $0 = \nabla_\mu T^\mu_\nu$, we also get the *continuity equation*

$$0 = \dot{\rho}_i + 3\left(\frac{\dot{a}}{a}\right)\left(\rho_i + P_i\right) = \dot{\rho}_i + 3H\left(1 + w\right)\rho_i\,, \tag{1.9}$$

from which we obtain the direct relation between the scale factor a and the energy density ρ_i of the i-th energy species, if we are able to provide an equation of state (EOS) $P_i \equiv w_i \rho_i$ ($w \simeq$ const.) for it. The quantity w is now called the *EOS parameter*. For the standard energy forms (matter (dust-like), radiation, dark energy), we find

$$\rho(a) \propto \begin{cases} a^{-3}\,, & w = 0 \qquad \text{(matter energy density)} \\ a^{-4}\,, & w = \frac{1}{3} \qquad \text{(radiation energy density)} \\ a^{0}\,, & w = -1 \qquad \text{(dark energy density)} \end{cases} \tag{1.10}$$

where $\rho_{i,0}$ is the observed present-day value for the i-th species' energy density. Inserting these cases into Eq. (1.8a), we respectively find

$$a(t) \propto \begin{cases} t^{2/3} & w = 0\,, \qquad \text{(matter energy density)} \\ t^{1/2} & w = \frac{1}{3}\,, \qquad \text{(radiation energy density)} \\ e^{H_0 t} & w = -1\,. \qquad \text{(dark energy density)} \end{cases} \tag{1.11}$$

This already shows that the special case of exponential and thus accelerated spacetime expansion is realized when a constant energy density is dominating the other energy components (see also Section 1.1.3). This is also referred to as *de Sitter spacetime*.

[4]We will henceforth neglect the cosmological constant term, since we will focus on processes in the very early Universe where it plays a subdominant role.

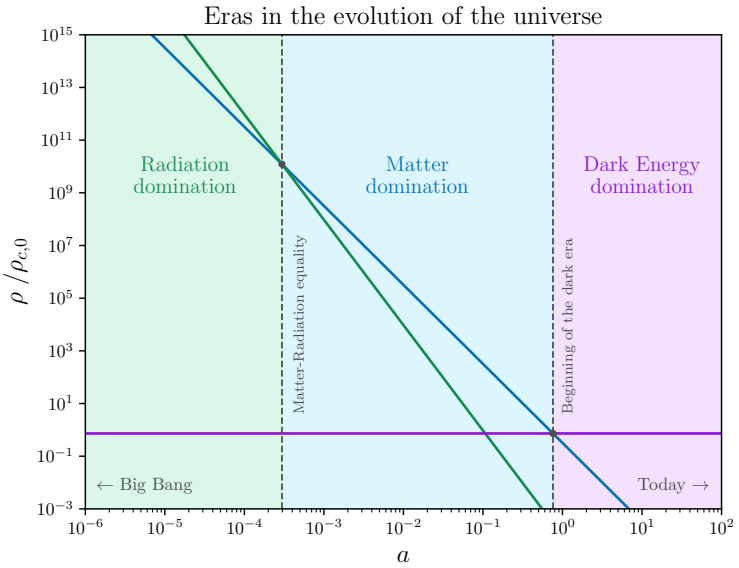

Figure 1.2: The different cosmic eras that are believed to have shaped the history of our universe according to recent measurements of the present-day dimensionless density parameters $\{\Omega_r, \Omega_m, \Omega_\Lambda\}$. While early times where dominated by the total radiation energy density, the universe transitioned to a matter-dominated period. The current dark era followed thereafter and is dominated by the yet unknown dark energy. Figure adopted from [17].

To get a more practical form of Eq. (1.8a), we may define the dimensionless density parameters $\Omega_i(t) = (\rho_i/\rho_{\text{crit}})(t)$ where $\rho_{\text{crit}}(t) = (8\pi G/3H^2)(t)$, such that we can rewrite

$$\frac{H^2}{H_0^2} = \sum_i \Omega_{i,0} \left(\frac{a_0}{a}\right)^{3(1+w_i)} \tag{1.12}$$

$$= \Omega_{r,0} \left(\frac{a_0}{a}\right)^4 + \Omega_{m,0} \left(\frac{a_0}{a}\right)^3 + \Omega_{k,0} \left(\frac{a_0}{a}\right)^2 + \Omega_{\Lambda,0}\,, \tag{1.13}$$

where in the derivation we divided Eq. (1.8a) by itself evaluated at the present time t_0. We have just found a way of expressing the evolution equation of our Universe's spacetime in terms of present-day observables $\Omega_i(t_0)$ that we can infer e.g., from precision measurements of the anisotropies in the the Cosmic Microwave Background (CMB) [15, 16]. The latter suggest that $k \simeq 0$ in our Universe [15], we will henceforth neglect the corresponding term in the Friedmann equations. With the experimental data at hand, we can not only draw a picture of the cosmological history until today but predict its evolution in the future.

One of the biggest puzzles in modern physics is the strong indirect evidence of *dark matter* [18], a yet unknown form of matter that does not interact with photons and is thus

not directly observable, but must be present due its gravitational influence visible in, e.g., *gravitational lensing* [19] and *galaxy rotation curve* measurements [20]. It is therefore appropriate to split $\Omega_{m,0} = \Omega_{bm,0} + \Omega_{dm,0}$, where we account for the common *baryonic matter* and the (cold) *dark matter*. This addition to our energy content completes the so-called Λ*CDM-model* or *Standard Model of Cosmology*.

A Brief History of our Universe Today we believe that our Universe began with a *Hot Big Bang (BB)*, after which it has subsequently expanded and cooled down. A proposed early period of inflation right after the BB is believed to resolve the main tensions of the ΛCDM-model (see next section). While initially all four fundamental forces (gravity, strong, weak and electromagnetic force) were believed to be unified, perhaps in a *Theory of Everything*, there is strong evidence that the evolution of the cosmic history has been driven by a sequencce of cosmological phase transitions (see Sec. 1.4) through spontaneous symmetry breaking, yielding the present state of the Universe whose microphysics are well-described by the Standard Model of Particle Physics (SM). Chronologically, this evolution includes a hypothesised decoupling of gravity from the other forces around $T \sim 10^{19}, \mathrm{GeV}$, followed by a hypothesised Grand-Unified Theory (GUT) phase transition at $T \sim 10^{15}, \mathrm{GeV}$, separating the strong from the electroweak force. At some point, a period of *cosmic inflation* is assumed to have caused exponential expansion and thus be able to resolve the main tensions within the ΛCDM model (see Sec. 1.1.3). A baryogenesis mechanism must then have generated the small matter–antimatter asymmetry responsible for the observed dominance of matter over antimatter today. Around $T \sim 100, \mathrm{GeV}$, the *electroweak phase transition* separated the electroweak force into the weak and electromagnetic interactions and generated the SM particle masses through the Higgs mechanism [21, 22]. At $T \sim 100\,\mathrm{MeV}$, the *QCD confinement phase transition* occurred, during which quarks formed bound states such as protons, neutrons, and mesons. The latter two phase transitions are crossover transitions within the SM [23,24]. This was followed by *Big Bang nucleosynthesis (BBN)* at $T \sim 100\,\mathrm{keV}$, when the first light nuclei, mainly H and He, were formed. Later, at $T \sim 0.3\,\mathrm{eV}$, *recombination* produced neutral hydrogen and helium atoms, and the subsequent decoupling of photons generated the *Cosmic Microwave Background (CMB)*. Finally, after the epoch of matter–dark energy equality, the Universe entered a phase of accelerated (approximately exponential) expansion that continues until today.

1.1.3 The Concept & Implications of Inflation

Despite its success in describing the evolution of our Universe so far, the ΛCDM-model is also challenged by a number of observations, leading to open questions that renders it incomplete.
One such example is the *Horizon problem*: The ΛCDM-model predicts that the spacetime consisted of many casually disconnected (*Hubble*) patches way in the past. These patches are spacetime regions about the size of the *particle horizon* $\chi_p(t)$ (or the *comoving Hubble*

horizon or radius $r_H(t)$)[5]

$$\chi_p(t) \propto r_H(t) = \frac{1}{a(t)H(t)}\,, \tag{1.14}$$

inside which causal interactions between two observers are possible, such that physical processes like thermalisation of particle species may occur. If this was not a given at early times, how can the CMB spectrum be so (largely) isotropic?

A resolution of this issue was proposed by introducing a new cosmological era called *inflation* in which the comoving Hubble radius *shrinks*, i.e.,

$$\frac{dr_H(t)}{dt} = \frac{d}{dt}\left((aH)^{-1}\right) < 0\,, \tag{1.15}$$

which effectively gives the disconnected patches more time before recombination to be in causal contact with each other. We can learn about how or by what energy content such a period can be realized by translating the shrinking of the Hubble radius into equivalent conditions [25]:

$$\frac{d}{dt}\left((aH)^{-1}\right) < 0 \;\Leftrightarrow\; \begin{cases} -\ddot{a}/(\dot{a})^2 < 0 & \text{(Accelerated expansion)} \\ \varepsilon \equiv -\dot{H}/H^2 < 1 & \text{(Slowly varying } H\text{)} \\ w = P/\rho < -1/3 & \text{(Negative EOS parameter)} \\ \left|\frac{d\ln(\rho)}{d\ln(a)}\right| = 2\varepsilon < 1 & (\approx \text{Constant energy density}) \end{cases} \tag{1.16}$$

Hence, for an inflationary phase in the early Universe we would need a dominant energy component which then has an (almost) constant energy density and thus negative pressure, leading to a quasi-exponential or *quasi-de Sitter* expansion of the spacetime with $H \approx$ const. when comparing to the dark energy case in Eq. (1.11). The newly introduced variable ε is also called the *slow-roll parameter* and is a crucial quantity when describing inflationary dynamics. Note that we recover a perfect de Sitter Universe when $\varepsilon \to 0$.

Inflation via a scalar *inflaton* field

Let us suppose that inflation is driven by a new scalar *"inflaton"* field $\Phi(t, \boldsymbol{x})$ with the above explained properties. The perfect fluid ansatz requires the field to be homogeneous and isotropic, i.e. we may decompose our field into a background field and fluctuations upon it, i.e.,

$$\Phi(t, \boldsymbol{x}) = \varphi(t) + \delta\phi(t, \boldsymbol{x}) \simeq \varphi(t)\,. \tag{1.17}$$

[5]Note that this direct proportionality is only given in Standard Cosmology (see [25] for more details).

Hence, only the homogeneous background field $\varphi(t)$ will enter the field's energy-momentum tensor and thus dictate the dynamics of the inflationary period. In this case we have

$$T_{\mu\nu} = \partial_\mu\varphi\ \partial_\nu\varphi - g_{\mu\nu}\left(\frac{1}{2}g^{\alpha\beta}\partial_\alpha\varphi\ \partial_\beta\varphi - V(\varphi)\right), \tag{1.18}$$

from whose components $T^0_0 = \rho_\varphi$ and $T^i_j = -P_\varphi\delta^i_j$ we obtain the energy density and pressure,

$$\rho_\varphi = \frac{1}{2}(\dot\varphi)^2 + V(\varphi)\,, \quad P_\varphi = \frac{1}{2}(\dot\varphi)^2 - V(\varphi)\,. \tag{1.19}$$

Using these expressions, the Friedmann Equation (1.8a) then takes the form

$$H^2 = \frac{\rho_\varphi}{3M_{\rm pl}} = \frac{1}{3M_{\rm pl}}\left(\frac{1}{2}(\dot\varphi)^2 + V(\varphi)\right) \tag{1.20}$$

$$\overset{(1.16)}{<} -\frac{P_\varphi}{9M_{\rm pl}} = -\frac{1}{9M_{\rm pl}}\left((\dot\varphi)^2 - V(\varphi)\right) \quad \Leftrightarrow \quad (\dot\varphi)^2 - V(\varphi) < 0\,. \tag{1.21}$$

Thus, the scalar field's energy density is dominated by its potential energy $V(\varphi)$ during an inflationary period. Taking the time derivative of Eq. (1.20) and combining it with x yields an equation of motion (EOM) for the scalar (background) field $\varphi(t)$, i.e,

$$\dot H = -\frac{1}{2}\frac{(\dot\varphi)^2}{M^2_{\rm pl}}\,, \tag{1.22a}$$

$$\Rightarrow\ 0 = \ddot\varphi + 3H(t)\dot\varphi + V'(\varphi)\,, \tag{1.22b}$$

$$\varepsilon \equiv -\frac{\dot H}{H^2} = \frac{(\dot\varphi)^2}{2H^2M^2_{\rm pl}}\,, \quad \delta \equiv -\frac{\ddot\varphi}{H\dot\varphi}\,, \tag{1.22c}$$

where we identify Eq. (1.22b) as the Klein-Gordon (KG) equation in an FLRW-spacetime containing a term proportional to the Hubble parameter commonly known as *Hubble friction*, and a force-like term generated by the potential's derivative $V'(\varphi) \equiv dV(\varphi)/d\varphi$.

This general set of equations (1.20) and (1.22b) can now be further approximated by means of the *slow-roll approximation* ($\epsilon \ll 1$ and $|\delta| \ll 1$) where we make explicit use of the conditions in Eq. (1.16) to describe the scalar field's evolution during an inflationary period. In particular, we obtain an almost constant Hubble parameter as well as a simplified KG equation,

$$H^2 = \frac{\rho}{3M^2_{\rm pl}} \approx \frac{V(\varphi)}{3M^2_{\rm pl}}\,, \tag{1.23a}$$

$$\Rightarrow\ \dot\varphi \approx -\frac{V'(\varphi)}{3H}\,, \tag{1.23b}$$

$$\varepsilon \approx \frac{M^2_{\rm pl}}{2}\left(\frac{V'(\varphi)}{V(\varphi)}\right)^2 \equiv \varepsilon_V\,. \tag{1.23c}$$

Note that the slow-roll approximation naturally breaks down when $\varepsilon_V \to 1$.
One may also generally estimate the scalar background field value $\varphi_{\rm cl}$ at which classical dynamics take over, i.e., where the classical background field φ dynamics dominate the quantum fluctuations [26], by comparing

$$-\frac{V'(\varphi)}{3H} \approx \dot{\varphi} \geq \dot{\varphi}_Q = \frac{H^2}{2\pi}\,, \tag{1.24}$$

$$\Rightarrow \left|V'(\varphi_{\rm cl}, T)\right| = \frac{H^3}{2\pi^2}\,. \tag{1.25}$$

We will use this condition later in Sec. 1.4.2 to consistently estimate the end of the linear *or* quantum regime in which fluctuation modes grow exponentially.

To conclude, a phase of *slow-roll inflation* can therefore be characterized by a scalar field evolving slowly from an initial condition where its energy density was dominated by its potential energy, leading to an approximately constant Hubble parameter and a temporary (quasi-)exponential expansion of the Universe. Note that the scale factor is then given by

$$a(t) = a_0\, e^{\int_{t_0}^{t} dt'\ H(t')} \approx a_0\, e^{H(t-t_0)} = a_0\, e^{N-N_0} \equiv a(N)\,, \tag{1.26}$$

where $N(t) \equiv Ht$ is called an *efold* describing the spacetime growth factor within a *Hubble time* $T_H = H^{-1}$. Hence, an inflationary spacetime is well-approximated by a de Sitter spacetime for which the line element concretely reads

$$\begin{aligned} ds^2 &= dt^2 - a^2(t)\ d\boldsymbol{x}^2 = dt^2 - e^{2Ht}\ d\boldsymbol{x}^2 \\ &= a^2(\eta)\left[d\eta^2 - d\boldsymbol{x}^2\right] = (\eta H)^{-2}\left[d\eta^2 - d\boldsymbol{x}^2\right]\,, \end{aligned} \tag{1.27}$$

where in the last line we performed a coordinate transformation from coordinate time t to *conformal time* η via

$$d\eta \equiv \frac{dt}{a(t)} \Leftrightarrow \eta - \eta_0 = \int_0^t \frac{dt'}{a(t')} \overset{(1.27)}{=} -\frac{1}{a_0 H} e^{-Ht} = -\frac{1}{a(t)H}\,. \tag{1.28}$$

Now we can also then define the *conformal Hubble parameter*

$$\mathcal{H} \equiv \left(\frac{a'(\eta)}{a(\eta)}\right)^2 = a(t)H(t)\,, \tag{1.29}$$

where the prime here denotes the derivative with respect to conformal time.

1.1.4 Evolution of fluctuations in our Universe: Cosmological Perturbation Theory

Unerstanding the origins of the Large Scale Structure (LSS), i.e., the present-day matter or energy distribution in our Universe, requires us to study how small perturbations of the metric and energy-momentum evolve in a FLRW-spacetime. The corresponding framework is called *Cosmological perturbation theory* and consists of the following steps [25, 27]:

- **Defining the curvature and energy-momentum perturbations.** Start from the flat ($k = 0$) FLRW-metric as in Eq. (1.7) and the perfect fluid energy-momentum tensor as the homogeneous "background tensors" and introduce small perturbations upon them,

$$g_{\mu\nu}(\eta, \boldsymbol{x}) = g^{\mathrm{FLRW}}_{\mu\nu}(\eta) + \delta g_{\mu\nu}(\eta, \boldsymbol{x})\,, \tag{1.30a}$$

$$T_{\mu\nu}(\eta, \boldsymbol{x}) = T^{\mathrm{PF}}_{\mu\nu}(\eta) + \delta T_{\mu\nu}(\eta, \boldsymbol{x})\,. \tag{1.30b}$$

- **Revealing the relevant dynamical dofs.** We may further rewrite these tensors using the the *Scalar-Vector-Tensor (SVT) decomposition*. It originates from the Helmholtz theorem stating that a vector field living on a spatial slice $\Sigma(\eta)$ may be decomposed into a curl-free and divergence-free contribution via

$$V(\boldsymbol{x}) = \nabla A(\boldsymbol{x}) + \nabla \times \boldsymbol{B}(\boldsymbol{x})\,, \tag{1.31}$$

where A is a scalar and $\boldsymbol{B}$ is a vector field. This decomposition rule also applies to tensors. In particular, one may write out the contributions to the metric perturbation, i.e., a rank-2 symmetric tensor in flat spacetime with 10 dofs in total, in terms of four scalar fields $\{A, B_s, C, E_s\}$ (4 scalar dofs), two divergence-free vectors $\{\boldsymbol{B}^i_v, \boldsymbol{E}^i_v\}$ (4 vector dofs) and one transverse, traceless, and symmetric spatial tensor field $\{E^T_{ij}\}$ (2 tensorial dofs).[6] Note that the purely tensorial part corresponds to gravitational waves and its two dofs to the two possible polarizations $\{+, \times\}$. In the following, we will refer to these fields as *metric perturbation fields*. The decomposed perturbed line element then reads

$$ds^2 = a^2(\eta)\left[(1+A)\,d\eta^2 + 2\boldsymbol{B}^i d\eta\, d\boldsymbol{x}_i + (\delta_{ij} + h_{ij}) d\boldsymbol{x}_i\, d\boldsymbol{x}_j\right]\,, \tag{1.32}$$

$$= a^2(\eta)\left[(1+A)\,d\eta^2 + 2\left(\partial_i B_s + \boldsymbol{B}^i_v\right) d\eta\, d\boldsymbol{x}_i\right. \tag{1.33}$$

$$\left. + \left(\delta_{ij} + \left(2C\delta_{ij} + 2\partial_{\langle i}\partial_{j\rangle} E_s + 2\partial_{(i}\boldsymbol{E}_{v,j)} + E^T_{ij}\right)\right) d\boldsymbol{x}_i\, d\boldsymbol{x}_j\right]\,. \tag{1.34}$$

While this seems like a huge effort, its tremendous advantage lies in the decoupling of the EOMs of the indivifual fields at linear order in perturbation theory, enabling us to study their evolution independently from each other. We can proceed analogously with the decomposition of the energy-momentum tensor yielding

$$T^0_{\ 0} = \bar{\rho}(\eta) + \delta\rho(\eta, \boldsymbol{x})\,, \tag{1.35}$$

$$T^i_{\ 0} = \left[\bar{\rho}(\eta) + \bar{P}(\eta)\right] \boldsymbol{v}^i \equiv \boldsymbol{q}^i\,, \tag{1.36}$$

$$T^i_{\ j} = -\left[\bar{P}(\eta) + \delta P(\eta, \boldsymbol{x})\right] \delta^i_{\ j} - \Pi^i_{\ j}\,, \tag{1.37}$$

$$= -\left[\bar{P}(\eta) + \delta P(\eta, \boldsymbol{x})\right] \delta^i_{\ j} - \left[\partial_{\langle i}\partial_{j\rangle}\Pi_s + \partial_{(i}\boldsymbol{\Pi}_{v,j)} + \Pi^T_{ij}\right] \tag{1.38}$$

[6] For a more detailed explanation, see [25] (Chapter 4.1.)

in which $\mathbf{v}^i$ is the *bulk velocity*, $\Pi^i{}_j$ is the anisotropic stress tensor, and the energy density and pressure[7] were decomposed to homogeneous scalar background and fluctuation fields. Later we might also make use of the *dimensionless density contrast* defined as $\delta \equiv \delta\rho/\bar{\rho}$.

Note that the perturbation fields are in general not gauge-independent and thus may change under a coordinate transformation; equivalently, coordinate changes may introduce "artificial" perturbations that are not physically measurable. It is therefore desirable to define certain combinations of them as *gauge-invariant perturbation fields*. On the metric side, we famously have the so-called *Bardeen potentials* [28]

$$\Psi(\eta,\boldsymbol{x}) = A(\eta,\boldsymbol{x}) + \mathcal{H}\left(B(\eta,\boldsymbol{x}) - E'(\eta,\boldsymbol{x})\right) + \left(B(\eta,\boldsymbol{x}) + E'(\eta,\boldsymbol{x})\right), \tag{1.39}$$

$$\Phi(\eta,\boldsymbol{x}) = -C(\eta,\boldsymbol{x}) + \mathcal{H}\left(B(\eta,\boldsymbol{x}) - E'(\eta,\boldsymbol{x})\right) + \frac{1}{3}\nabla^2 E(\eta,\boldsymbol{x}), \tag{1.40}$$

$$\boldsymbol{\Phi}_i(\eta,\boldsymbol{x}) = \boldsymbol{E}_i'(\eta,\boldsymbol{x}) - \boldsymbol{B}_i'(\eta,\boldsymbol{x}), \quad E_{ij}(\eta,\boldsymbol{x}). \tag{1.41}$$

- **Deriving the perturbations' EOMs.** The dynamics of the system can be deduced from energy-momentum conservation equation as well as the Einstein equation in terms of the perturbation fields. The first case yields the *continuity equation* of the density contrasts $\delta_i \equiv \delta\rho_i/\rho_i$,

$$\begin{aligned} 0 = \delta_i'(\eta,\boldsymbol{x}) &+ \left(1 + \frac{\bar{P}_i(\eta)}{\bar{\rho}_i(\eta)}\right)\left(\partial_j \boldsymbol{v}_j^i - 3\Phi'(\eta,\boldsymbol{x})\right) \\ &+ 3\mathcal{H}(\eta)\left(\frac{\delta\bar{P}_i(\eta,\boldsymbol{x})}{\bar{\rho}_i(\eta)} - \frac{\bar{P}_i}{\bar{\rho}_i}\delta_i(\eta,\boldsymbol{x})\right), \end{aligned} \tag{1.42}$$

and the second case yields the *metric perturbation evolution equations*,

$$4\pi G a^2(\eta)\delta\rho(\eta,\boldsymbol{x}) = \nabla^2\Phi(\eta,\boldsymbol{x}) - 3\mathcal{H}(\eta)\left(\Phi'(\eta,\boldsymbol{x}) + \mathcal{H}\Psi(\eta,\boldsymbol{x})\right), \tag{1.43a}$$

$$8\pi G a^2(\eta)\Pi_s(\eta,\boldsymbol{x}) = \Phi(\eta,\boldsymbol{x}) - \Psi(\eta,\boldsymbol{x}), \tag{1.43b}$$

$$\begin{aligned} 4\pi G a^2(\eta)\delta P(\eta,\boldsymbol{x}) &= \Phi''(\eta,\boldsymbol{x}) + \mathcal{H}(\eta)\Psi'(\eta,\boldsymbol{x}) + 2\mathcal{H}(\eta)\Phi'(\eta,\boldsymbol{x}) \\ &\quad + \frac{1}{3}\nabla^2\left(\Psi(\eta,\boldsymbol{x}) - \Phi(\eta,\boldsymbol{x})\right) \\ &\quad + \left(2\mathcal{H}'(\eta) + \mathcal{H}(\eta)\right)\Psi(\eta,\boldsymbol{x}) \end{aligned} \tag{1.43c}$$

$$\begin{aligned} &\approx \Phi''(\eta,\boldsymbol{x}) + 3\mathcal{H}\Phi'(\eta,\boldsymbol{x}) \\ &\quad + \left(2\mathcal{H}(\eta) + \mathcal{H}'(\eta)\right)\Phi(\eta,\boldsymbol{x}), \end{aligned} \tag{1.43d}$$

[7] As in Sec. 1.1.2, we note that the energy density and pressure shall be further understood as the sum of the contributions from all species, i.e., $\rho = \sum_i \rho_i$ and $P = \sum_i P_i$.

where the last equation is an approximation applicable in the absence of anisotropic stress ($\Pi_s = 0$) such that $\Phi \approx \Psi$ (see Eq. (1.43b)). Evidently, the FLRW-background metric responds to small perturbations in the pressure by generating dynamic *curvature perturbations* described by Bardeen variable Φ.[8]

For special applications such as the study of curvature perturbations from inflationary periods, it is more practical to work with the *comoving curvature perturbation* $\mathcal{R}$ and the *uniform-density curvature perturbation* ζ,

$$\mathcal{R}(\eta, \boldsymbol{x}) = -\Phi(\eta, \boldsymbol{x}) + \frac{H}{\bar{\rho}(\eta) + \bar{P}(\eta)}\, \delta q_s(\eta, \boldsymbol{x}) \overset{\delta q_s \to 0}{\longrightarrow} -\Phi(\eta, \boldsymbol{x})\,, \tag{1.44}$$

$$\zeta(\eta, \boldsymbol{x}) = -\Phi(\eta, \boldsymbol{x}) + \frac{H}{\dot{\bar{\rho}}(\eta)} \delta\rho(\eta, \boldsymbol{x}) \overset{\delta\rho \to 0}{\longrightarrow} -\Phi(\eta, \boldsymbol{x})\,, \tag{1.45}$$

which describe the change of the spacetime curvature of a comoving ($\delta q = 0$) spatial slice, and on a spatial slice of uniform energy density ($\delta\rho = 0$) with respect to the background spacetime, respectively. One can show that on super-horizon scales, i.e., for perturbation Fourier modes with wavenumbers $k \ll r_H(\eta)$, both expressions coincide, $\mathcal{R} \simeq \zeta$.

1.1.5 Curvature Perturbations on different spatial scales

If we are interested in how the curvature perturbations vary on different spatial scales k, we shall compute and study its so-called *power spectrum*. Formally, this quantity is defined for statistical variables f which have

$$\langle f \rangle \simeq 0 \;\Rightarrow\; \mathrm{Var}(f) \equiv \langle f^2 \rangle - \langle f \rangle^2 \simeq \langle f^2 \rangle\,, \tag{1.46}$$

where $\langle \circ \rangle$ is the expectation value operator and $\mathrm{Var}(\circ)$ the variance operator. If $f = f(t, \boldsymbol{x})$ is now a field, we can relate the latter to the *equal-time correlation function* of f,

$$\begin{aligned}
\mathrm{Var}(f)(\eta) \simeq \langle f^2 \rangle &= \langle f(\eta, \boldsymbol{x}) f(\eta, \boldsymbol{0}) \rangle \qquad (1.47)\\
&= \iint \frac{d^3\boldsymbol{k}}{(2\pi)^3} \frac{d^3\boldsymbol{p}}{(2\pi)^3}\, \langle \tilde{f}_k(t) \tilde{f}_p(t) \rangle\, e^{-i\boldsymbol{k}\boldsymbol{x}}\\
&= \iint \frac{d^3\boldsymbol{k}}{(2\pi)^3} \frac{d^3\boldsymbol{p}}{(2\pi)^3} e^{-i\boldsymbol{k}\boldsymbol{x}}\, (2\pi)^3 \delta^3(k - p)\, \mathcal{P}_f(k, t)\\
&= \int \frac{d^3\boldsymbol{k}}{(2\pi)^3}\, \mathcal{P}_f(k, t)\, e^{-i\boldsymbol{k}\boldsymbol{x}} = \int d\ln(k)\, \Delta_f(k, t)\, e^{-i\boldsymbol{k}\boldsymbol{x}}\,, \qquad (1.48)
\end{aligned}$$

[8] Due to the similarity of these equations to the weak-field expansion in GR, this specific Bardeen variable Φ is also called the *gravitational potential* in [25].

and define the (dimensionful) power spectrum $\mathcal{P}_f(k,t)$ as its Fourier transform, whose dimensionless version then reads

$$\Delta_f(k,t) = \frac{k^3}{2\pi^2}\mathcal{P}_f(k,t)\,. \tag{1.49}$$

Applied to the curvature perturbations $\mathcal{R}$, this yields the general expressions

$$\Delta_{\mathcal{R}}(k,t) = \frac{k^3}{2\pi^2}\mathcal{P}_{\mathcal{R}}(k,t) = \frac{k^3}{2\pi^2}\int d^3\boldsymbol{x}\,\langle\mathcal{R}(\eta,\boldsymbol{0})\mathcal{R}(\eta,\boldsymbol{x})\rangle\,e^{+i\boldsymbol{k}\boldsymbol{x}}\,. \tag{1.50}$$

Following Eq. (1.44), its concrete functional shape must depend on the nature of the energy content in the perturbed spacetime.

1.2 Scalar Fields in Curved Spacetimes

Suppose we have a (complex) *quantum* scalar field $\Phi(\eta, \boldsymbol{x})$ in a general curved spacetime described by the metric $g_{\mu\nu} \neq \eta_{\mu\nu}$. The physical information of such system is encoded in the *minimally-coupled matter action*,

$$S = \int d\eta\, d^3\boldsymbol{x} \sqrt{-g} \left[\frac{1}{2} g_{\mu\nu} \partial^\mu \Phi \partial^\nu \Phi - V(\Phi) \right] . \tag{1.51}$$

Since such quantum fields constitute the energy content in our Universe, we want to understand their evolution on a *flat* FLRW-metric (in conformal time). In this special case we have

$$g_{\mu\nu} = -a^2(\eta)\, \mathrm{diag}(-1,1,1,1) \quad \Rightarrow \quad \sqrt{-g} = a^2(\eta)\,, \tag{1.52}$$

such that the *FLRW-matter* action reads

$$S_{\mathrm{FLRW}} = \int d\eta\, d^3\boldsymbol{x}\; a^2(\eta) \left[\frac{1}{2} \left(\left(\Phi'\right)^2 - \left(\nabla^2 \Phi\right) \right) - a^2(\eta)\, V(\Phi) \right] . \tag{1.53}$$

By applying the variational principle to the action, i.e., $\delta S_{\mathrm{FLRW}} \overset{!}{=} 0$, we recover a modified KG-equation as EOM for the scalar field[9] in FLRW-spacetime,

$$\begin{aligned} 0 &= \Phi''(\eta, \boldsymbol{x}) + 2\mathcal{H}(\eta, \boldsymbol{x}) \Phi'(\eta, \boldsymbol{x}) - \nabla\Phi(\eta, \boldsymbol{x}) + V'(\Phi(\eta, \boldsymbol{x})) \\ &= \ddot{\Phi}(t, \boldsymbol{x}) + 3H(t) \dot{\Phi}(t, \boldsymbol{x}) - a^{-2}(t) \nabla\Phi(t, \boldsymbol{x}) + V'(\Phi(t, \boldsymbol{x})) \end{aligned} \tag{1.54}$$

$$\begin{aligned} 0 &= v_k''(\eta) + 2\mathcal{H}(\eta) v_k'(\eta) - k^2 v_k(\eta) + V'(\Phi(\eta, \boldsymbol{x})) \\ &= \ddot{v}_k(t) + 3H(t) \dot{v}_k(t) - k^2 v_k(t) + V'(\Phi(t, \boldsymbol{x}))\,, \end{aligned} \tag{1.55}$$

where the first and second expressions in the above equations are formulated in conformal time η and coordinate time t, respectively.[10] In Eq. (1.55) we used the Fourier decomposition of Φ to obtain EOMs for its Fourier modes $v_k(\eta)$

$$\begin{aligned} \Phi(\eta, \boldsymbol{x}) &= \int \frac{\mathrm{d}^3\boldsymbol{k}}{\sqrt{(2\pi)^3 a^2}} \left[v_k(\eta)\, \hat{a}_k + v_k^\star(\eta)\, \hat{a}^\dagger_{-k} \right] e^{+i\boldsymbol{k}\cdot\boldsymbol{x}} \\ &= \int \frac{\mathrm{d}^3\boldsymbol{k}}{\sqrt{(2\pi)^3 a^2}}\, \Phi_{\mathrm{k}}(\eta)\, e^{+i\boldsymbol{k}\cdot\boldsymbol{x}}\,. \end{aligned} \tag{1.56}$$

In the following, we will refer to the time-dependent Fourier mode functions v_k as *k-mode functions*. Note that the process of canonical quantisation requires a proper normalisation to guarantee $[\hat{a}_k, \hat{a}_k^\dagger] \equiv 1$, which is realised when

$$i = u_k \cdot (u_k^\star(\eta))' - (u_k(\eta))'\, u_k^\star\,. \tag{1.57}$$

[9] Note that the complex conjugated Fourier modes $v_k^\star(\eta)$ follow the same EOM, this is why it has been omitted here.

[10] Throughout this work, we will denote *coordinate time* derivatives as usual with the dot operator $(\circ)\dot{}$, and *conformal time* derivative with the prime operator $(\circ)'$. The only exception to the latter case is the field-derivative of a potential, i.e., $V'(\varphi) = dV(\varphi)/d\varphi$.

1.2.1 Mukhanov-Sasaki Equation

To study the dynamics *small* quantum complex[11] scalar field fluctuations, we may decompose the full quantum scalar field $\Phi(\eta, \boldsymbol{x})$ into a homogeneous background (or *mean-*) field $\varphi(\eta)$ and a small fluctuation field $\delta\phi(\eta, \boldsymbol{x})$ upon it,

$$\Phi(\eta, \boldsymbol{x}) = \langle \Phi(\eta, \boldsymbol{x}) \rangle + \delta\phi(\eta, \boldsymbol{x}) = \varphi(\eta) + \delta\phi(\eta, \boldsymbol{x}) = \varphi(\eta) + \frac{\tilde{\delta\phi}(\eta, \boldsymbol{x})}{a(\eta)}\,, \tag{1.58}$$

where we introduced the *comoving fluctuation field* $\tilde{\delta\phi}$, and we will henceforth identify the background field with the full quantum scalar field's *vacuum expectation value*, i.e., $\varphi(\eta) = \langle \Phi(\eta, \boldsymbol{x}) \rangle$.
Note that in the case where $\varphi(\eta) \approx 0$, we may associate the fluctuation field $\delta\phi(\eta, \boldsymbol{x})$ with the full quantum scalar field $\Phi(\eta, \boldsymbol{x})$; the same applies to the corresponding k-mode functions.
Plugging in Eq. (1.58) into the FLRW-matter action of Eq. (1.53) and expanding up to second order in scalar field fluctuations while working in *spatially-flat gauge* [12] yields two *decoupled* differential equations, one for the homogeneous background field $\varphi(\eta)$ and one the comoving fluctuation field $\tilde{\delta\phi}(\eta, \boldsymbol{x})$,

$$0 = \varphi''(\eta) + 2\mathcal{H}(\eta)\varphi'(\eta) + a^2(\eta)V'(\varphi(\eta))\,, \tag{1.59a}$$

$$0 = \delta\phi''(\eta, \boldsymbol{x}) - \left(\nabla\delta\phi(\eta, \boldsymbol{x})\right)^2 + \left[a^2(\eta)\, V''(\varphi) - \frac{z''(\eta)}{z(\eta)}\right]\delta\phi(\eta, \boldsymbol{x}) \tag{1.59b}$$

$$= u_k''(\eta) + \left[k^2 - \frac{z''(\eta)}{z(\eta)} + a^2(\eta)\, V''(\varphi)\right] u_k(\eta),\,, \tag{1.59c}$$

where the last equation is also known as the *Mukhanov-Sasaki equation*, which describes the evolution of the *comoving k-mode functions* $u_k(\eta)$ of the fluctuation field $\delta\phi(\eta, \boldsymbol{x})$, and $z(\eta) \equiv a(\eta)\,\varphi'(\eta)/\mathcal{H}(\eta)$ is the so-called *Mukhanov variable*. Here, k is now the comoving momentum or wavenumber, i.e., $k = k_{\mathrm{com}} \equiv a(\eta)k_{\mathrm{phys}} = \text{const.}$.
Now let us constrain this result to an *inflationary spacetime* in the *quasi-de Sitter approximation*, which serves as a suitable approximation for the on-set phase of inflation and is described by the conditions of Eqs. (1.16) with the additional claim that

$$\varepsilon = \text{const.} \ll 1 \quad \Rightarrow \quad \frac{z''(\eta)}{z(\eta)} \approx \frac{a''(\eta)}{a(\eta)} \overset{(1.28)}{\approx} \frac{2}{\eta^2}\,, \tag{1.60}$$

which further simplifies the Mukhanov-Sasaki equation to

$$0 = u_k''(\eta) + \left[k^2 - \frac{2}{\eta^2} + a^2(\eta)\, V''(\varphi)\right] u_k(\eta) = u_k''(\eta) + \omega_k^2(\eta)\, u_k(\eta)\,. \tag{1.61}$$

[11] Here again we omit the explicit notation of the real and imaginary component since their EOMs turn out to be identical.

[12] This is a convenient gauge to choose where $\Psi = 0$ such that we can relate the curvature perturbations $\mathcal{R}(\eta, \boldsymbol{x})$ directly to the fluctuation field $\delta\phi(\eta, \boldsymbol{x})$.

This equation is of the shape of a time-dependent harmonic oscillator with frequency

$$\omega_k^2(\eta) = k^2 - \frac{2}{\eta^2} + a^2(\eta)\, m^2(\varphi(\eta)) = \Omega_k^2(\eta) - 2\left(a(\eta)\mathcal{H}(\eta)\right)^2 \tag{1.62}$$

$$= k^2 - \frac{1}{\eta^2}\left(\nu^2(T(\eta)) - \frac{1}{4}\right), \tag{1.63}$$

$$\nu^2(T(\eta)) = \frac{9}{4} + \frac{|m^2(\varphi(\eta)),\, T(\eta)|}{H^2}, \tag{1.64}$$

where we have introduced the effective background field or *curvature mass* $m^2(\varphi(\eta)) = V''(\varphi)$[13] and $\Omega_k^2 = k^2 + a^2(\eta)\, m^2(\varphi(\eta))$.

Note that in the case $m^2 \approx$ const., we can express the general solution of Eq. (1.61) via the Hankel functions of first and second kind,

$$u_k(\eta) = \sqrt{-\eta}\left[C_1 H_\nu^{(1)}(-k\eta) + C_2 H_\nu^{(2)}(-k\eta)\right], \quad C_1^2 + C_2^2 = 1\,. \tag{1.65}$$

The behaviour of the solution of this second-order *linear* differential equation is entirely determined by the sign and value of ω_k^2 or equivalently the order of scales between its constituents. For $\omega_k^2 > 0$, two very common interesting limits emerge, namely the *sub-horizon limit*, i.e., $\Omega_k^2(\eta) \gg (aH)^2$, and the *super-horizon limit*, i.e., $\Omega_k^2(\eta) \ll (aH)^2$:

I *Comoving sub-horizon fluctuations* have a frequency which is dominated by the wavenumber k, such that their EOMs reduce to a simpler harmonic oscillator,

$$0 \approx u_k''(\eta) + \Omega_k^2(\eta)\, u_k(\eta) \overset{m^2 \to 0}{\longrightarrow} u_k''(\eta) + k^2\, u_k(\eta)\,. \tag{1.66}$$

which becomes even time-independent in the case of vanishing curvature mass or slow-roll inflation where $m^2(\varphi) = V''(\varphi)$ is very small (see Eq. (1.23c)). We then recover a simple plane wave solution $u_k(\eta) \propto e^{-ik\eta}$. It is a suitable assumption that at the beginning of inflation ($\eta \lll 0$), (almost) all modes were inside the Hubble horizon. Only in this special situation are able to define a *unique vacuum state or initial condition*

$$u_k^{\rm vac}(\eta) = \lim_{\eta \to -\infty} u_k(\eta) = \frac{1}{\sqrt{2k}} e^{-ik\eta}\,. \tag{1.67}$$

It was Bunch and Davies [29] who derived the famous *Bunch-Davies (BD) vacuum mode function* from the solution of Eq. (1.61),

$$u_k^{\rm vac}(\eta) = u_k^{\rm BD}(\eta) \equiv \frac{e^{-i\eta\,\omega_k(\eta)}}{\sqrt{2\omega_k(\eta)}}\left(1 - \frac{i}{\eta\,\omega_k(\eta)}\right). \tag{1.68}$$

This expression serves as an ideal initial condition for the study of the evolution of inflationary scalar fluctuations.

[13] Note that m^2 may also depend on the temperature T if the potential is temperature-dependend.

- On the other hand, *comoving super-horizon fluctuations* have momenta or wavenumbers way smaller than the current Hubble horizon size, leading to simplified differential equation of the form

$$0 = u_k''(\eta) - \frac{a''(\eta)}{a(\eta)}\, u_k(\eta) \quad \Leftrightarrow \quad \frac{u_k''(\eta)}{u_k(\eta)} = \frac{a''(\eta)}{a(\eta)} \tag{1.69}$$

  whose exact solution consists of a constant (A) and a decaying part[14],

$$u_k(\eta) = A + B \int^{\eta} \frac{d\eta'}{a^2(\eta')} = A + \frac{BH^2}{3}\eta^3 \,, \tag{1.70}$$

We conclude that while k-modes which are deep in the Hubble horizon are highly-oscillating, those which already left the Hubble horizon freeze out and become constant. Thus, when using the BD vacuum as initial condition, the exact solution of Eq. (1.61) interpolates between these two typical regimes. The moment $\eta_{\rm cross}$ when

$$\Omega_k^2(\eta_{\rm cross}) = \left(a(\eta_{\rm cross})\mathcal{H}(\eta_{\rm cross})\right)^2 \,, \tag{1.71}$$

is also called *horizon crossing*.

The *Amplitude*-Mukhanov-Sasaki equation We are free to express the complex comoving k-mode functions $u_k(\eta)$ through an amplitude and a phase, i.e., $u_k(\eta) = A_k(\eta)\exp\left(i\eta\theta_k(\eta)\right)$, whose derivatives now explicitly read

$$u_k(\eta) = A_k(\eta)\, e^{i\theta_k(\eta)} \,, \tag{1.72}$$

$$u_k'(\eta) = \left(A_k'(\eta) + i\, A_k(\eta)\, \theta_k'(\eta)\right)\, e^{i\theta_k(\eta)} \,, \tag{1.73}$$

$$u_k''(\eta) = \left(A_k''(\eta) + i\left(2A_k'(\eta)\,\theta_k'(\eta) + A_k'(\eta)\,\theta_k''(\eta)\right) - A_k'(\eta)\left(\theta_k'\right)^2\right)\, e^{i\theta_k(\eta)} \,. \tag{1.74}$$

Inserting these expressions in the mode normalisation condition Eq. (1.57), we obtain yet another helpful relation,

$$\theta_k'(\eta) = \frac{1}{2\, A_k^2(\theta)} \,. \tag{1.75}$$

that we can use together with Eqs. (1.72) to derive a differential equation *only* for the k-mode function's amplitude $A_k(\eta) \equiv |u_k(\eta)|$ reading

$$0 = A_k''(\eta) - A_k(\eta)\left(\theta_k'\right)^2 + \omega_k^2\, A_k(\eta) \,, \tag{1.76}$$

$$= A_k''(\eta) - A_k(\eta)\left(\frac{1}{2\, A_k^2(\theta)}\right)^2 + \omega_k^2\, A_k(\eta) \,, \tag{1.77}$$

$$= A_k''(\eta) - \frac{1}{4\, A_k^3(\eta)} + \omega_k^2(\eta)\; A_k(\eta) \,. \tag{1.78}$$

[14] Remember that η *per definition* evolves from $-\infty$ to 0.

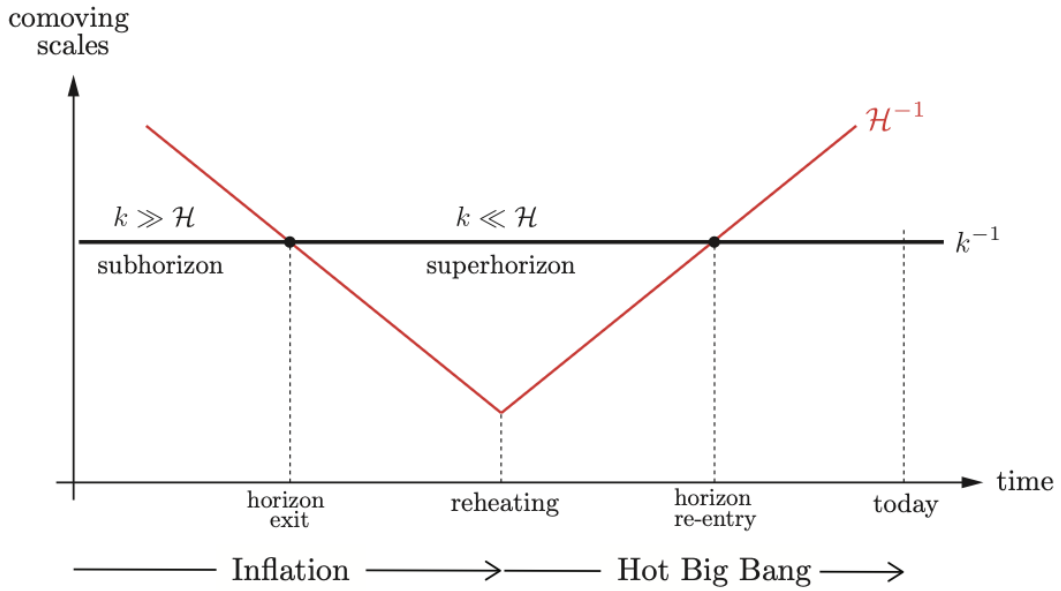

Figure 1.3: The fate of comoving fluctuation modes in a Universe exhibiting a (finite) inflationary period. Since the latter is characterized by a shrinking Hubble radius, fluctuation modes with comoving wavenumber k exit the Hubble horizon at horizon crossing, i.e., where $k = a_{\rm exit}\mathcal{H}$ and freeze-out, and re-enter later again some while after inflation has already ended at $k = a_{\rm entry}\mathcal{H}(a_{\rm entry})$. Note that only those fluctuation modes which have exited the horizon until the end of inflation can contribute to later curvature perturbations. Figure from [25].

Clearly, we have traded in a *linear* second-order differential equation for our two functions $\{\mathrm{Re}(u_k), \mathrm{Im}(u_k)\}$ for a *non-linear* second-order differential equation of *only* the amplitude $A_k \equiv |u_k| = \sqrt{\mathrm{Re}(u_k) \cdot \mathrm{Im}(u_k)}$. Numerically, this has however the huge advantage of halving the number of simulated equations necessary to track the k-mode function's evolution, and removing the phase factor which avoids the costly resolution of high-frequency oscillations as in later application (see Sec. 3).

1.2.2 Scalar-Induced Curvature Power Spectrum

Later we will be interested in the case where super-horizon ($k \ll (aH)^{-1}$) curvature perturbations are sourced from quantum scalar field fluctuations during slow-roll inflation (see also Sec. 1.2). In this set-up, the scalar background field or *vacuum expectation value* $\varphi(\eta)$ is zero for most of the time, i.e.,

$$\Phi(\eta, \boldsymbol{x}) = \langle \Phi(\eta, \boldsymbol{x}) \rangle + \delta\phi(\eta, \boldsymbol{x}) = \varphi(\eta) + \delta\phi(\eta, \boldsymbol{x}) \approx \delta\phi(\eta, \boldsymbol{x}) = \frac{\widetilde{\delta\phi}(\eta, \boldsymbol{x})}{a(\eta)}\,, \tag{1.79}$$

which is why we can associate the Fourier modes $u_k(\eta)$ in Eq. (1.56) with those of the *comoving* fluctuation field $\widetilde{\delta\phi}(\eta, \boldsymbol{x})$. With this information and the help of Eq. (1.45), (1.20) and (1.48), we already find

$$\zeta = \frac{H}{\dot{\rho}_\phi}\,\delta\rho_\phi \approx \frac{H}{\dot{\varphi}}\,\delta\phi = -\frac{3H^2}{V'(\varphi)}\,\delta\phi\,, \tag{1.80}$$

$$\Rightarrow \mathcal{P}_\zeta(k,\eta) = \left(\frac{3H^2}{V'(\varphi)}\right)^2 \mathcal{P}_{\delta\phi}(k,\eta) = \left(\frac{3H^2}{V'(\varphi)}\right)^2 \mathcal{P}_{\tilde{\delta\phi}/a}(k,\eta) \tag{1.81}$$

Hence, we obtain the *scalar-induced curvature power spectrum* from studying the spectral distribution of the scalar field fluctuations. For this, we first need to evaluate the equal-time correlation function,

$$\begin{aligned}
&\langle \Phi(\eta, \boldsymbol{x}) \Phi(\eta, \boldsymbol{0}) \rangle \qquad (1.82)\\
&= \iint \frac{d^3\boldsymbol{k}}{(2\pi)^3} \frac{d^3\boldsymbol{p}}{(2\pi)^3} \left\langle \left(u_k \hat{a}_k + u^\star_{-k} \hat{a}^\dagger_{-k}\right) \left(u_p \hat{a}_p + u^\star_{-p} \hat{a}^\dagger_{-p}\right) \right\rangle_{\mathrm{T}} e^{-i\boldsymbol{k}\boldsymbol{x}}\\
&= \iint \frac{d^3\boldsymbol{k}}{(2\pi)^3} \frac{d^3\boldsymbol{p}}{(2\pi)^3} \left[u_k u^\star_{-p} \langle \hat{a}_k \hat{a}^\dagger_{-p} \rangle_{\mathrm{T}} + u^\star_{-k} u_p \langle \hat{a}^\dagger_{-k} \hat{a}_p \rangle_{\mathrm{T}} \right] e^{-i\boldsymbol{k}\boldsymbol{x}}\\
&= \iint \frac{d^3\boldsymbol{k}}{(2\pi)^3}\, d^3\boldsymbol{p}\, \delta^3(\mathrm{k} + \mathrm{p})\\
&\qquad \times \left[u_k u^\star_{-p}\,(1 + n_{\mathrm{B}}(\mathrm{k})) + u^\star_{-k} u_p\, n_{\mathrm{B}}(-\mathrm{k}) \right] e^{-i\boldsymbol{k}\boldsymbol{x}}\\
&\overset{(1.84)}{=} \int \frac{d^3\boldsymbol{k}}{(2\pi)^3}\, |u_k(\eta)|^2 (1 + 2n_{\mathrm{B}}(\mathrm{k}))\, e^{-i\boldsymbol{k}\boldsymbol{x}}\,, \qquad (1.83)
\end{aligned}$$

where used the fact that $|u_k|^2 = |u_{-k}|^2$ in de Sitter spacetime as well as the expressions for the non-vanishing *thermal averages* of ladder operator combinations,

$$\langle \hat{a}_k \hat{a}_p^\dagger \rangle_{\mathrm{T}} \;=\; (1 + n_{\mathrm{B}}(k))\, \delta^3(\vec{k} - \vec{p})\,, \quad \langle \hat{a}_k^\dagger \hat{a}_p \rangle_{\mathrm{T}} \;=\; n_{\mathrm{B}}(k)\, \delta^3(\vec{k} - \vec{p}) \tag{1.84}$$

$$n_{\mathrm{B}}(k,\eta) = \left[\exp\left(\sqrt{k^2(\eta) + m^2}/T(\eta)\right) - 1\right]^{-1}\,, \tag{1.85}$$

where $n_{\mathrm{B}}(-\mathrm{k}) = n_{\mathrm{B}}(\mathrm{k})$ is the spectral Bose-Einstein (BE) distribution for a bosonic field with mass m. The averages $\langle \ldots \rangle_{\mathrm{T}}$ mean the ensemble average at finite temperature; they naturally reduce to the vacuum expression for $T \to 0$ due to the characteristics of $n_{\mathrm{B}}(k)$. If we properly account for the gravitational redshift, where the temperature T and *wavenumber* k scale as

$$k \propto \frac{1}{a} \quad \Leftrightarrow \quad \frac{k(\eta)}{k_i} = \frac{a_i}{a(\eta)}\,, \tag{1.86a}$$

$$T \propto (g_\star(T))^{\frac{1}{3}}\, \frac{1}{a} \quad \Leftrightarrow \quad \frac{T(\eta)}{T_i} = \left(\frac{g_{\star,i}}{g_\star(T(\eta))}\right)^{\frac{1}{3}} \frac{a_i}{a(\eta)} \;\approx^{15}\; \frac{a_i}{a(\eta)}\,, \tag{1.86b}$$

we end up with the redshifted spectral BE-distribution, namely

$$n_{\mathrm{B}}(k,\eta), \overset{(1.86b)}{\approx} \left[\exp\left(\frac{\sqrt{a_i^2 k_i^2 \;+\; a^2(\eta)\, m^2}}{T_i}\right) - 1\right]^{-1}\,. \tag{1.87}$$

Generally, we may also expect a field and scale factor-dependence or equivalently a (conformal) time-dependence in m^2, i.e., $m^2 = m^2(\varphi, T(a(\eta)))$ (see e.g., Sec. 1.4.2).

Combining these equations with Eq. (1.50) leads us to the final expression for the scalar-induced curvature power spectrum from an inflationary (de Sitter) slow-roll pe-

[15] We can neglect the prefactor involving the entropy degrees of freedom number $g_\star$ for time periods where $g_\star(T) \approx$ const.. This is suitable in many situatons and will therefore be used in the redshifted Bose-Einstein distribution. Note that Eq. (1.86b) also constitutes an implicit equation for whose solution T one has to be able to estimate it to be plugged into $g_\star(T(\eta))$, since there is no analytically defined inverse of $a(T)$ or $\eta(T)$. For practical reasons, whenever it is needed and unavoidable, we will estimate the value of $g_\star(T)$ at with a numerical inverse $T_{\mathrm{intpl}}(\eta)$, which we construct via the interpolation of $\eta(T)$.

riod,

$$\begin{aligned}
\mathcal{P}_\zeta(k,\eta) \;\propto\; \mathcal{P}_{\delta\phi}(k,\eta) &= \mathcal{P}_{\tilde{\delta\phi}/a}(k,\eta) \\
&= \int d^3\boldsymbol{x}\, a^{-2}(\eta)\, \langle \tilde{\delta\phi}(\eta,\mathbf{0})\tilde{\delta\phi}(\eta,\boldsymbol{x})\rangle\, e^{+i\boldsymbol{k}\boldsymbol{x}} \\
&\overset{(1.79)}{\approx} \int d^3\boldsymbol{x}\, a^{-2}(\eta)\, \langle \Phi(\eta,\boldsymbol{x})\Phi(\eta,\mathbf{0})\rangle\, e^{+i\boldsymbol{k}\boldsymbol{x}} \\
&\overset{(1.82)}{=} \int d^3\boldsymbol{x}\, e^{+i(\boldsymbol{k}-\boldsymbol{q})\boldsymbol{x}} \int \frac{d^3\boldsymbol{q}}{(2\pi)^3} \left(\frac{|u_q(\eta)|}{a(\eta)}\right)^2 (1+2n_{\rm B}(\mathrm{q})) \\
&= \int d^3\boldsymbol{q}\, \delta^3(\mathrm{k}-\mathrm{q}) \left(\frac{|u_q(\eta)|}{a(\eta)}\right)^2 (1+2n_{\rm B}(\mathrm{q})) \\
&= \left(\frac{|u_k(\eta)|}{a(\eta)}\right)^2 (1+2n_{\rm B}(\mathrm{k}))\;. \qquad (1.88)
\end{aligned}$$

The corresponding *dimensionless scalar-induced curvature power spectrum* reads

$$\begin{aligned}
\Delta_\zeta(k,\eta) &\equiv \frac{k^3}{2\pi^2}\mathcal{P}_\zeta(k,\eta) \qquad (1.89) \\
&= \frac{k^3}{2\pi^2}\left(\frac{3H^2}{V'(\varphi)}\right)^2 \left(\frac{|u_k(\eta)|}{a(\eta)}\right)^2 (1+2n_{\rm B}(\mathrm{k}))\;,
\end{aligned}$$

where $|u_k(\eta)| \equiv A_k(\eta)$ are the solutions of the *Amplitude*-Mukhanov-Sasaki equation (1.78). This expression is to be evaluated at the conformal time $\eta_{\rm cl}$ at which the background field has reached the classical field value $\varphi_{\rm cl}$ of Eq.(1.25), from which point onwards background field dynamics become non-neglectable (see Sec. 1.1.3). Correspondingly, the k-modes that determine this spectrum will be the super-horizon ones with wavenumbers $k \in [a_i\mathcal{H},\, a_i\mathcal{H}\exp(N(\eta_{\rm cl}))]$, since they re-enter the Hubble horizon after the end inflation and produce curvature perturbations. Hence, what we are interested in computing later is

$$\Delta_\zeta^{SI}(k) \equiv \Delta_\zeta(k,\eta_{\rm cl})\,. \qquad (1.90)$$

With this at hand, we may calculate the gravitational wave sprectrum $h^2\Omega_{\rm GW}^{\rm SI}$ from scalar-induced curvature perturbations through Eq. (29) and Eq. (30) from [30] (which

were previously derived and discussed in [31–34]), which reads

$$h^2\Omega_{\rm GW}^{\rm SI}(f) \approx 4.6\times10^4\left(\frac{g_{\star,s}^4(T_{\rm v})\,g_\star^{-3}(T_{\rm v})}{100}\right)^{-\frac{1}{3}} \times\int_{-1}^{1}dx\int_{1}^{\infty}dy\mathcal{P}_\zeta\left(\frac{y-x}{2}k\right)\mathcal{P}_\zeta\left(\frac{y+x}{2}k\right)F(x,y)|_{k=2\pi f}\,, \tag{1.91}$$

$$F(x,y) = A(x,y)\Big\{\left[x^2-y^2+\frac{x^2+y^2-6}{2}\ln\left(\left|\frac{y^2-3}{x^2-3}\right|\right)\right]^2 +\frac{\pi^2(x^2+y^2-6)^2}{4}\theta\left(y-\sqrt{3}\right)\Big\}\,, \tag{1.92}$$

$$A(x,y) = \frac{(x^2+y^2-6)^2(x^2-1)^2(y^2-1)^2}{(x-y)^8(x+y)^8}\,. \tag{1.93}$$

The concrete derivation of this expression is a rather laborious exercise, and more details can be found in [31–33]. The basic recipe to obtain scalar-induced metric perturbations requires the expansion of the metric tensor in terms of small perturbations up to *second* order. The fundamental reason behind this is that only combinations of scalar perturbations (spin-0 fields) can source tensor perturbations (spin-2 fields), i.e., the perturbative expansion must feature terms including products of scalar fields.

Note that Eq. (1.91) is formally only valid if the inflationary period is directly followed by a radiation-dominated era. This means that its usage is appropriate in the scenario of instant reheating of the primordial plasma where there is no intermediate matter-dominated era through background field oscillations around the true vacuum. We will later put this more into context in Sec. 4.3.

1.3 Aspects of Finite-Temperature Field Theory & Phase Transitions

Since our principal research objective is the study of the dynamics of a cosmological phase transition, we must introduce the appropriate framework to describe and characterize phase transitions themselves and put them into the context of cosmology thereafter. Since phase transitions are phenomena of physical systems with an enormous amount of dofs, we will first turn towards statistical physics and move on to its relativistic, field-theoretical extension, namely *finite-temperature field theory*.

Note that we will work in natural units here again; we therefore set the Boltzmann constant to $k_\mathrm{b} = 1$.

1.3.1 Elements of Statistical Physics

Statistical physics allows us to describe the *macroscopic equilibrium properties* of a physical system of (infinitely) many dofs with only a few *thermodynamic variables* such as temperature T, pressure P, volume V, and number density N. It simply requires the initial specification of the microscopic interactions of the dofs $\Phi \equiv \{\Phi_i(\boldsymbol{x})\}$ present in the system through a Lagrangian $\mathcal{L}(\Phi, \partial\Phi)$ or equivalently a Hamiltonian $\mathcal{H}(\Phi, P)$. The underlying symmetries of the system will dictate the most general expression for $\mathcal{L}$ or $\mathcal{H}$. All physical information of this system is then incapsulated in the *central* quantity, namely the *partition function* $\mathcal{Z}[J, T, V, N]$, which corresponds to the sum of all possible configurations of the system in the presence of some general external fields $J \equiv \{J_i(\boldsymbol{x})\}$. Its concrete shape will depend on what kind of statistical ensemble (microcanonical, canonical, grand-canoncial) we will consider for our system. Here, we will concentrate on the last two, where the system is additionally connected to a thermal bath with which it can exchange only heat ($\langle T\rangle|_V =$ const.) or heat and particles ($\langle T\rangle|_V =$ const. $= \langle N\rangle|_\mathrm{V}$), respectively. Ensemble average of physical observables, i.e., the dofs $\Phi_i(\boldsymbol{x})$, can be computed by summing over all its possible configurations, weighted by the corresponding Boltzmann factor depending on $\mathcal{H}(\Phi, P)$.

The system's possible configurations are described by the so-called *thermodynamical potentials*, which can all be obtained through derivatives of $\mathcal{Z}$ and and consequently depend on a set of *thermodynamic variables*. Depending on the problem at hand, it may be more useful to work with a different set and therefore different potential. They are related to each via a so-called *Legendre-Fenchel (LF) transformations*[16]. In the following derivations, we will supress the notation of all thermodynamic variables expect for T and V. Let us give account of the most important thermodynamic potentials:
The ***Helmholtz free energy density*** f, which is given by

$$f\,[J,T] = \lim_{V\to\infty} \frac{1}{V} F[J,T] = \lim_{V\to\infty} \frac{1}{V}\left(-T\,\ln\left(\mathcal{Z}[J,T]\right)\right). \tag{1.94}$$

[16] A more thorough discussion on this type of transformation and its impact on the structure of a function weill be elaborated in Appendix A

It is a *convex* function[17], which is *continuous* and *almost everywhere differentiable*, meaning that its derivative may jump discontinously at a finite number of points. This formality plays a major role when it comes to dicsussing phase transitions and will be explained later on. As previously mentioned, the Helmholtz free energy density can be obtained by a LF transformation of the *internal energy* $E[\Phi, J, S]$ via

$$f\,[J,T] = \lim_{V\to\infty} \frac{1}{V} \sup_{S} \Big(E[J,S] - T\cdot S \Big)\,, \tag{1.95}$$

where $S = S(T)$ is the *entropy*, and $T \equiv \partial_S E|_V$ is the (ensemble) temperature.
Another crucial thermodynamic potential is the *Gibbs free energy density* g, which can be recovered from f via a LF transform[18],

$$g[\varphi, T] = \lim_{V\to\infty} \frac{1}{V} \sup_{J} \Big(f[J,T] - J\cdot\varphi \Big)\,, \tag{1.96}$$

in which the supremum singles out the specific value $J[\varphi, T]$ that satisfies

$$\varphi_i(\boldsymbol{x}) \equiv \frac{\delta f}{\delta J_i(\boldsymbol{x})}\Big|_{J[\varphi,T]} = \langle \Phi_i(\boldsymbol{x})\rangle_{\mathrm{T}}\,. \tag{1.97}$$

Since the last expression in the above equation corresponds to the ensemble average of our dof at a fixed temperature T, we may refer to $\varphi_i(\boldsymbol{x})$ as the *average* or *mean field* [19]. Note that φ and J become conjugated variables in this context.

We continue by defining also the *isothermal susceptibility* $\chi_{T,i}$ as

$$\chi_{T,i}(\boldsymbol{x},\,\boldsymbol{y}) \equiv \frac{\delta^2 f}{\delta J_i(\boldsymbol{x})\delta J_i(\boldsymbol{y})}\Big|_{J[\varphi,T]} = \left(\frac{\delta^2 g}{\delta\varphi_i(\boldsymbol{x})\delta\varphi_i(\boldsymbol{y})}\Big|_{T} \right)^{-1}\,, \tag{1.98}$$

which is directly proportional to the *spatial correlator* $G_{T,i}(x,y)$ [35],

$$\begin{aligned} G_{T,i}(\boldsymbol{x},\,\boldsymbol{y}) &\equiv \langle \Phi_i(\boldsymbol{x})\,\Phi_i(\boldsymbol{y})\rangle_{\mathrm{T}} - \langle \Phi_i(\boldsymbol{x})\rangle_{\mathrm{T}}\cdot\langle \Phi_i(\boldsymbol{y})\rangle_{\mathrm{T}} \\ &= \frac{1}{Z}\frac{\partial^2 f}{\partial J_i(\boldsymbol{x})\partial J_i(\boldsymbol{y})}\Big|_{T} = T\cdot\chi_{T,i}(\boldsymbol{x},\,\boldsymbol{y})\,, \end{aligned} \tag{1.99}$$

whose function it is to measure the correlation of fluctuations of our dofs (fields) Φ_i at the spacetime points $\boldsymbol{x}$ and $\boldsymbol{y}$ with respect to their average values $\varphi_i(\boldsymbol{x})$ and $\varphi_i(\boldsymbol{y})$, respectively. Eq. (1.99) represents an important result from *linear response theory*, in which one can understand how a statistical system reacts in the presence of small fluctuations through the study of its *response functions*.

[17] See Appendix A for the definition of a convex function.

[18] The compactified notation in Eq. (1.96) is to be interpreted as the simultaneous LF transform of a number n of individual external fields, such that e.g., the last term is $\sum_i^n J_i(\varphi_i)\cdot\varphi_i$.

[19] In the standard literature (like [35]), this quantity is also commonly referred to as *average magnetisation* $M(H)$ in the presence of an external magnetic field H due to its interpretation of the average spin in, e.g., Ising spin models.

Note that for translationally-invariant systems, the spatial correlator only depends on the difference $|\boldsymbol{x}-\boldsymbol{y}|$ such that we can write

$$\begin{aligned} G_{T,i}(\boldsymbol{x},\,\boldsymbol{x}) &= G_{T,i}(\boldsymbol{x}-\boldsymbol{x}) = G_{T,i}(\boldsymbol{0}) \\ &= \langle \Phi_i(\boldsymbol{0})\,\Phi_i(\boldsymbol{0})\rangle_{\mathrm{T}} - \langle \Phi_i(\boldsymbol{0})\rangle_{\mathrm{T}} \cdot \langle \Phi_i(\boldsymbol{0})\rangle_{\mathrm{T}} \\ &= \langle \Phi_i^2(\boldsymbol{0})\rangle_{\mathrm{T}} - \langle \Phi_i(\boldsymbol{0})\rangle_{\mathrm{T}}^2 \\ &= \mathrm{Var}(\Phi_i) = T\cdot\chi_{T,i}(\boldsymbol{0})\,, \end{aligned} \tag{1.100}$$

where we have related the *variance* of the dof field Φ_i to the *static* isothermal susceptibility $\chi_{T,i}(\boldsymbol{0})$.

Stability of Equilibrium Configurations

A *stable equilibrium state* of a statistical system at a given temperature T is a configuration $\varphi_{\mathrm{eq},T}$ which minimises the Gibbs free energy (density) *globally*, i.e.,

$$\frac{\delta g(\varphi,T)}{\delta\varphi}\Big|_{\varphi_{\mathrm{eq},T}} = 0\,, \quad \chi_T^{-1} = \frac{\delta^2 g(\varphi,T)}{\delta\varphi^2}\Big|_{\varphi_{\mathrm{eq},T}} > 0\,. \tag{1.101}$$

Note that the last expression is to be identified as the *stability requirement*, which is automatically ensured by the aforementioned convexity property.

Later we will further extend the notion of stability when working with the so-called Landau free energy (density) in Sec. 1.3.3 (or the constraint effective potential in Sec. 1.3.4), which is a very useful quantity to study cosmological phase transitions that is *related but not equal* to the Gibbs free energy (density).

1.3.2 Characterisation of Phase Transitions

In nature, a statistical physical system might manifest in different ways. The number of such distinct *phases* as well as the type of the *phase transitions* that lie between them is mostly determined by the dimensionality and symmetries of the underlying theory. Oftentimes, the possible phases of the system can be characterized by the presence *or* absence of symmetries, i.e., the stable equilibrium or ground state does *or* does not respect the symmetries of the microscopical theory. The transition from one to another is then driven by a mechanism referred to as *spontaneous symmetry breaking*, and happens at a characteristic temperature scale called the *critical temperature* T_{c}. In the modern approach, one generally distinguishes between two major types of phase transitions:

I **First-order (or *discontinous*) phase transition (FOPT)**: The first-order derivative of the Helmholtz free energy density f w.r.t. the temperature T exhibits a discontinuous jump[20]at $T = T_{\mathrm{c}}$,

$$\epsilon_T \equiv \left| \frac{\partial f}{\partial T}\Big|_{T\to T_{\mathrm{c}}^+} - \frac{\partial f}{\partial T}\Big|_{T\to T_{\mathrm{c}}^-} \right| > 0\,, \tag{1.102}$$

where ϵ_T is called the *latent heat* that is released during such a transition. All higher derivatives of f w.r.t. the temperature (and other thermodynamic variables) are however finite at T_c. Phenomenologically, the transition proceeds by a phase separation mechanism which typically features the nucleation of spherically symmetric spatial (or spacetime) configurations, often called *critical bubbles* or *nuclei*, which converts the system to the new phase through their expansion that is driven by the latent heat. Note that since these nucleating bubble structures have a characteristic size, namely its radius R, the system exhibits a characteristic length scale, which renders this kind of transition an anisotropic process. A more thorough explanation will be given in Sec. 1.4

As will be clear from the dicussion in Appendix A, the non-analyticity in the Helmholtz free energy density f through the discontinuous jump in its derivative $\partial_T f|_{T_\mathrm{c}}$ will naturally reflect in the Gibbs free energy density g as a *section of constant slope* equal to the value of the latent heat ϵ_T. This specific section also marks the region of stable phase coexistence.

II ***Continuous*** **phase transition (CPT):** Eventhough the first derivative of f w.r.t. the temperature T is continuous, which directly implies the absence of latent heat, its higher-order derivatives show discontinuities at $T = T_\mathrm{c}$. We further divide this case into two subsclasses:

II.A *Second-order phase transitions:* The heat capacity C_V (second derivative of f w.r.t. the temperature T) as well as the susceptibility $\chi_{T,i}$ (second derivative w.r.t. the externl field J_i) diverge at $T = T_\mathrm{c}$,

$$\lim_{T\to T_\mathrm{c}^\pm} C_\mathrm{V}(T) \;=\; \lim_{T\to T_\mathrm{c}^\pm} \frac{\partial^2 f}{\partial T^2}\Big|_T \;\to\; \infty\,, \tag{1.103}$$

$$\lim_{T\to T_\mathrm{c}^\pm} \chi_{T,i} \;=\; \lim_{T\to T_\mathrm{c}^\pm} \frac{\delta^2 f}{\delta J^2}\Big|_{J[\varphi,T]} \;\to\; \infty\,. \tag{1.104}$$

Interestingly, the divergence of $\chi_{T,i}$ is not caused by the divergence of the spatial correlator $G_{T,i}$ (see Eq. (1.99)) itself but the divergence of the so-called *correlation length* ξ, which specifies the spatial decay of $G_{T,i}$ and thus describes the typical spatial scale over which fluctuations of the dof fields Φ are correlated. This means that at the critical temperture the system experiences the *growth and correlation of fluctuations at all length scales*, which drives the transition of the system towards the new phase. This can also be explicitly seen in Eq. (1.100) (and even already in the context of Eq. (1.47)), in which an increasing fluctuation growth at T_c leads to the divergence of the variance.

[20] Remember that this is not surprising since the convexity of f does not guarantee differentiability everywhere.

Thus, no anisotropies are generated during this type of transition. The aforementioned aspects can be summarized as *critical behaviour*: when approaching T_c, physical observables follow power-law relations dictated by the so-called *critical exponents* determining *how exactly* a certain observable diverges. Miraculously, the critical behaviour of a system is dictated by the *universality class* it belongs to, which is *solely* determined from its dimensionality and symmetries. Clearly, this means that different theories of ranging complexity which share these two features will exhibit the same critical behaviour.

II.B *Crossover transitions:* All derivatives of f are finite at $T = T_\mathrm{c}$, and instead of featuring divergencies, the heat capacity, susceptibility, and correlation length show (finite) peaks at the critical temperature. This case constitutes a literally *smooth* transition from one phase to another, and therefore does not source anisotropies of any kind as well.

1.3.3 Mean-field theories

Especially for the study of phase transition dynamics, it is often very common to work in a *simplified framework* in which one *only* works with *statistical averages* of the dof fields and thus consequently neglect their fluctuations (which are however quite important for critical behaviour). These reduced theories are called *mean-field theories* and allow us to explore large parts of the equilibrium thermodynamics of a statistical system, including the nature of possible phase transitions that might occur.

This approach was developed by Lev Landau and later further extended in collaboration with Vitaly Ginzburg [36,37]. The idea is fairly simple: the macroscopic properties of an ensemble are being modeled by the so-called *Landau free energy (density)* $g_\mathrm{L}(\theta, T)$, which is an *analytic* function of a *order parameter* θ[21]with a_n, whose structures are determined by the symmetries of the underlying system as well as positivity bounds,

$$g_\mathrm{L}(\theta, T) = \frac{G_\mathrm{L}}{V} = \sum_{n=0}^{\infty} a_n(T, \dots)\, \theta^n \,, \tag{1.105}$$

$$\tilde{g}_\mathrm{L}(\theta, J, T) = g_\mathrm{L}(\theta, T) - J \cdot \theta \,. \tag{1.106}$$

The functions a_n may generally depend on all relevant thermodynamic variables as well as couplings of the underlying theory. Just as in Sec. (1.3.1), we now require that the equilibrium state of the system corresponds to $\bar{\theta}(T)$, i.e., the order parameter value which minimises $\tilde{g}_\mathrm{L}$ at a given temperature T and external field value J. The inclusion of the linear θ-term in Eq. (1.106) gives us now the opportunity of studying spontaneous symmetry breaking and thus the phase transitions of the system.

[21]To make our point, we will only consider $\theta(\boldsymbol{x}) = \theta = \text{const.}$; the generalisation to spatially varying order parameters corresponds to allowing spatially varying external fields $H(\boldsymbol{x})$ and is the basis of *Ginzburg-Landau theory* [35].

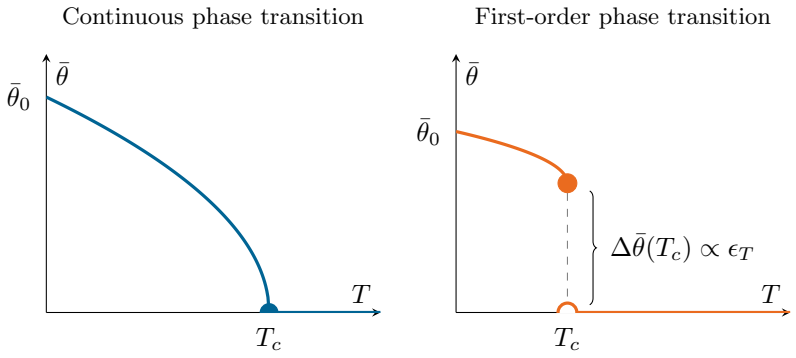

Figure 1.4: Temperature dependence of the minimising order parameter $\bar{\theta}(T)$ of the Landau free energy $g_{\mathrm{L}}[\theta, T]$ in the case of a continuous (*left*) and first-order/ discontinuous (*right*) phase transition. While the order parameter is continuous in the first case, it jumps discontinuously at $T = T_{\mathrm{c}}$ in the second case. Note that for simplicity, we have only shown the limiting case $J \to 0^+$.

A continuous phase transition is relaized by $\bar{\theta}(T)$ being a *continuous* function in T as can be seen in Fig. 1.4. The minimisation of $\tilde{g}_{\mathrm{L}}$ yields two possible solutions $\pm\bar{\theta}(T)$, which minimise $\tilde{g}_{\mathrm{L}}$ *equally*. Which one of them is eventually picked by the system depends on the external field value $J > J_c$ or $J < J_c$. The symmetry is said to be broken at the critical external field J_c for $T \to T_{\mathrm{c}}$. For example, the solution for $\bar{\theta}(T)$ for theories in the Ising universality class is given by [35]

$$\bar{\theta}(T) \quad \begin{cases} = 0\,, & T > T_{\mathrm{c}}\,, \\ \propto \pm\sqrt{T_{\mathrm{c}} - T}\,, & T \geq T_{\mathrm{c}}\ (J \to 0^{\pm})\,. \end{cases} \tag{1.107}$$

From this point, one is also able to calculate the so-called *mean-field critical exponents*, which do not have to coincide with the true critical exponents of the system since fluctuations crucial to criticality are not included from the start. It is important to note that for every theory, one can define a *critical dimension* $d > d_c(\alpha, \beta, \gamma)$[22] above which the system's simplified mean-field description becomes exact.

On the other hand, a first-order phase transition occurs in this picture if the order parameter exhibits a discontinuous jump at the critical temperature. The height of the jump is then proportional to the latent heat ϵ_T released in the transition. This time, we obtain two *unequally minimising* solutions, $\bar{\theta}_1(T)$ and $\bar{\theta}_2(T)$, as well as a maximising solution $\bar{\theta}_{\max}(T) \in [\bar{\theta}_1(T), \bar{\theta}_2(T)]$. In a similar manner, the value of the external field picks out which of the two minima is the *local* and which is the *global* minimum of $\tilde{g}_{\mathrm{L}}$ by tilting the function accordingly via the linear θ-term in Eq. (1.106). Pictorially, this corresponds to a local minimum being separated from a global minimum by a *thermal barrier*, as depicted in Fig. 1.3.3. Note that this non-analytic behaviour of the order

[22] Here, $\{\alpha, \beta, \gamma\}$ are some of the critical exponents of the theory; see [35] for their definition.

parameter can only be induced by symmetry-breaking terms in $g_{\mathrm{L}}(\theta, T)$, e.g., cubic θ-terms in $\mathbb{Z}_2$-symmetric theories. One possible solution for $\bar{\theta}(T)$ then reads

$$\bar{\theta}(T) \quad \begin{cases} = 0\,, & T > T_{\mathrm{c}}\,, \\ = \pm\theta_c \neq 0\,, & T = T_{\mathrm{c}}\ (J \to 0^{\pm})\,, \\ = \pm\bar{\theta}(T)\,, & T \geq T_{\mathrm{c}}\ (J \to 0^{\pm})\,. \end{cases} \tag{1.108}$$

Despite its resemblence with the Gibbs free energy g in Eq. (1.96) (if we identify θ as φ), it is *essential* to understand that these two objects are *not* equal. This comes from the fact that, *by construction*, g_{L} is not necessarily convex and therefore must not satisfy the identity in Eq. (1.97). However, one can show that g is the *convex hull* of g_{L},

$$g[\theta, J, T] = \sup_{\theta} \left(g_{\mathrm{L}}(\theta, T) - \theta \cdot J \right)\,, \tag{1.109}$$

which means that the two functions are only equal in the intervals where $\delta^2 g / \delta\varphi^2 > 0$, which naturally employs the stability condition on the possible equilibrium states (see also Eq. (1.101)). More precisely, if $\bar{\theta}_1$ and $\bar{\theta}_2$ are both minima of a general $\tilde{g}_{\mathrm{L}}$, the property of the convex hull imposes

$$\partial_\theta^2 \tilde{g}_{\mathrm{L}}(\theta \in [\bar{\theta}_1, \bar{\theta}_2], J,\, T) \overset{!}{\geq} 0 \tag{1.110}$$

$$\Leftrightarrow \int_{\bar{\theta}_1}^{\bar{\theta}_2} d\theta\ \partial_\theta^2 \tilde{g}_{\mathrm{L}}(\theta, J_c,\, T) \;=\; \partial_\theta \tilde{g}_{\mathrm{L}}(\bar{\theta}_2, J_c,\, T) - \partial_\theta \tilde{g}_{\mathrm{L}}(\bar{\theta}_1, J_c,\, T)$$

$$\geq \Delta\bar{\theta}(T) = \text{const.} \tag{1.111}$$

$$\Leftrightarrow\ \tilde{g}_{\mathrm{L}}(\theta, J,\, T) \geq -J_c \cdot \theta \text{ for } \theta \in [\bar{\theta}_1, \bar{\theta}_2]\,, \tag{1.112}$$

which is a different notation for the *Maxwell-* or *common tangent construction* from classical statistics, describing the region of stable phase coexistence [35]. It means that the *true* Gibbs free energy g is a linear function with slope J_c interpolating between the two minima of $\tilde{g}_{\mathrm{L}}$, marking the boundaries of the (temperature-dependent) region of stable phase coexistence, i.e., $[\bar{\theta}_1(T), \bar{\theta}_2(T)]$.

Note that this also means that g and $\tilde{g}_{\mathrm{L}}$ contain the same physical information, but $\tilde{g}_{\mathrm{L}}$ even allows us to further extend the stability definition of an equilibrium state, which is extremely useful in the later analysis of cosmological phase transitions (see Sec.1.4).

Mean-field stability definition of equilibrium states The set of all equilibrium states $\{\bar{\theta}_T\}$ is defined by their property of extremising the Landau free energy g_L, i.e.,

$$\theta_T \in \{\bar{\theta}_T\} \;\Leftrightarrow\; \partial_\theta g_\mathrm{L}(\theta, T)|_T = 0\,. \tag{1.113}$$

We now may further classify them with regards to their stability:

I **Stable (true) equilibrium:** θ_T minimises g_L *globally*, and $\partial_\theta^2 g_\mathrm{L}|_T > 0$,

II **Metastable (false) equilibrium:** θ_T minimises g_L *locally*, and $\partial^2 g_\mathrm{L}|_T > 0$,

III **Unstable equilibrium:** θ_T maximises g_L, and $\partial^2 g_\mathrm{L}|_T \leq 0$.

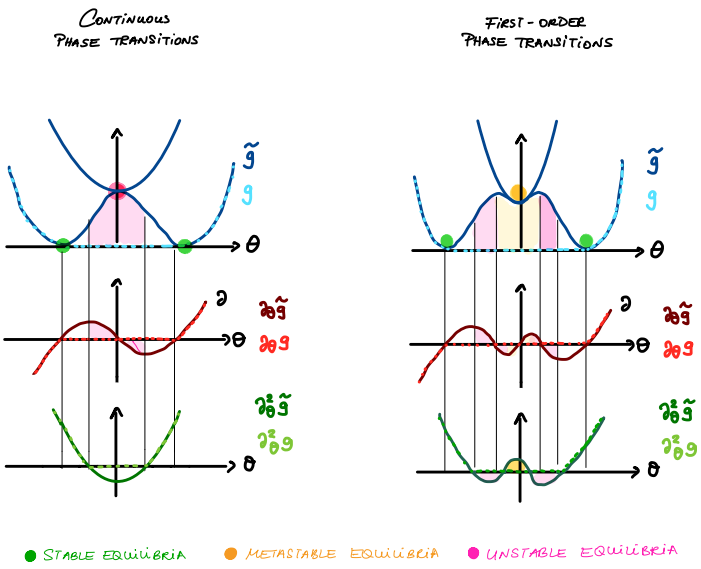

Figure 1.5: **Summary sketch of the phase transitions classification à la Landau.**
Left: Continuous phase transitions feature continuous order parameters, especially at the critical temperature T_c. The Landau free energy g_L exhibts one stable equilibrium in the symmetric phase $T > T_\mathrm{c}$, and (at least) two degenerate stable equilibria in the broken phase $T < T_\mathrm{c}$, separated by an unstable equilibrium configuration.
Right: First-order phase transitions exhibit a discontinuous jump in the order parameter at the critical temperature T_c, which is related to the latent heat released during the transition. g_L typically features metastable and stable equilibria configurations.

1.3.4 From classical to quantum fields at $T > 0$: Finite-temperature field theory

How is it now possible to make contact to a scenario featuring infinitely many *relativistic* and *quantized* dofs at a non-zero temperature T from the very general framework we have previously introduced?
The key lies in the following observation: We can write a QFT on a Minkowskian spacetime (here in 4 dimensions) as a euclidean QFT[23] via the introduction of the *imaginary-time formalism*, i.e., $t \to \tau = -it$, formally realised by performing a Wick rotation. What we end up with is a well-defined euclidean path integral expression for the *generating functional* Z_{E} of the correlation functions, namely

$$Z_{\mathrm{E}}[J] = e^{-V \cdot W_{\mathrm{E}}[J]} = \int \mathcal{D}\Phi \; e^{-S_{\mathrm{E}}[\Phi] - (J,\Phi)} \,, \text{[24]} \tag{1.114}$$

$$\Leftrightarrow \; W_{\mathrm{E}}[J] = -\frac{1}{V} \ln\left(Z_{\mathrm{E}}[J]\right) = -\frac{1}{V} \ln\left(\int \mathcal{D}\Phi \; e^{-S_{\mathrm{E}}[\Phi] - (J,\Phi)} \right) , \tag{1.115}$$

where J is called the *external soruce* or *field*, and $S_{\mathrm{E}}[\Phi]$ is the *euclidean* classical action depending on the Lagrangian $\mathcal{L}_{\mathrm{E}}(\Phi, \partial\Phi)$ defined on a *euclidean* spacetime $E^4 = \mathbb{R}^4$ with signature $(+,+,+,+)$,

$$S_{\mathrm{E}}[\Phi] = \int d^4\boldsymbol{x} \; \mathcal{L}_{\mathrm{E}}(\Phi, \partial\Phi) = \int d^4\boldsymbol{x} \left\{ \frac{1}{2} \left[(\partial_\tau \Phi)^2 + (\nabla\Phi)^2 \right] + V(\Phi) \right\} , \tag{1.116}$$

where after the last equal sign we have shown the explicit form in the case of a real scalar field theory, which we will use henceforth as an pedagocial example. *Expectation values* as well as *correlation functions* may now be computed by taking of functional derivatives of W_{E}, the *euclidean* generating functional of all connected correlation functions,

$$G_{\mathrm{E},c}(x_1, \ldots, \boldsymbol{x}_n) = \langle \Phi(\boldsymbol{x}_1) \cdots \Phi(\boldsymbol{x}_n) \rangle_J \;\equiv\; \frac{\delta^n W_{\mathrm{E}}[J]}{\delta J(\boldsymbol{x}_1) \cdots \delta J(\boldsymbol{x}_n)} \,, \tag{1.117}$$

or the effective action Γ_{E}, the generator of all 1PI correlation functions and defined as the Legendre-Fenchel transform of $W_{\mathrm{E}}[J]$, i.e.,

$$\Gamma[\varphi_J(\boldsymbol{x})] = \sup_J \left(W_{\mathrm{E}}[J] - \int d\boldsymbol{x} \; \varphi_J(\boldsymbol{x}) \cdot J(\boldsymbol{x}) \right) , \tag{1.118}$$

where φ *is* the expectation value of the quantum field Φ in the presence of the external source J,

$$\varphi_J(\boldsymbol{x}) \;=\; \frac{\delta W_{\mathrm{E}}[J]}{\delta J(\boldsymbol{x})}\Big|_{J[\varphi_J(\boldsymbol{x})]} \;\equiv\; \langle \Phi(\boldsymbol{x}) \rangle_J \,. \tag{1.119}$$

[23] This is strictly only possible if the Minkowskian QFT satisfies the *Wightmann axioms* [38]. The inverse case, i.e., the existence of a Minkowskian counterpart to a euclidean QFT, is only guaranteed if the Osterwalder-Schrader theorem [39] is applies.

[24] As in the standard literature [40], the notation (J, Φ) denotes $(J, \Phi) \equiv \int d\boldsymbol{x} \; J(\boldsymbol{x}) \cdot \Phi(\boldsymbol{x})$.

The solution to the quantum EOMs is given by minimisation of Γ_{E},

$$\frac{\delta\Gamma_{\mathrm{E}}[\varphi_J(\boldsymbol{x})]}{\delta\varphi_J(\boldsymbol{x})}\Big|_{\varphi(J(\boldsymbol{x}))} = -J(\boldsymbol{x})\,, \tag{1.120}$$

where we notice that in the case of a vanishing external source, $J = 0$, we end up with the *vacuum expectation value (VEV)* $\langle\Phi(\boldsymbol{x})\rangle_0$, ground state of the theory.[25] Note that the translational invariance of the systems we will henceforth consider enforce their VEVs to be constant, $\langle\Phi(\boldsymbol{x})\rangle_0 = \text{const.}$. If we evaluate $\Gamma_{\mathrm{E}}[\varphi_J(\boldsymbol{x})]$ at constant configurations, i.e., $\varphi_J(\boldsymbol{x}) \equiv \varphi$, we obtain a new crucial quantity called the *quantum effective potential* $U(\varphi)$,

$$U(\varphi) \;\equiv\; \frac{1}{V}\,\Gamma_{\mathrm{E}}[\varphi_J(\boldsymbol{x}) = \varphi]\,, \tag{1.121}$$

This is now a function of the quantum expectation value in the presence of a *constant* external source $J(\varphi_J(\boldsymbol{x})) \equiv J$, and following Eq. (1.120), the VEV will be simply given by its (*global*) minimum,

$$\partial_\varphi U(\varphi)\Big|_{\varphi_0=\langle\Phi(\boldsymbol{x})\rangle_0} = 0\,. \tag{1.122}$$

If we want to describe this quantum field theoretical system within a mean-field approach, we may also define the ***constraint effective potential*** $U_{\mathrm{con}}(\varphi)$ [41–43] through

$$U_{\mathrm{con}}(\varphi) \equiv -\frac{1}{V}\,\ln\left[\int \mathcal{D}\Phi\;\delta\left(\frac{1}{V}\int\; d^4\boldsymbol{x}\;\Phi(\boldsymbol{x}) - \varphi\right)\; e^{-S_{\mathrm{E}}[\Phi]}\right]\,, \tag{1.123}$$

$$= -\frac{1}{V}\,\ln\left[\int\; \mathcal{D}\,\varphi'(\boldsymbol{x})\; e^{-S_{\mathrm{E}}[\Phi=\varphi+\varphi'(\boldsymbol{x})]}\right]\,, \tag{1.124}$$

$$Z_{\mathrm{E}}[J] = e^{-V\cdot W_{\mathrm{E}}[J]} = \int_{-\infty}^{\infty}\; d\varphi\; e^{-V\,(U_{\mathrm{con}}(\varphi)\,-\,J\cdot\varphi)}\,, \tag{1.125}$$

$$W_{\mathrm{E}}[J] = \sup_{\varphi}\,(U_{\mathrm{con}}(\varphi) - J\cdot\varphi)\;. \tag{1.126}$$

where we have used the decomposition of the quantum field $\Phi(\boldsymbol{x})$ into its Fourier modes,

$$\Phi(\boldsymbol{x}) = \int\; d\boldsymbol{P}\; e^{i\boldsymbol{P}\cdot\boldsymbol{x}}\;\tilde{\Phi}(\boldsymbol{P}) \tag{1.127}$$

$$= \tilde{\Phi}(\boldsymbol{P}=\boldsymbol{0}) + \int_{\boldsymbol{P}\neq\boldsymbol{0}}\; d\boldsymbol{P}\; e^{i\boldsymbol{P}\cdot\boldsymbol{x}}\;\tilde{\Phi}(\boldsymbol{P}) \tag{1.128}$$

$$= \varphi + \varphi'(\boldsymbol{x})\,. \tag{1.129}$$

Again, per construction, $U_{\mathrm{con}}(\varphi)$ or $\tilde{U}_{\mathrm{con}}(\varphi, J)$ *must not be convex* since φ and J are not necessarily related to each other via a relation Eq. (1.119). It also only depends on the fields zero-mode, $\varphi \equiv \tilde{\Phi}(\boldsymbol{P}=\boldsymbol{0}) = \text{const.}$.

[25] Since Γ_{E} is a convex function, any minimum will automatically be the *global* minimum and thus the ground state.

Turning on the heat Up until now, we stayed at $T = 0$. To see the connection of a euclidean QFT to a statistical system at *thermal equilibrium*, we need to closely inspect the canonical partition function of the latter,

$$\mathcal{Z}[J,T] = e^{-F[J,T]/T} = \mathrm{Tr}_\Phi\left(e^{-(E[\Phi,T]-J\cdot\Phi)/T}\right), \tag{1.130}$$

where the trace operation $\mathrm{Tr}_\Phi(\circ)$ represents the sum over all possible field configurations. This expression does not only resemble the euclidean generating functional in Eq. (1.114) enormously, but they are actually equal if we identify the imaginary time τ with the inverse temperature $\beta = 1/T$, and impose periodic (antiperiodic) boundary conditions on the bosonic (fermionic) quantum fields from $S_\mathrm{E}[\Phi]$ in the now compactified time direction $\tau \in [0, \beta]$.

As a result, $Z_\mathrm{E}[J]/T$ obtains an interpretation as the partition function $\mathcal{Z}[J,T]$ of the quantum field theoretical system. Equivalently stated, the partition function $\mathcal{Z}$ can be expressed as a path integral, we can compute the equilibrium thermodynamics via the common perturbative (Feynman diagrams) and non-pertubative techniques (functional, lattice) from usual QFT. Most importantly, we may now identify all quantities derived from $\mathcal{Z}$, such as the thermodynamic potentials $\{f, g\}$, with their counterparts from euclidean QFT, namely the generating functionals $\{W_\mathrm{E}, \Gamma_\mathrm{E}\}$ (see also Table 1.1),

$$f[J,T] \equiv W_\mathrm{E}[J]/T\,, \quad g[\varphi_J, T] \equiv \Gamma_\mathrm{E}[\varphi_J]/T\,.^{26} \tag{1.131}$$

The *stable equilibrium* state of the system now *corresponds to its VEV* via

$$0 = \frac{1}{T}\frac{\delta\Gamma_\mathrm{E}[\varphi_J]}{\delta\varphi_J(\boldsymbol{x})}\Big|_{\varphi_0=\langle\Phi(\boldsymbol{x})\rangle_0} \overset{(1.101)}{=} \frac{\delta g[\varphi_J]}{\delta\varphi_J(\boldsymbol{x})}\Big|_{\varphi_0=\langle\Phi(\boldsymbol{x})\rangle_0}. \tag{1.132}$$

In this context, the quantum expectation values can be understood as ensemble averages at finite temperature T,

$$\langle\Phi(\boldsymbol{x}_1)\cdots\Phi(\boldsymbol{x}_n)\rangle_{J[\varphi(\boldsymbol{x}),T]}\,. \tag{1.133}$$

Lastly, by comparing Eq. (1.126) with Eq. (1.109) with each other, we may interpret the *constraint effective potential* $U_\mathrm{con}(\varphi)$ as the *Landau free energy (density)* in a mean-field description of such quantum field theoretical system in *thermal equilibrium*,

$$U_\mathrm{con}(\varphi)/T = g_\mathrm{L}(\varphi,T) \equiv V_\mathrm{eff}(\varphi,T)\,.^{27} \tag{1.134}$$

[26] Sometimes $\Gamma_\mathrm{E}[\varphi_J]/T$ is said to be equivalent to the *Helmholtz* free energy density $f[J,T]$. This statement is incorrect since Γ_E does not depend on the external source $J[\varphi(\boldsymbol{x})]$ like f, but the expectation value $\varphi_J(\boldsymbol{x})$ like g.

[27] *Important note:* In the standard literature for cosmological phase transitions, $U_\mathrm{con}(\varphi)$ is not called the *constraint effective potential*, but (only) the *effective potential*, and is typically denoted as $V_\mathrm{eff}(\varphi)$. This misleading nomenclature might suggest that $U_\mathrm{con}(\varphi)$ might be identifiable with $U(\varphi)$ and is thus also convex. The effective potential is however the *convex hull* of the constraint effective potential.

Statistical Physics	Euclidean QFT
Partition function $\mathcal{Z}[J,T]$	Generating functional $Z_{\mathrm{E}}[J]/T$
Helmholtz free energy density $f\,[J,\,T]$	Connected generating functional $W_{\mathrm{E}}[J]\,/\,T$
Gibbs free energy density $g[\varphi,\,T]$	Effective action $\Gamma_{\mathrm{E}}[\varphi]\,/\,T$
Average field $\varphi = \delta f/\delta J\vert_{J[\varphi,T]}$	Expectation value $\varphi = \delta W_{\mathrm{E}}/\delta J\vert_{J[\varphi,T]}$
External field J	External source J

Table 1.1: Listing of the quantities from statistical physics and euclidean QFT which can be identified with each other in the case a quantum field theoretical system in *thermal equilibrium*.

In the spirit of the mean-field phase transitions descriptions à la Landau (see Sec. 1.3.3), we will say a quantum field theoretical system may experience phase transitions of the following kind:

I A ***FOPT*** if the *stable equilibrium* (*global* minimum) $\bar{\varphi}(T)$ of $V_{\mathrm{eff}}(\varphi,T)$, i.e., the VEV of the system, jumps discontinuously from 0 to a non-zero value at T_{c};
We then denote the formerly stable equilibrium (at $T > T_{\mathrm{c}}$) and now *metstable* equilibrium as *false vacuum* and the new *stable* equilibrium at $T \leq T_{\mathrm{c}}$ as *true vacuum (configuration)*. The false vacuum and the true vacuum are separated by a thermal barrier (an unstable region where $\partial_{\varphi} V_{\mathrm{eff}}(\varphi,T)|_T \leq 0$).

II A ***continuous transition*** if the *stable equilibirum* (*global* minimum) $\bar{\varphi}(T)$ of $V_{\mathrm{eff}}(\varphi,T)$, i.e., the VEV of the system, changes continuously from 0 to a non-zero value at T_{c}; The formerly stable equilibrium at $T > T_{\mathrm{c}}$ is now an *unstable* equilibrium, whereas the new minima are now the stable equilibria of the system.

The concrete phase separating mechanisms realising the transition, such as *critical bubble nucleation* as well as *spinodal decomposition*, will be discussed in detail in Sec. 1.4 in the context of cosmological phase transitions.

Since $V_{\mathrm{eff}}(\varphi,T)$ is now defined through a path integral expression, we may apply our standard perturbative techniques to compute its contributions order by order in, e.g., the loop expansion.[28] This procedure also helps realise that the one-loop order result for $U_{\mathrm{con}}(\varphi)$ is nothing else than the *gaussian approximation* (saddle-point approximation) around the solution of the classical EOMs, i.e., $\delta S[\varphi]/\delta\varphi|_{\varphi_{\mathrm{cl}}} = 0$, which takes into account the quantum fluctuations around φ_{cl} [35].

To one-loop order, one obtains vacuum ($T = 0$) as well as thermal ($T > 0$) contributions, where the latter involve the so-called *thermal integrals* $J_{\mathrm{B,F}}$ of the type,

$$J_{\mathrm{B,F}}(x^2) = \int_0^\infty dy'\ (y')^2\ \ln\left[1 \mp \exp\left(-\sqrt{y^2+x^2}\right)\right]\,, \tag{1.135}$$

[28] See also p.158 - 159 in [43] for detailed instructions on the perturbative computation, and Sec. 1.4 for a concrete example.

where $-$ $(+)$ is applicable in the case of bosonic (fermionic) dofs Φ_i, and $x^2 = m_i^2(\Phi)/T^2$ involves the *effective masses* of the dofs in the system (see Sec. 1.4, 2). Two approximations to Eq. (1.135) are especially useful with regards to the description of cosmological phase transitions, namely the high-temperature (HT) regime, i.e., $T \gg m_i^2$, and the low-temperature (LT) regime, i.e., $T \ll m_i^2$.

1.4 Cosmological Phase Transitions

In the light of the previous sections, we now want to study how phase transitions in quantum field theoretical systems can impact or even alter the history of the Universe, and through which potentially observable phenomenological consequences we might be able to probe them. Here, we are especially interested in processes that source GWs, whose detection would offer a unique possibility to learn more about the (thermodynamic) conditions at very early times. Since they can only be sourced by anisotropic processes (see Sec. 1.3.2), this leaves us with FOPTs as a possible origin. Note however that such transitions cannot be realised within the SM [23, 24], such that those studies take place in the context of BSM frameworks (see, e.g., Sec. 2).

1.4.1 Cosmological FOPT and their GW Signatures

To study FOPTs in the early Universe, we will in the following consider a quantum scalar field theory on a flat FLRW metric (minimally-coupled to the gravity sector) as in Sec. 1.2, which is now additionally coupled to a thermal bath with temperature T. The quantum scalar field contributes (as a perfect fluid) to the energy content of the Universe, and thus its evolution influences the spacetime evolution by its impact on the Hubble parameter H (see Eq. (1.20)). If the quantum scalar field now underwent a phase transition, this *could* temporarily change its EOS and thus the evolution of the scale factor $a(\eta)$ (see Eq. (1.10)), modifying the standard cosmic evolution by introducing additional intermediate eras (see also Fig. 1.2).

In the following, we will stick to the mean-field theoretical description of phase transitions (see Sec. 1.3.4) via the Landau approach, and characterise them by the behaviour of the underlying model's constraint effective potential $V_{\text{eff}}(\varphi, T)$.

Phase transition dynamics

Recall that for a FOPT, we need the VEV, i.e., the global minimum of V_{eff}, to jump discontinuously at the critical temperature T_{c}. This requires the appearance of a symmetry-breaking term in V_{eff}, and it was Coleman & Weinberg [44] who first demonstrated that already the quantum one-loop corrections to the classical (tree-level) and symmetric potential $V(\varphi)$ may generate such term at $T = 0$. Here, one also refers to *spontaneous symmetry breaking by radiative corrections*. The corresponding expression for the one-loop contribution is typically referred to as *Coleman-Weinberg potential*. This new concept was later extended by Linde and collaborators [45, 46] to finite temperatures,

who also first discussed the cosmological implications of such a phase transition mechanism. Their theory of *(false) vacuum decay* describes the evolution of the background field φ from the false to the true vacuum value in a semi-classical approach. After a first step featuring a *stochastic* quantum/thermal tunneling process, where the background field φ tunnels the thermal barrier of the constraint effective potential, it classically "rolls down the potential hill" towards the true vacuum value. Mathematically, this is described by the so-called *bounce solution*, which is the field configuration solving the *bounce equation*,

$$\left(\frac{\partial^2}{\partial\tau^2} + \nabla^2\right)\varphi = \partial_\varphi V'_{\text{eff}}(\varphi, T) \tag{1.136}$$

for the explicit boundary conditions

$$\text{a)} \lim_{\tau\to\pm\infty} \varphi(\tau, \mathbf{x}) = \varphi_{\text{false}}, \qquad \text{b)} \; \partial_\tau\varphi(\tau = 0, \mathbf{x}) = 0. \tag{1.137}$$

Often, one can show that the bounce solution should exhibit $O(N)$-symmetry,[29] rendering it a function of only one "radial" spacetime coordinate $r = \sqrt{\tau^2 - \boldsymbol{x}^2}$. Evidently, the bounce corresponds to a spherically symmetric field configuration interpolating between the false and the true vacuum, and can therefore be interpreted as nucleating and expanding *(true) vacuum bubbles*. Thus cosmological FOPT typically proceed by a phase separation mechanism called *bubble nucleation*: the whole spacetime becomes filled with nucleating bubbles, whose expansion is powered by the released latent heat, which will eventually collide and fill more and more Hubble patches in the Universe with the true vacuum. Since bubble nucleation is a stochastically process, its probability is given by the *false vacuum decay rate* at a given temperature T [43],

$$\frac{\Gamma(T)}{\mathcal{V}} \;\simeq\; T^4 \left(\frac{\mathcal{S}_3(T)}{2\pi T}\right)^{\frac{3}{2}} \exp\left(-\frac{\mathcal{S}_3(T)}{T}\right), \tag{1.138}$$

where $\mathcal{V}$ is the spacetime volume, and $\mathcal{S}_3$ is the three-dimensional Euclidean action evaluated at the bounce field configuration, i.e.,

$$\mathcal{S}_3(T) = 4\pi \int dr\; r^2 \left[\frac{1}{2}\left(\frac{d\varphi}{dr}\right)^2 + \Big(V_{\text{eff}}(\varphi, T) - V_{\text{eff}}(\varphi_{\text{false}}, T)\Big)\right]. \tag{1.139}$$

The completion of the phase transition then depends on the ratio between the false vacuum decay rate and the Hubble parameter describing the expansion rate of the Universe,

$$\frac{\Gamma_{\text{v}}}{H^4} \quad \begin{cases} \geq 1 : & \text{Successful bubble nucleation \& collision,} \\ \leq 1 : & \text{Extended inflation scenario.} \end{cases} \tag{1.140}$$

[29] The specific symmetry group depends on whether one studies phase transitions at zero temperature ($O(4)$), or at finite temperatures ($O(3)$).

In the first scenario, the false vacuum decays sufficiently rapidly to allow bubble nucleation and subsequent collisions to occur. In contrast, in the second scenario, the expansion of spacetime proceeds too quickly for such collisions to take place. We further define the effective bubble nucleation temperature $T_{\rm n}$ via $\Gamma_{\rm v}(T_{\rm n}) \sim H^4(T_{\rm n})$. The temperature scale at which we may define the FOPT to have successfully completed is refered to as *percolation temperature* $T_{\rm p}$ [47],

$$I(T) = \frac{4\pi}{3}\int_T^{T_C} \frac{dT'\,\Gamma(T')}{(T')^4 H(T')}\left(\int_T^{\tilde{T}} \frac{d\tilde{T}}{H(\tilde{T})}\right)^3 , \qquad I(T=T_\star) = 0.34\,, \tag{1.141}$$

where $p(T) = \exp(-I(T))$ is the probablity of finding a point in sapce still remaining in the false vacuum state. Note that for a successful completion via bubble nucleation, we need to require $T_{\rm p} > T_{\rm b}$, where $T_{\rm b}$ is the temperature at which the thermal barrier of the constraint effective potential disappears.

The Case of a Supercooled Universe

In some BSM models, such as the one we will study in Sec. (2), the onset of the effective bubble nucleation is delayed well below the critical temperature, i.e., $T_{\rm n} \ll T_{\rm c}$. This in turn implies that the background field φ remains "trapped" at the false vacuum for a long time. It might then occur that below a certain temperature $T_{\rm v}$, the energy density of the universe starts to be dominated by the background field's constant potential energy $V_{\rm eff}(\varphi_{\rm false}, T)$, causing the Universe to enter a period of *thermal inflation* (cf. Eqs. (1.23a) and (1.11)).[30] This is analogous to a supercooled liquid-solid transition in statistical mechanics, and we therefore call this scenario a *supercooled cosmological phase transition*. The exit from such inflationary supercooling period is then achieved by the completion of the FOPT, such that the background field approaches the true vacuum state, driven by efficient phase separation mechanism like bubble nucleation or tachyonic mode amplification (see Sec. 1.4.2).

Origins & Computation of SGWBs from FOPTs

The production of GWs requires the existence of anisotropies in the energy-momentum tensor, which in the case of FOPTs can be generated by different sources during the process, namely the collision of nucleating true vacuum bubbles as well as their impact on the surrounding plasma in the form of sound waves and turbulence in the thermal radiation bath. Due to the stochastic nature of the bubble nucleation, we would expect the GW signature to be of a SGWB. Pioneering studies involving spacetime lattice simulations [48, 49] of the latter revealed that its spectral energy density $\Omega_{GW}(f)$ can be solely parametrised by characteristic macrophysical quantities, which can be derived

[30] Here, we mean an additional inflationary period distinct from the proposed cosmic inflation period right after the BB.

from the underlying microphysical theory. Most prominently, we will encounter the FOPT transition strenght α, and inverse FOPT duration β,

$$\alpha(T) = \frac{\rho_{\rm vac}(T)}{\rho_{\rm rad}(T)} = \frac{30\Delta V_{\rm eff}(T)}{\pi^2 g_{\star,\epsilon}(T) T^4}\,, \qquad \beta = (8\pi)^{\frac{1}{3}} R_\star^{-1}\,, \tag{1.142}$$

where $\rho_{\rm vac}$ is the (false) vacuum energy density, $\rho_{\rm rad}$ is the thermal radiation energy density, and R_p is the average bubble size at the percolation temperature $T_{\rm p}$. Among others, these are some of the key quantities which enter the convenient semi-analytical templates for the GW spectral energy, which are widely used in the community today.

1.4.2 Tachyonic Phase Transition in Supercooled Universe

An interesting and less-studied situation emerges when we find the Universe in a supercooled inflationary period, *and* the VEV remains trapped at the false vacuum until the temperature scale $T_{\rm b}$, where the thermal barrier of the constraint effective potential disappears, i.e., $\varphi(\eta(T_{\rm b})) \approx 0$. Evidently, this prevents a successful completion of the FOPT via the bubble nucleation mechanism. In this case, we have

$$T_{\rm p} \to T_{\rm b}\,, \quad I \to 0\,, \tag{1.143}$$

i.e., the percolation temperature $T_{\rm p}$ reaches the temperature scale $T_{\rm b}$, causing the false vacuum decay or tunneling rate to eventually vanish. The latter prevents the further existence of bounce solutions, and thus disfavours bubble nucleation as the driving phase separation mechanism.

However, what also happens at $T \leq T_{\rm b}$ is that the curvature mass at the false vacuum first vanishes and then becomes negative,

$$0 \geq m^2\left(\varphi = 0, T \leq T_{\rm b}\right) = \partial_\varphi^2 V_{\rm eff}(\varphi, T)\big|_{\varphi=0,\, T\leq T_{\rm b}}\,. \tag{1.144}$$

for all background field configurations lying in the *spinodal* or *tachyonic field interval* $\varphi \in [-\varphi_{\rm spinodal}\,,\, \varphi_{\rm spinodal}]$ as depicted in Fig. 1.6. This phenomenon is also called a *spinodal*[31]or *tachyonic instability* in the literature [50, 51]. Recalling the mean-field stability classification from Sec. 1.3.3, this renders the false vacuum not a metastable but now a *completely unstable* vacuum configuration against small fluctuations. Since we still find ourselves in a supercooled, inflationary Universe at this temperature scale, we notice that the evolutions of the small field fluctuations around the false vacuum will follow the Mukhanov-Sasaki equation given by Eq. (1.61). By inspecting the latter's frequency more closely (see Eq. (1.62)), we find that the negative sign of the curvature

[31]In the mean-field approach of statistical mechanics, the *spinodal region* is a subregion of the stable phase coexistence region in the phase diagram of a statistical system, whose boundaries are given by the solutions $\{\varphi_{\rm spinodal}\} = \{\varphi : \partial_\varphi^2\, g(\varphi, T)|_T = 0\}$, where g is the Landau free energy. It marks the region of completely unstable mixed phase equilibria.

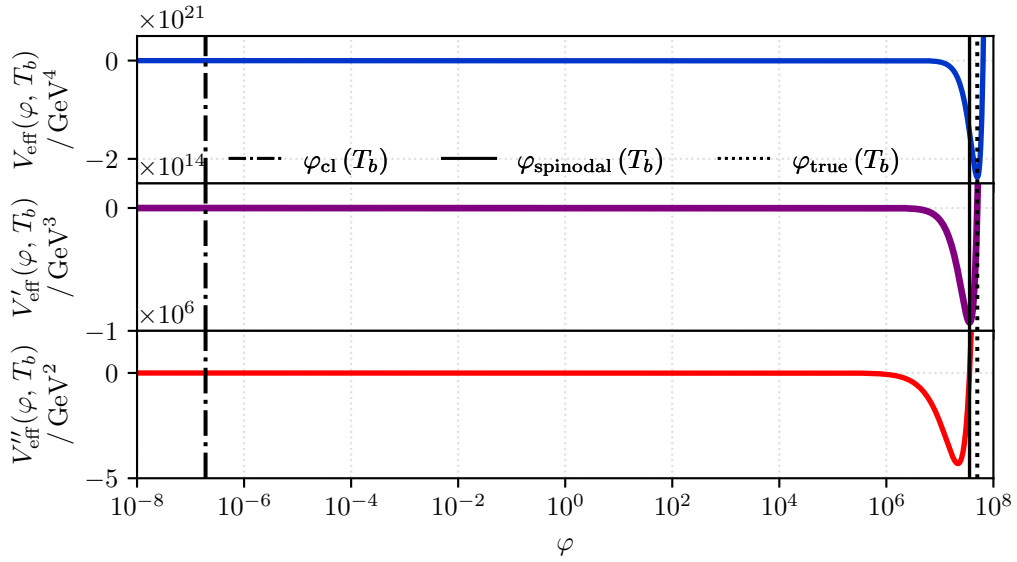

Figure 1.6: Shape of the constraint effective potential $V_{\rm eff}(\varphi, T)$ as well as its first and second derivative for $T < T_{\rm b}$. The vanishing of the thermal barrier establishes a *spinodal* or *tachyonic field region* in which the curvature mass at the false vacuum, i.e., the second derivative of $V_{\rm eff}$ at $\varphi = 0$, is negative. This marks the onset of a tachyonic phase transition, during which the background field may evolve through a number of characteristic field values: the initial false vacuum value $\varphi_{\rm false}$ (here at $\varphi = 0$), the classical transition value $\varphi_{\rm cl}$, the spinodal value $\varphi_{\rm spinodal}$, and lastly the final true vacuum value $\varphi_{\rm true}$.

mass for $T \leq T_{\rm b}$ induces an exponential growth of the superhorizon k-mode amplitudes,

$$|u_k(\eta)| \overset{T=T_b}{\longrightarrow} \propto (\eta)^{-\left(\nu(T_{\rm b})-\frac{1}{2}\right)} = \left(\frac{1}{H}\, e^{N(\eta)}\right)^{\frac{1}{2}-\nu(T_{\rm b})} \tag{1.145}$$

$$= H^{\nu(T_{\rm b})-\frac{1}{2}} \exp\left[+\left(\nu(T_{\rm b}) - \frac{1}{2}\right) N(\eta)\right] ,$$

$$\nu(T_{\rm b}) = \sqrt{\frac{9}{4} + \frac{|m^2(\varphi, T_{\rm b})|}{H^2}} , \tag{1.146}$$

whose wavenumber lie in the *tachyonic wavenumber band*

$$0 \leq k \leq m^2(\varphi \approx 0\,, T \leq T_{\rm b})\,. \tag{1.147}$$

The expression in Eq. (1.145) can be derived by considering the superhorizon limit of the general solution in Eq. (1.65) and using the Mukhanov frequency given in Eq. (1.63).

Lastly, we may definecolor the *(mode amplitude) growth factor*,

$$\Gamma_{\text{growth}}(T(\eta)) = \frac{\sqrt{|m^2(\varphi(T(\eta)),\, T(\eta))|}}{H}\,, \tag{1.148}$$

with whose help we may estimate the growth efficiency of the tachyonic mode amplitudes.

These mathematical results are in accordance with the physical interpretation of the appearance of a tachyonic instability: the false vacuum becomes thermodynamically unstable and will be detabilised by first small but then exponentially growing long-wavelength fluctuation modes, eventually converting the Universe's vacuum state to the true vacuum [52]. This special phase separation mechanism is called *spinodal decomposition* and was first studied in the context of solid-state physics [53, 54]. It is a truly anisotropic process since only k-modes satisfying Eq. (1.147) become amplified, causing the formation of clustured structures[32] in field space with a typical extent given by the (initial) characteristic length scale[33]

$$k_{\text{SD}} = H \exp\left(N_{\text{b}}\right) = H \exp\left(N(\eta(T_{\text{b}}))\right)\,. \tag{1.149}$$

The growth of tachyonic mode amplitudes can also be directly observed in the sudden increase of the scalar field's variance,

$$\text{Var}(\Phi)(\eta) = \langle\Phi^2\rangle(\eta) - \langle\Phi\rangle^2(\eta)\,, \tag{1.150}$$

for whose calculation and qualitative discussion we followingly employ the linearised approach from Eq. (1.58), i.e., $\Phi(\eta, \boldsymbol{x}) = \varphi(\eta) + \delta\phi(\eta, \boldsymbol{x})$. The exact computation of the variance would therefore require the solving of the background field and fluctuation modes evolution equations simultaneously due to their coupling via the curvature mass term $m^2(\varphi(\eta), T(\eta))$ in the mode frequency ω_k^2 in Eq. (1.62).

However, in the initial phase of the thermal inflation period *before* the appearance of the tachyonic instability at T_{b}, we can assume that the VEV remains trapped at the false vacuum, i.e., $\varphi(\eta) = \langle\Phi\rangle(\eta) \approx 0$, such that the fluctuation mode evolutions decouple from the background field, yielding

$$\text{Var}(\Phi)(\eta) \approx \langle(\delta\phi)^2\rangle(\eta) = \langle(\delta\phi)^2\rangle_0(\eta) + \langle(\delta\phi)^2\rangle_T(\eta) \tag{1.151}$$

$$= \int_H^{a(\eta)H} \frac{k^2\, dk}{2\pi^2 a^2}\, |u_k(\eta)|^2 + \int_H^{\infty} \frac{k^2\, dk}{\pi^2 a^2}\, n_k(T)\, |u_k(\eta)|^2\,, \tag{1.152}$$

where $n_{\text{k}}(T)$ denotes the Bose-Einstein distribution from Eq. (1.87), $\langle(\delta\phi)^2\rangle_0$ and $\langle(\delta\phi)^2\rangle_T$ are the vacuum and thermal variance contributions, respectively, and $|u_k(\eta)|$ are the mode amplitude solutions from the Amplitude-Mukhanov Sasaki Equation (1.78) with $\omega_k^2(m^2(\varphi = 0))$. While at first the thermal contribution will clearly dominate, the emergence of the tachyonic instability at T_{b} will especially make the vacuum contribution

[32] See also [55] for lattice simulations showing the phase separation via spinodal decomposition.

[33] Here, the subscript "SD" in k_{SD} stands for spinodal decomposition.

grow significantly, signalising the onset of a *tachyonic phase transition*. From this moment onwards, it becomes inaccurate to assume that the background field remains at the false vacuum, and thus its evolution has to be appropriately taken into account. For this purpose, we can purpsue a simplifying ansatz where we roughly estimate the end of the quantum regime, measured by the background field value $\varphi_{\rm cl}$ (see Eq. (1.25)) beyond which the classical background field evolution starts to dominate the quantum fluctuations. If $\varphi_{\rm cl}$ is still very close to zero, we may well approximate the background field evolution for temperatures below $T_{\rm b}$ until $T_{\rm cl}$ as

$$\varphi(\eta(T)) \approx \sqrt{\langle(\delta\phi)^2\rangle(\eta(T))} \quad \text{for } T \in [T_{\rm cl}\ T_{\rm b}]\,, \qquad \varphi(\eta(T_{\rm cl})) = \varphi_{\rm cl}\,. \tag{1.153}$$

Consequently, this expression then needs to be used in the curvature mass term in the modes' frequencies for $T < T_{\rm b}$. The great (numerical) advantage of this ansatz is that is leaves the fluctuation modes decoupled from the background field while still accounting for the latter's impact on the modes' growth factor.

Note again that the linearised treatment introduced in Eq. (1.58) has intrinsic limitations in capturing the complete dynamics of the scalar field. Specifically, it is valid only within the *linear regime* of the evolution, i.e., during the initial stage in which the fluctuation modes can be treated as evolving independently. At later times, particularly during reheating, nonlinear effects become important. In this phase, interactions between different fluctuation modes as well as their backreaction on the homogeneous background field must be taken into account. A more comprehensive analysis would therefore require solving the full FLRW–KG equation (cf. Eq. (1.54)) on a discretized spacetime lattice. Such an investigation is beyond the scope of the present work and is deferred to future study.

About the remaining Fate of the Universe

Within our framework, we can argue that the tachyonic phase transition has a chance to complete if the mode amplification is efficient enough to drive the scalar field's variance up to $\varphi_{\rm cl}$. The background field φ has then reached the point at which its evolution is dictated by the classical "rolling down the potential hill" (see Eq. (1.54)) towards the true vacuum. If the mode amplification is not large enough, the quantum fluctuations around the false vacuum will not be able to destabilize it, causing an extension of the inflationary period by a couple of efolds after $N_{\rm b} = N(\eta(T_{\rm b}))$, which could be in conflict with upper bounds from CMB measurements [56], or even an *eternal inflation scenario* [34], in which the transition towards the true vacuum does not complete at all. Consequently, we will therefore distinguish between these two alternative cases with the help of the maximal growth factor[34], i.e.,

$$\Gamma^{\rm max}_{\rm growth} \;=\; \frac{\sqrt{|m^2(\varphi=0,\,T=0)|}}{H} \quad \begin{cases} \geq 1: & \text{Exit from thermal inflation,} \\ \leq 1: & \text{Extended inflationary period.} \end{cases} \tag{1.154}$$

[34] This criterion is similar to the one in the case of bubble nucleation driven FOPT (cf. (1.140)).

Which scenario will be realised in the end, depends on the concrete model under investigation, or more precisely, the concrete shape of the model's constraint effective potential.

To conclude, a tachyonic phase transition *within a period of (thermal) inflation* induces the exponential amplification of scalar quantum fluctuation modes, which destabilise the now completely unstable false vacuum, and drive the Universe's transition towards the true vacuum through a phase separation mechanism called spinodal decomposition. We importantly note that from what we have learned from Sec. 1.2.2, the increase in the quantum field's variance sources scalar-induced curvature perturbations, which translate into the generation of a SGWB that can be computed with Eq. (1.91).[35]

Remark. Eventhough the dynamics of the above described tachyonic phase transition resemble the features of a continuous phase transition as described in Secs. 1.3.2, it is important to note that it does *not* correspond to a genuine continuous phase transition showing true criticality at T_{b}. In the latter case, the system stays in equilibirum throughout the whole process. This corresponds to following a FOPT line in a phase diagram up to a critical end point (CEP) where we find a continuous phase transition, at which the metastable and stable vacua would smoothly merge together. This is *not* the case during a tachyonic phase transition, where the metastable minimum disappears and becomes an inflection point, indicating the appearance of a *dynamical* instability and thus out-of-equilibirum processes. Note that only in the limiting case where a mean-field description of the system under consideration is exact, does the tachyonic phase transition correspond to a continuous phase transition at a true critical point.

[35]It is worth mentioning that the production of GWs in similar settings have been analysed in preceding studies, e.g., [57], where non-perturbative techniques such as holography were employed to study the real-time evolution of this thermodynamic process.

Chapter 2

BSM Physics: The Classically Conformal $U(1)_{\mathrm{B-L}}$ Model

Despite its tremendeous success in explaining the nature and interactions of the building blocks of the our Universe, the *Standard Model of Particle Physics (SM)* with the gauge group $SU(3)_{\mathrm{c}} \times SU(2)_{\mathrm{L}} \times U(1)_{\mathrm{Y}}$ cannot serve as the full picture due to a number of conflicting observations within this framework: the origin of the neutrino masses, the nature of dark matter and dark energy, the lack of a quantum description of Einstein's GR, the strong CP problem[1], and the hierarchy problem, among others. The latter relates to the puzzle of the origin of the Higgs masses' peculiar value, and the resulting question of potential new heavier physics awaiting us beyond the EW scale.

The CC-$\mathrm{B-L}$-model feautures the dynamical radiative generation of the Higgs mass, the generation of the neutrino masses via the Seesaw mechanism, and sterile neutrinos as dark matter candidates. The model does not only offer the geat opportunity to learn about cosmological phase transitions in BSM frameworks, but also features the possibility for cosmological FOPT, rendering the theory potentially probable through its SGWB production.

2.1 Set-Up

In this work, we want to study the interesting phenomenological consequences of the so-called *Classically Conformal* $U(1)_{\mathrm{B-L}}$ *SM extension* [59], which is defined through

[1]The strong CP problem referrs to the *issue* in quantum chromodynamics (QCD) where a CP-violating term would technically be allowed in the Lagrangian but does not manifest in nature through observations, leaving scientists with an apparent fine-tuning problem for the θ-or vacuum angle. It may be noted that this topic is especially present in recent discussion in which it is re-evaluated whether this poses an actual fine-tunig problem, or if it is based on past mistreatments in QCD-calculations. For more details, see [58].

the following Lagrangian,[2]

$$\mathcal{L} = \mathcal{L'}_{SM} - \frac{1}{4} Z'_{\mu\nu} Z'^{\mu\nu} + |D_\mu \Phi|^2 - V(H, \Phi)\,. \tag{2.1}$$

Here, $\mathcal{L'}_{SM}$ is the Lagrangian describing the interactions of the Standard Model particles with themselves and the Higgs, and $\mathcal{L'}_{SM}$ is the part that exhibits the coupling of the new complex scalar field Φ with the Higgs field H. The symmetry group underlying this theory is thus $SU(3)_\mathrm{c} \times SU(2)_\mathrm{L} \times U(1)_\mathrm{Y} \times U(1)_\mathrm{B-L}$, in which the global $(\mathrm{B}-\mathrm{L})$-symmetry has been promoted to a local gauge symmetry $U(1)_\mathrm{B-L}$. This BSM model comes with three new sterile neutrinos (that we will not consider any further), one new gauge boson Z' and the new complex scalar field Φ. Their dynamics are encoded in the corresponding terms in $\mathcal{L}$, namely

$$Z'_{\mu\nu} = \partial_\mu Z'_\nu - \partial_\nu Z'_\mu\,, \tag{2.2}$$

$$D_\mu \phi = \left(\partial_\mu + i 2 g_\mathrm{BL} Z'_\mu\right) \Phi\,, \tag{2.3}$$

$$V(H, \Phi) = \lambda_\mathrm{H} (H^\dagger H)^2 + \lambda_\mathrm{P} (H^\dagger H)(\Phi^\dagger \Phi) + \lambda_\phi (\Phi^\dagger \Phi)^2\,. \tag{2.4}$$

where $Z'_{\mu\nu}$ is the new gauge field, $\lambda_{\mathrm{H}\phi}$ is the bare *portal coupling* determining the interaction strength between H and Φ, λ_ϕ is the bare Φ-self-coupling, λ_H is the bare H-self-coupling, and g_BL is the new bare gauge coupling. The *constrained* finite-temperature quantum effective potential $V_\mathrm{eff}(\varphi, T)$ to one-loop order in standard pertubation theory is given by

$$V_\mathrm{eff}(\varphi, T) = V^{(0)}_\mathrm{eff}(\varphi) + V^{(1)}_\mathrm{eff}(\varphi, T) + V_\mathrm{daisy}(\varphi, T)\,, \tag{2.5}$$

where φ corresponds to the scalar field's zero-mode (see Eq. (1.127)), which we will also denote as the *background field*. The tree-level contribution to $V_\mathrm{eff}(\varphi, T)$,

$$V^{(0)}_\mathrm{eff}(\varphi) = \begin{cases} \frac{\lambda_\varphi}{4} \varphi^4\,, & T \geq T_\mathrm{QCD}\,, \\ \frac{\lambda_\varphi}{4} \varphi^4 - \frac{\lambda_\mathrm{P}}{4} v^2_\mathrm{QCD} \varphi^2\,, & T < T_\mathrm{QCD}\,, \end{cases} \tag{2.6}$$

receives an additional term $\propto {v_\mathrm{QCD}}^3$ from the coupling to the Higgs field after the QCD phase transition around $T \simeq 100$ MeV [61]. The one-loop contribution consists of a typical Coleman-Weinberg term (see Sec. 1.4) and a second part involving the thermal intergrals J_T (see Eq. 1.135), i.e.,

$$V^{(1)}_\mathrm{eff}(\varphi, T) \;=\; V_\mathrm{CW}(\varphi) + \frac{T^4}{2\pi^2} \sum_i k_i J_T\left(M_i^2(\varphi)\right)\,, \tag{2.7}$$

$$V_\mathrm{CW}(\varphi) = \sum_i \frac{n_i M_i^4(\varphi)}{64\pi^2} \left[\ln\left(\frac{M_i^2(\varphi)}{\mu^2(\varphi, T)}\right) - c_i\right]\,, \tag{2.8}$$

[2]Here, we omitted the contribution to the Lagrangian describing the sterile neutrinos as well as the Seesaw mechanism, since these parts are not relevant for the study conducted in this work.

[3]For our later study, we follow [60] and set $v_\mathrm{QCD} \sim 100$ MeV.

Particle	$m_i^2(\varphi)$	$\Pi_i(T)$	n_i	c_i
φ	$3\lambda_0\varphi^2$	$(g_{\mathrm{BL}}^2 + \lambda_0/3)T^2$	1	3/2
G	$\lambda_0\varphi^2$	$\Pi_\varphi(T)$	1	3/2
Z'	$4g_{\mathrm{BL}}\varphi^2$	$4g_{\mathrm{BL}}T^2$	3	5/6

Table 2.1: Ingredients of the (B − L) -SM extension.

in which n_i and $c_i = 5/6\,(3/2)$ are the number of degrees of freedom of the i-th particle species, and specific constants for bosonic (fermionic) fields, respectively.

Lastly, we add the *daisy resummation term* to resum a certain class of Feynman diagrams, and therefore treat artificial infrared (IR) ($k \to 0$) divergencies arising in perturbative calculations in finite-temperature field theories. It reads

$$V_{\mathrm{daisy}}(\varphi, T) \;=\; -\sum_i \frac{T}{12\pi}\left[\left(M_i^2(\varphi) + \Pi_i(T)\right)^{\frac{3}{2}} - \left(M_i^2(\varphi)\right)^{\frac{3}{2}}\right], \tag{2.9}$$

where $\Pi_i(T)$ is the so-called *thermal* or *Debye mass* of the i-th particle species (see Table 2.1). Note that the daisy resummation technique is rather an adhoc method and thus certainly not the most elegant way of dealing with IR divergencies. A modern and more systematic approach to tackle this problem in perturbative calculations is called the *High-temperature dimensional reduction (HTDR)* technique [62], with which one constructs lower-dimensional effective field theories (EFTs) through the scale hierachy between the zero- and the non-zero Matsubara modes at $T > 0$. This allows to systematically integrate out modes of different scales, which yields the common daisy ressumation technique at first order.

Note that we employ also the one-loop β-functions for the couplings present in the system (as calculated in [63]) to minimize the perturbative results' dependence on the chosen renormalization (RG) scale μ. As a systematic uncertainty, the latter can have a sizable impact on GW background predictions within such a setting as shown in [30]. Discrepancies between individual GW spectra predictions with varied μ signalise a larger residual RG scale dependence of the constraint quantum effective potential, indicating the need for higher loop-order corrections to obtain robust predictions.

The free model parameters g_{BL} and $m_{Z'}$ Our BSM model comes along with five parameters of unknown values: the scalar self-coupling λ_φ, the portal coupling λ_{P}, the new B − L gauge coupling g_{BL}, and the kinetic mixing $\tilde{g}$ between the gauge groups $U(1)_{\mathrm{B-L}}$ and $U(1)_{\mathrm{Y}}$. We employ the procedure from [60,64] to set our input parameter such that they become functions of only g_{BL} and $m_{Z'}$. We require λ_{P} and λ_φ to reproduce the EW scale by fixing them at the RG scale $\mu = m_{Z'}$, and demanding that they match experimentally determined values, such as the SM Higgs VEV. The SM couplings are obtained from the physical masses $m_{SM} = \{m_h, m_W, m_W, m_t\}$. By solving the one-loop β-functions [63] for the involved parameters, we may finally compute $V_{\mathrm{eff}}(\varphi, T)$.

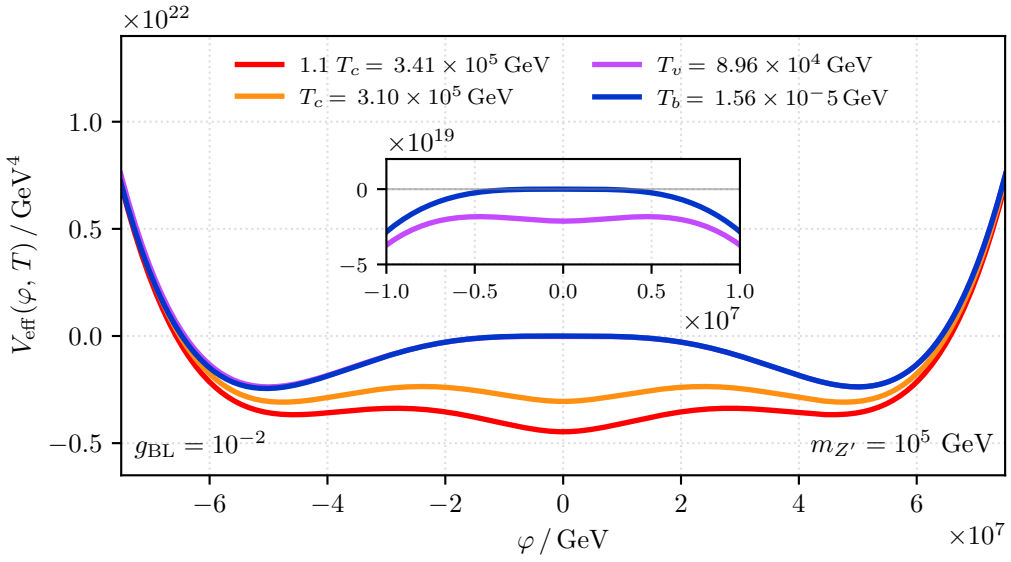

Figure 2.1: The constrained effective potential $V_{\text{eff}}(\varphi, T)$ at its different characteristic temperatures scales $T = \{T_{\text{c}}, T_{\text{v}}, T_{\text{b}}\}$.

2.2 Characteristic temperature scales

It is well known from preceding studies [60, 61] that due to its classical conformality, the B − L-model opens up the possibility towards supercooled cosmological phase transitions in the very early Universe. It even features a number of different scenarios, here referred to as *phase transition pathways*, which are realised in specific regions of the parameter space (g_{BL}, $m_{Z'}$). Hence, the dynamics of our model's phenomenology stretch across a wide range of time/energy scales (max. 10 orders of magnitude), which can be characterized by the following scale of temperatures:

- **Critical temperature T_{c}:** This is the temperature at which the constraint quantum effective potential effective potential develops a second local minimum at $\varphi_c \neq 0$, such that both minima become degenerate, i.e.,

$$V_{\text{eff}}(\varphi = 0, T_{\text{c}}) = V_{\text{eff}}(\varphi_c, T_{\text{c}})\,. \tag{2.10}$$

- **Inflation-onset temperature T_{v}:** During a supercooling period, the thermal potential barrier persists until very low temperatures such that the VEV remains trapped at the false vacuum for a long time. The vacuum (potential) energy contribution eventually starts to dominate the radiation energy contribution at

the temperature T_{v}, i.e.,

$$\rho(T) \;=\; \rho_{\mathrm{vac}}(T) + \rho_{\mathrm{rad}}(T) \;=\; \rho_{\mathrm{vac}}(T)\left(1 + \frac{\rho_{\mathrm{rad}}(T)}{\rho_{\mathrm{vac}}(T)}\right) \tag{2.11}$$

$$\approx \rho_{\mathrm{vac}}(T) \;=\; \text{const.}\,, \quad \text{for } T < T_{\mathrm{v}}\,. \tag{2.12}$$

Followingly, the Universe will be dominated by a constant energy density, causing the scale factor to grow exponentially and thus initiating a period of *thermal inflation*[4].

- **QCD phase transition temperature T_{QCD}:** At this temperature scale, one expects a QCD phase transition featuring quark condensation, which generates an additional term linearly proportional to the Higgs field (cf. Eq. (2.6)), which effectively counteracts and may eventually *"melt"* the thermal potential barrier.
- **Tachyonic temperature T_{b}[5]:** This is the temperature at which the QCD-induced term in Eq. (2.6) finally cancels the thermal barrier such that the curvature of V_{eff} at the origin vanishes, i.e.,

$$0 \;=\; m^2(\varphi = 0,\; T = T_{\mathrm{b}}) \;=\; \partial_{\varphi}^2 V_{\mathrm{eff}}(\varphi, T_{\mathrm{b}})|_{\varphi=0}\,. \tag{2.13}$$

The sign of the curvature mass at the *false vacuum* flips and becomes negative, such that our contraint quantum effective potential exhibits a *tachyonic instability*. Following the mean-field stability definitions in Sec. 1.3.3 and 1.3.4, this means that for $T \leq T_{\mathrm{b}}$ the *false vacuum* at $\varphi = 0$ is not metastable anymore but *completely unstable* with respect to small fluctuations around it. As described in Sec. 1.4.2, the negative curvature mass induces the exponential growth of fluctuation modes that destabilise the false vacuum, driving the phase transition of the VEV towards the true vacuum.

2.3 Possible Phase Transitions Pathways

The ordering of the relevant temperature scales in our model is: $0 < T_{\mathrm{b}} < T_{\mathrm{v}} < T_{\mathrm{c}}$. Thus, the different phase transition pathways can be distinguished from another by the scale of the percolation temperature T_{p} with regards to the phase transition in the φ-direction (see also Sec. 2.3):

I **First-order $\mathrm{B-L}$ phase transition ($T_{\mathrm{QCD}} < T_{\mathrm{p}}$):**
If percolation completes successfully before the QCD scale, i.e. $T_{\mathrm{p}} > T_{\mathrm{QCD}}$, we find a $\mathrm{B-L}$-FOPT through which the SM Higgs mass term is generated by the true vacuum of the new scalar field φ. If $T_{\mathrm{EW}} > T_{\mathrm{p}} > T_{\mathrm{QCD}}$, where $T_{\mathrm{EW}} \simeq 100\,\mathrm{GeV}$ is the EW scale in the SM, we find a slightly delayed continuous EW phase transition.

[4]Note that such thermal inflation period is distinct from the cosmic inflation period right after the big bang.

[5]It is also referred to as T_{roll} in the related publication [60].

II **Combined EW-QCD phase transition:**
In the scenario where $T_\mathrm{p} < T_\mathrm{QCD}$, the QCD phase transition will happen *before* the percolation of the $\mathrm{B}-\mathrm{L}$-FOPT completes successfully. The quark-condensation (especially $\langle t\bar{t}\rangle$) will generate an additional term linear in h in the constraint effective potential of the $\mathrm{B}-\mathrm{L}$-model (cf. Eq. (2.6)), which counteracts the thermal potential barrier. Moreover, the QCD phase transition happens prior to the EW phase transition (in contrast to the SM), and triggers EWSB by generating an intermediate Higgs VEV, $v_{h,\mathrm{QCD}} \sim 100\,\mathrm{GeV}$. Two further subcases can now be identified w.r.t. the $\mathrm{B}-\mathrm{L}$ phase transition, depending on how much more time the percolation will take:

IIa If $T_\mathrm{QCD} > T_\mathrm{p} > T_\mathrm{b}$, we have $\mathrm{B}-\mathrm{L}$ phase transition of first order completing via the bubble nucleation mechanism.

IIb If $T_\mathrm{QCD} \gg T_\mathrm{p}$, $T_\mathrm{p} \to T_\mathrm{b}$, i.e., the percolation temperature lies well below the QCD-scale and approaches the temperature at which the thermal potential barrier melts. A *dynamical* tachyonic instability emerges, rendering the $\mathrm{B}-\mathrm{L}$ phase transition still a FOPT, which can now only primarily complete via spinodal decomposition (see Sec. 1.4.2).

In both cases, subsequent reheating periods will pump back the energy from the new scalar sector to the SM sector via decays to SM particles.

In this work, we will study the linear regime or, equivalently, the initial quantum phase of the phase transition dynamics of the last case (IIb), and assess its potential for a sizable SGWB production.

2.3.1 QCD-sourced Tachyonic $\mathrm{B}-\mathrm{L}$ Phase Transition

The results of a preceded study [60] demonstrated that our BSM model exhibits a region in the parameters space where a tachyonic instability in the new sectors contrained quantum effective potential emerges (see Sec. 2.3, Case (IIb)). The $\mathrm{B}-\mathrm{L}$ phase transition towards the true vacuum state begins with an exponential amplification of fluctuation modes, which destabilise the unstable false vacuum, and concludes with the (dominant) "classical rolling" dynamics of the background field φ. The driving phase separating mechanism is therefore spinodal decomposition instead of bubble nucleation.

The constrained *tachyonic parameter subspace* (see Fig. 2.3.1) spans over the area

$$A_\mathrm{tachyonic} = m_{Z'} \times g_\mathrm{BL} \equiv [5\times10^4\ \mathrm{GeV},\, 5\times10^7\ \mathrm{GeV}] \times [10^{-4},\, 2\times10^{-1}]\,. \tag{2.14}$$

The ultimate goal of this work is now to analyse the phase transition dynamics by studying the evolution of the fluctuation modes and the field's variance via the methodology developed in Sec. 1.4.2. For small background field values φ, the mode amplitude growth rate (cf. Eq. (1.154)) has been estimated as

$$\Gamma^\mathrm{BL}_\mathrm{growth}(T) \;=\; \frac{\sqrt{|m^2(\varphi=0,T)|}}{H} \;\overset{T\to0}{\longrightarrow}\; \frac{\sqrt{|\Delta m^2_{\varphi,\mathrm{QCD}}|}}{H}\,, \tag{2.15}$$

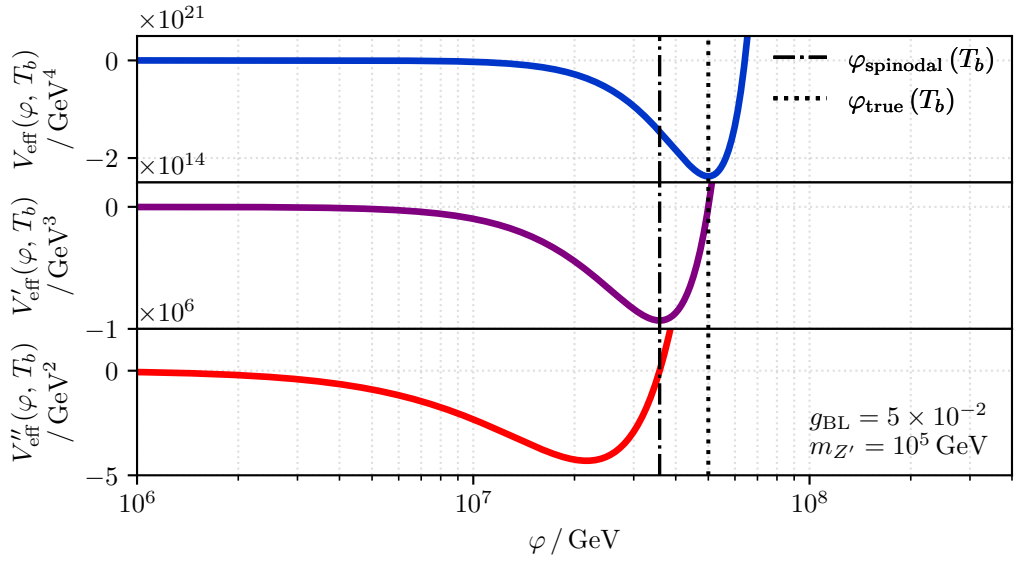

Figure 2.2: Constraint effective potential and its derivatives for $g_{\mathrm{BL}} = 5 \times 10^{-2}$ and $m_{Z'} = 10^5\,\mathrm{GeV}$, evaluated at $T = T_{\mathrm{b}}$, where we highlighted the tachyonic field region $|\varphi| \leq \varphi_{\mathrm{spinodal}}$. Fluctuation modes will experience exponential amplification until the background field reaches the spinodal point during its evolution.

which also corresponds to the quantity plotted in Fig. 2.3.1.

Spectral GW Density from Tachyonic Instability & Redshift Factor

Following our discussions from Secs. 1.2.2 and 1.4.2, we finally want to investigate the possible SGWB signatures of the tachyonic B − L phase transitions within our model. For this purpose, we will use the expression for the redshifted spectral GW density given in Eq. (1.91), in which we will employ the dimensionless curvature power spectrum derived in Eqs. (1.89) and (1.90). Eventhough the parameter subspace under consideration includes models featuring a subsequent short reheating period — mostly the points close to the decay constraint line in Fig. 2.3.1 — we will henceforth neglect this fact for practicality reasons and leave a more careful treatment for future work. More precisely, we will assume instant reheating from T_{cl}, i.e. the temperature at which classical rolling starts to dominate our background field's dynamics (see Eq. (1.25)), to T_{v}. This allows us to identify

$$T_{\mathrm{RH}} = T_{\mathrm{v}}\,, \quad a_{\mathrm{RH}}\, k_{p,\mathrm{RH}} = k\,, \quad a_{\mathrm{RH}} = e^{N_{\mathrm{cl}}}\,, \tag{2.16}$$

$$\frac{a_{\mathrm{RH}}}{a_0} = \left(\frac{T_0}{T_{\mathrm{RH}}}\right)\left(\frac{g_{\star,s}(T_0)}{g_{\star,s}(T_{\mathrm{RH}})}\right) = \left(\frac{T_0}{T_{\mathrm{v}}}\right)\left(\frac{g_{\star,s}(T_0)}{g_{\star,s}(T_{\mathrm{v}})}\right)^{\frac{1}{3}}\,, \tag{2.17}$$

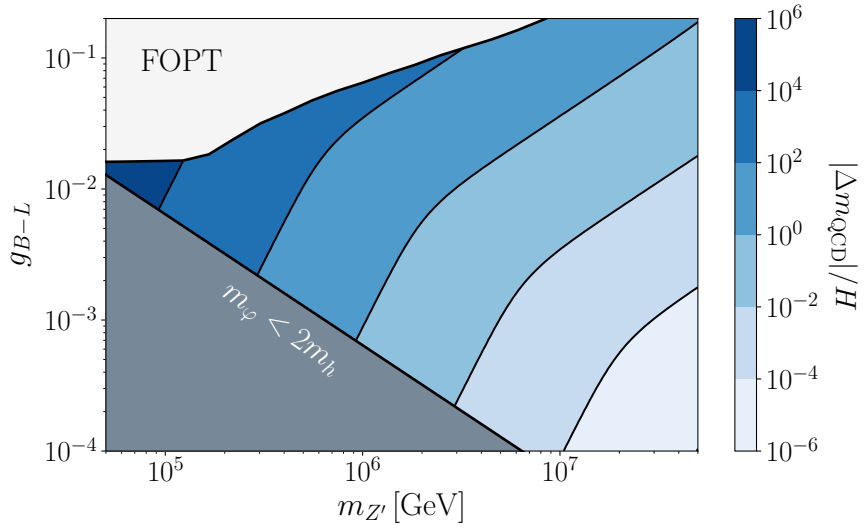

Figure 2.3: The tachyonic B − L parameter space [60], here filled in shades blue. The latter depicts the maximal mode growth factor given by Eq. (2.15). Two exlusion regions are constraining the subspace. For larger gauge couplings and gauge boson masses (*upper left, white shaded region*), the B − L phase transition completes via bubble nucleation before the tachyonic instability occurs. For smaller gauge couplings and gauge boson masses, the scalar field mass is too low to decay to the SM Higgs boson, preventing a necessary and successful reheating period after the B − L phase transition (*lower left, gray shaded region*) We will henceforth include both of these constrained regions in our calculations. Figure adopted from [60].

where $k_{p,\mathrm{RH}}$ is the *physical* wavenumber at the reheating temperature, and $N_{\mathrm{cl}} = N(\eta(T_{\mathrm{cl}}))$ is the efold number at which $\varphi \simeq \varphi_{\mathrm{cl}}$. Note that we have set $a(T_{\mathrm{v}}) = a(T(N = 0)) \equiv 1$, i.e., we have normalised the scale factor at the beginning of the inflationary period to 1. Finally, we can express the present-day (redshifted) physical frequency $f_{p,0}$ or wavenumber $k_{p,0}$ as

$$2\pi f_{p,0} = k_{p,0} = \frac{k_{p,\mathrm{RH}}\, a_{\mathrm{RH}}}{a_0} = \frac{k}{a_{\mathrm{RH}}} \left(\frac{T_0}{T_{\mathrm{RH}}}\right) \left(\frac{g_{\star,s}(T_0)}{g_{\star,s}(T_{\mathrm{RH}})}\right)^{\frac{1}{3}} \tag{2.18}$$

$$= k\; e^{-N_{\mathrm{cl}}} \left(\frac{T_0}{T_{\mathrm{v}}}\right) \left(\frac{g_{\star,s}(T_0)}{g_{\star,s}(T_{\mathrm{v}})}\right)^{\frac{1}{3}}$$

$$\Leftrightarrow \quad f_{p,0}(k) = \frac{k}{2\pi}\; e^{-N_{\mathrm{cl}}} \left(\frac{T_0}{T_{\mathrm{v}}}\right) \left(\frac{g_{\star,s}(T_0)}{g_{\star,s}(T_{\mathrm{v}})}\right)^{\frac{1}{3}} \tag{2.19}$$

$$\Leftrightarrow \quad f_{p,0}(k) = k\ e^{-N_{\mathrm{cl}}} \left(\frac{T_0}{T_{\mathrm{v}}}\right) \left(\frac{g_{\star,s}(T_0)}{g_{\star,s}(T_{\mathrm{v}})}\right)^{\frac{1}{3}} \times 2.418 \times 10^{23}\, \frac{\mathrm{Hz}}{\mathrm{GeV}}\,. \tag{2.20}$$

$$\tag{2.21}$$

where k is the comoving wavenumber (of the associated simulated k-mode) (in GeV), and the temperature of the SM plasma today corresponds to the CMB temperature, i.e., $T_0 = T_{\mathrm{CMB}} = 2.725\ \mathrm{K} \approx 2.725 \times 8.62 \times 10^{-14}\ \mathrm{GeV}$.

Chapter 3

Numerical Implementation

In this section, we will describe the numerical methodology that we developed to obtain the results listed in Chapter 4.

The goal of this work was to develop a `Python` code to solve the Amplitude-Mukhanov-Sasaki equations (1.78) including the curvature mass $m^2(\varphi(\eta), T(\eta))$ derived from the $\mathrm{B}-\mathrm{L}$ one-loop constraint quantum effective potential $V_{\mathrm{eff}}(\varphi(\eta), T(\eta))$ (see Eq. (2.4)) to study the nature of the linear regime of the tachyonic transition in our model. The obtained numerical solutions shall then be used to compute the resulting scalar-induced curvature power spectrum in Eq. (1.90) as well as the corresponding gravitational wave spectrum from Eq. (1.91).

In the following, we will give a detailed account of the variety of numerical challenges one faces with these kind of physical systems, and discuss with which solutions these have been (mostly) overcome.

3.1 Mode Amplitude & Variance Evolution

At the heart of the analysis conducted in this work lies the computational infrastructure for the simulation of the *comoving* k-modes' evolution from the onset of the inflationary period at T_{v} until the end of the linear or quantum regime at T_{cl} (see Sec. 2.3.1) with the general methodology described in Sec. 1.4.2. Since inflationary time scales are commonly best described by efolds N (see Eqs. (1.26) and (1.28)), we will define the start and end of the time period during which the physical process under investigation takes place via N_{min} to $N_{\mathrm{abort}}^{\mathrm{phys}}$, where

$$\mathtt{N} = \left[N(T_{\mathrm{v}}),\, N_{\mathrm{abort}}^{\mathrm{phys}}\right] , \tag{3.1}$$

$$N_{\mathrm{min}} \equiv N(T_{\mathrm{v}}) = 0\,, \quad N_{\mathrm{abort}}^{\mathrm{phys}} \equiv N(T_{\mathrm{cl}}) = N(T(\eta_{\mathrm{cl}})) = N_{\mathrm{cl}}\,, \tag{3.2}$$

respectively. We are free to set the scale factor a as we want, such that we choose to normalise it to unity at the beginning of the inflationary period, i.e. $a(N_{\mathrm{min}}) \equiv 1$. Followingly, this translates to an initial conformal time $\eta_{\mathrm{min}} \equiv \eta(N_{\mathrm{min}}) = -1/\mathcal{H}$.

Since we are interested in the evolution of the k-modes' amplitudes that generate curvature pertubation after the inflationary period, i.e., the amplitudes of all modes leaving the Hubble horizon until $T_{\rm cl} = T(\eta_{\rm cl})$, we need to solve the following differential equation (DEQ)

$$0 = A_k''(\eta) - \frac{1}{4\,A_k^3(\eta)} + \omega_k^2(\eta)\; A_k(\eta)\,, \tag{3.3}$$

$$\omega_k^2(\eta) = k^2 - \frac{2}{\eta^2} + a^2(\eta)\cdot m^2(\varphi(\eta), T(\eta)) \;= \Omega_k^2(\eta) - 2\left(a(\eta)\mathcal{H}(\eta)\right)^2\,. \tag{3.4}$$

for the modes with wavenumber k lying in the *minimum wavenumber interval* $\mathtt{k}$,

$$k \in \mathtt{k} \equiv a(\mathtt{N})\mathcal{H}e^{\mathtt{N}} = [a(T_{\rm v})\mathcal{H},\, a(T_{\rm cl})\mathcal{H}] \overset{(3.1)}{=} [\mathcal{H},\, \mathcal{H}\,\exp(N_{\rm cl})]\,. \tag{3.5}$$

Obviously, necessary wavenumbers span over

$$\log_{10}\left(\exp(N_{\rm cl})\right) = \log_{10}(e)\times N_{\rm cl} \approx 0.43\times N_{\rm cl} \tag{3.6}$$

orders of magnitude. For example, in the common case of $N_{\rm cl} \simeq 25$, we will have to resolve the evolution of k-modes whose wavenumbers span across approximately 11 orders of magnitude. Recall that the sign of the frequency ω_k^2 in Eq. (3.3) decides if the specific k-mode's evolution follows the typical behaviour of the sub- or super-horizon limit, i.e., if it the mode is either (rapidly) oscillating with almost constant amplitude, or if the oscillation decays and the amplitude freezes out, respectively. At the beginning of the inflationary period at $N = N_{\rm min}$, all k-modes are in the Hubble horizon, i.e., $k \geq a(N_{\rm min})\mathcal{H} = \mathcal{H}$, and can thus be expressed via the BD vacuum solution in Eq. (1.68). Then over the simulation time, the individual k-modes will progressively exit the Hubble horizon at their *horizon-crossing conformal time* $\eta_{\rm cross}$ (see Eq. (1.71)) — first the IR- (long wavelength), and then the UV- (short wavelength) modes due to the shrinking Hubble horizon during inflation. This means that our numerical DEQ solver must be capable of resolving both these widely different solution behaviours *at the same time step*. This leads us directly to the numerical challenges one encounters when dealing with such kind of physical systems.

3.1.1 Numerical Challenges

The development of the DEQ solver was challenged by two main properties of the system that we want to study:

I **Dependency of the DEQ on the background field evolution** Formally, we need to solve the k-mode amplitude evolution that is coupled to the evolution of the background field φ through the curvature mass in the DEQ frequency (cf. Eq. (3.3)). However, we find ourselves in a special physical set-up, namely in a supercooled Universe experiencing an additional thermal inflation period before

the onset of a tachyonic phase transition as described in Sec. 2.3.1. In the context of studying this scenario until the end of its linear or quantum regime, we may use the approximative treatment of the background field evolution as elaborated in Sec. 1.4.2. It assumes φ to be trapped at the false vacuum at $\varphi = 0$ for $N < N_\mathrm{b}$, such that the individual k-mode evolutions become decoupled from one another until this point. The concrete numerical implementation of the *linear regime background field treatment* will be further explained in Sec. 3.1.3.

II **Simulating a large number of scales simultaneously** As mentioned previously, we need to simulate the amplitude evolution of k-modes, whose wavenumbers span over roughly over 10 orders of magnitude, over a time span of N_cl efolds, during which they simply evolve drastically differently on different time scales. Differently stated, our solver has to handle the rapid oscillations of the UV-modes as well as the freeze-out of the IR-modes *simultaneously*. Such numerical problems are referred to as *stiff problems* in the literature, and the associated DEQs as *stiff DEQs* [65, 66]. In such cases, commonly used *explicit solver algorithms* fail to perform well or even provide a stable result at all. Since the next evolution step is only computed from the past step's results, it requires the algorithm to subsequently decrease the next time in order to preserve stability for the desired accuracy. On the other hand, *implicit solver algorithms* need the past and (guessed) future information to evolve the DEQ to the next time step, which is computationally more expensive per step, but much more stable and therefore extremely well suited for stiff systems. Thus, in our case, we will make use of the implicit `Radau` solver method, i.e., an implicit Runge-Kutta method, for the `solve_ivp` solver from the Python package `SciPy` [67].

Eventhough the latter already helps to tremendously reduce the computation time of a single simulation (from hours/days to minutes/hours), a poor choice of one of the key parameters impacting our simulation results can offset the time advantage we had gained by using a suitable solver method. More precisely, when designing the code infrastructure, it is important to ask the following questions:

Q1 Starting the simulation at at the beginning of the inflationary period at $N_\mathrm{min} = N(\eta_\mathrm{min})$ means simulating heavily oscillating sub-horizon k-modes for a very long time, which is computationally expensive. Is this really necessary to obtain the correct result at the end of the linear regime, or can we start our simulation at a later point in time before the tachyonic instability appears without losing importnt physical information?

Q2 What is the optimal set of parameters to define our simulation set-up, and what are their optimal values? Especially the choice of the number and interval of simulated wavenumbers need special attention. The minimum wavenumber interval in Eq. (3.5) spans over a large number of scales, with the physical maximum corresponding to $k_\mathrm{max} = k_\mathrm{cl} = a(T_\mathrm{c})\mathcal{H}$. What is the optimal number of k-modes to be simulated, and can we choose a smaller and more convenient value for k_max without (largely) impacting the end result?

In order to answer the above questions and thus to test our simulation code base properly, we first analysed the typical behaviour of the DEQ frequency of the $\omega_k^2(N(\eta))$ from Eq. (3.3) as a function of k to obtain a first feeling for the important parts of the evolution. Later on, we tested our developed code in order to reproduce the variance results from [68], through which we were able to identify the optimal simulation parameter set.

3.1.2 Preliminary Study for Code Optimisation

Finding appropriate Inital Conditions To find an answer for **Q1**, we need to check for how long the individual k-modes remain in the sub-horizon regime. For this purpose, we calculated the frequency evolution normalised to the frequency at the beginning of inflation, evaluated with the curvature mass at the false vacuum, i.e., $\omega_k^2\left(m^2(0,T(N))\right)$. The result is depicted in Fig. 3.1 for the parameter point set $g_{\rm BL} = 10^{-2}$ and $m_{Z'} = 5\times10^6\,\text{GeV}$. We can see that *all* modes maintain their oscillatory behaviour until (minimum) $N = 20$ in this case, and, in fact, in most cases. This means they have $\omega_k^2(N)\,/\,\omega_{k,0}^2 \geq 1$ for $N \in [0,20]$. The efold scale at which the IR-modes start to deviate from the oscillatory behaviour is naturally given by the efold number associated to the temperature at which the thermal potential barrier melts $N_{\rm b} = N(T_{\rm b}) = N(T(\eta_{\rm b}))$, since this is the time where the curvature mass becomes negative and starts decreasing the frequency ω_k^2. We will denote the wavenumber associated to $N_{\rm b}$ as the tachyonic wavenumber

$$k_{\rm b} \equiv \mathcal{H}\exp(N_{\rm b})\,. \tag{3.7}$$

Note that the very large UV-modes with $k \gg k_{\rm b}$ will remain oscillatory until the end of the simulation, when considering the expected duration of the linear regime being $N_{\rm cl} \in [20,35]$. Moreover, we observe that the IR-modes with $k < k_{\rm b}$ show a small amplification in their frequency (spike-like structure in Fig. 3.1) due to the drop in the evolution of the number of entropy dofs roughly between $N = 15$ and $N = 25$. To see how this explicitly impacts the frequency through the temperature-dependence of the curvature mass, we can calculate for $N < N_{\rm b}$

$$m^2(\phi(N),T(N)) \;\approx\; m^2(0,T(N)) \tag{3.8}$$

$$\propto g_{\rm BL}^2\,T^2(N) \;=\; g_{\rm BL}^2\left(\frac{g_{\star,i}}{g_\star(N)}\right)^{\frac{2}{3}} T_v^2\,e^{-2N}\,, \tag{3.9}$$

$$\Rightarrow a^2(N)\cdot m^2(\phi(N),T(N)) \;\approx\; g_{\rm BL}^2\left(\frac{g_{\star,i}}{g_\star(N)}\right)^{\frac{2}{3}} T_{\rm v}^2\,. \tag{3.10}$$

Since $g_\star(T(N))$ is a decreasing function in temperature and thus time, we expect the oscillatory frequency ω_k^2 of modes with $k^2 \sim \mathcal{O}\left(a^2\,m^2(0,T(N))\right)$ to increase by roughly an order of magnitude before the effective mass m^2 becomes negative around $N_{\rm b}$. The step-function-like nature of $g_\star(T(N))$ reflects in the non-smooth increase of ω_k^2 for $k < k_{\rm b}$.

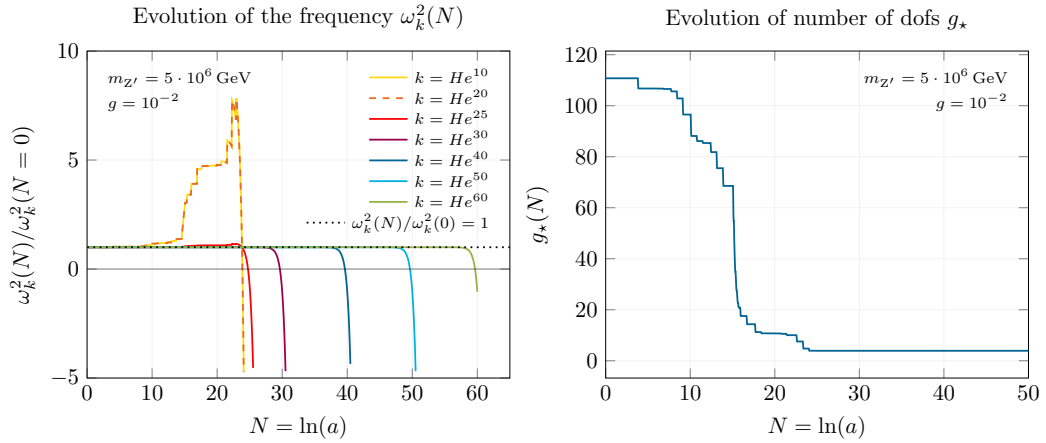

Figure 3.1: General structure of the frequencies' evolutions ω_k^2 shown explicitly at the benchmark parameter set $g_{\rm BL} = 10^{-2}$ and $m_{Z'} = 5 \times 10^6\,\text{GeV}$ (*left*). All modes remain oscillatory until shortly before the curvature mass flips it sign at $N_{\rm b}$. The frequencies of smaller k-modes are sensitive to the change of the entropy degrees of freedom $g_\star(T(N))$ (*right*) as the temperature cools down during the inflationary period.

We may also shortly study what happens if we vary the model parameters $g_{\rm BL}$ and $m_{Z'}$, which is demonstrated in Fig. 3.2. An increase in $g_{\rm BL}$ and a decrease in $m_{Z'}$ cause a sooner departure from the oscillatory behaviour. Note however that even under their variation, (almost) all modes remain in the sub-horizon regime roughly until $N = 20$.

From this analysis, we may conclude that the BD vacuum remains an appropriate initial condition for *all* k-modes well after the beginning of the inflationary period. Even the small amplification of the IR-modes due to the drop in the entropy dofs is not worrysome with regards to the variance evolution, since the latter is dominated by its thermal contribution until shortly before $N_{\rm b}$ (see Sec. 4.1).

We therefore employ the BD vacuum from Eq. (1.68) as standard initial condition for all simulations, and choose the simulation starting conformal time $\eta_{\rm start}$ or equivalently efold $N_{\rm start}$ by the following rule:

$$N_{\rm start} = \begin{cases} 20\,, & N_{\rm b} \geq 20\,, \\ \lfloor N_{\rm b} - 2 \rfloor\,, & N_{\rm b} < 20\,. \end{cases} \tag{3.11}$$

The maximal time period our simulations will capture will be set by $N_{\rm end} = 50$ for all parameter points, which is, one the one hand, due to practicality reasons, and on the other hand, also physically motivated due to inflation constraints from the CMB (see discussion in [30], Sec. II).

Lastly, the k-mode evolution for the time period from the start of inflation until the start of our simulation, i.e., for $N \in [0, N_{\rm start})$, will be also calculated using the analytical BD vacuum solution.

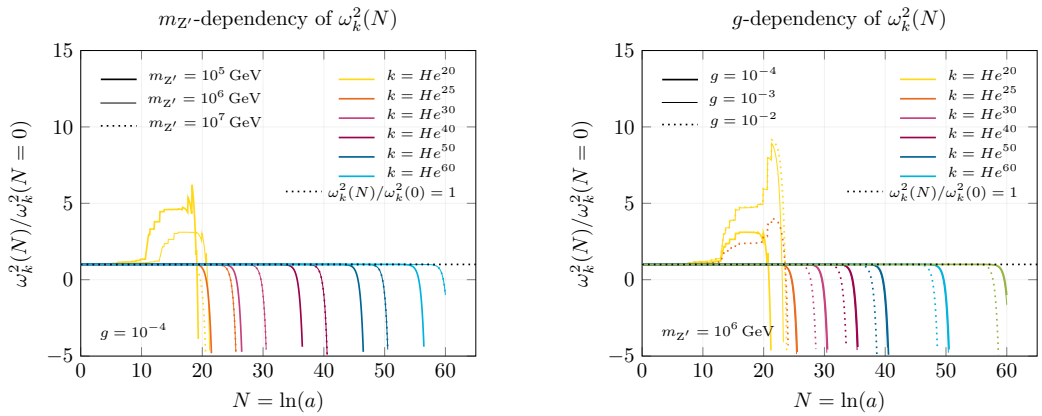

Figure 3.2: Effect on the frequencies' evolution under variation of the model parameters $m_{Z'}$ and $g = g_{\mathrm{BL}}$.

Finding an appropriate set of Simulation Parameters After an initial code development and testing phase, including the successful reproduction of a benchmark variance evolution from [30] (see Fig. 3.3), we identified the following key parameters to determine the quality of our simulation:

- $\boldsymbol{N_{\mathrm{start}}}$: Efold number at which simulation of the k-modes' evolutions is started, determined by the rule in Eq. (3.11).
- $\boldsymbol{N_{\mathrm{end}}}$: Efold number that defines the maximum simulation time. Due to the divergent nature of the variance in our set-up, this value is never reached and serves as an upper limit.
- $\boldsymbol{N_{\mathrm{mid}}}$: Efold number that defines the largest wavenumber $k_{\mathrm{mid}} \equiv \mathcal{H}\exp(N_{\mathrm{mid}})$ and thus the largest UV-mode that is being numerically evolved until the end of the simulation. In order to be able to reproduce the characteristic evolution of the scalar field's variance in the presence of a tachyonic instability in the constraint quantum effective potential, it is neccessary to have tachyonically amplified k-mode amplitudes included. Only the latter are responsible for its steep increase after N_{b} (cf. Fig. 4.1). It is therefore completely sufficient to only simulate k-modes with wavenumbers that lie in the interval

$$k \in \mathtt{k} \equiv [\mathcal{H}, k_{\mathrm{cl}}]\,, \tag{3.12}$$

$$k_{\mathrm{cl}} = \mathcal{H}\exp(N_{\mathrm{cl}}) = \mathcal{H}\exp(N(\eta_{\mathrm{cl}}))\,, \tag{3.13}$$

We will therefore simulate k-modes with wavenumber lying in the interval

$$\mathtt{k}_{\mathrm{sim}} \equiv [\mathcal{H}, k_{\mathrm{mid}}] = [\mathcal{H}, \mathcal{H}\exp(N_{\mathrm{mid}})]\,, \tag{3.14}$$

$$N_{\mathrm{mid}} = \begin{cases} 40\,, & N_{\mathrm{b}} \geq 20\,, \\ N_{\mathrm{start}} + 10\,, & N_{\mathrm{b}} < 20\,. \end{cases} \tag{3.15}$$

- |k|: Total number of k-modes being numerically evolved during the simulation. Several tests have revealed that |k|= 500 seems to be sufficient to obtain robust results. To further improve the accuracy of the variance calculation, which is a discrete integral over all super-horizon k-modes, we will use |k|= 1000 as the default value.
- `is_k_analytic` (*optional*): Boolean variable to decide whether or not UV-modes with $k \geq k_{\mathrm{mid}}$ should be computed analytically via the BD vacuum solution and added to the total variance at each evolution step.
  The initial version of the code featured the option to include an analytic background term for the variance calculation to account for the "missing" oscillatory k-modes with $k > k_{\mathrm{mid}}$ especially in the thermal variance sum. Later, we found that its inclusion is irrelevant for the end result due to the above explained reasons, which is why it has been disabled for all simulations.
- N_{max} (*optional*): Efold number that defines the largest wavenumber and thus the highest UV-mode contributing to the analytic background term for the variance. This has also become irrelevant since the analytic background itself has become irrelevant for our computations.

The relationship between these key parameters during the simulation is also illlustrated in Fig. 3.1.2.

N_{min}	N_{start}	N_{mid}	N_{end}	|k|	`is_k_analytic`	N_{max}
0	20 if $N_{\mathrm{b}} \geq 20$, else $N_{\mathrm{b}} - 2$	40 if $N_{\mathrm{b}} \geq 20$, else $N_{\mathrm{start}} + 10$	50	1000	`False`	60

Table 3.1: Fixed values for the key simulation parameters used for the simulations which have been performed to obtain the results presented in Sec. 4.

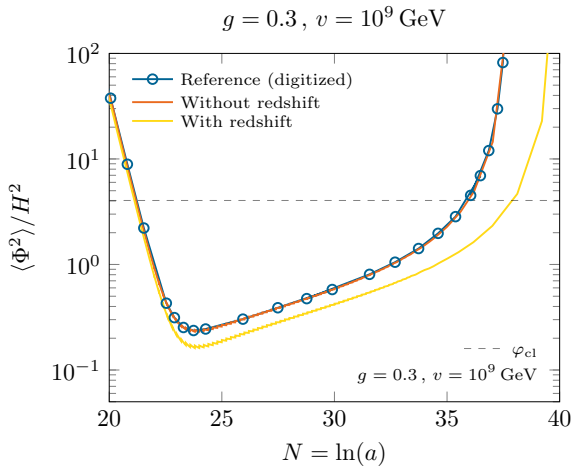

Figure 3.3: Reproduction of Fig. (3) from [30] with our k-mode amplitude evolution solver. The authors studied a similar mechanism to generate scalar-induced curvature pertubations from inflationary periods in a supercooled Universe. The reference curve (blue circles) matches our numerical result (orange). Due to an incorrect redshift factor in their Bose-Einstein distribution, the correct result for this benchmark point should however corresponds to the yellow curve.

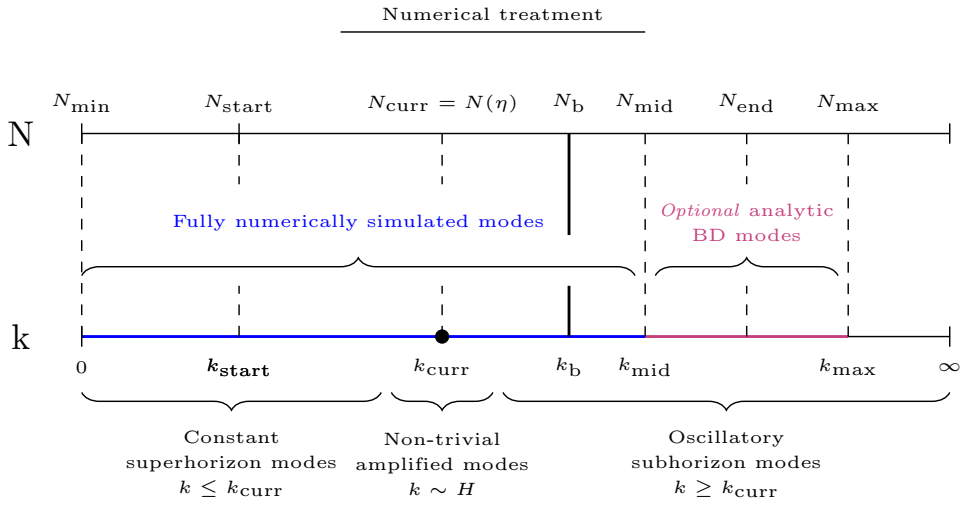

Figure 3.4: Overview of the evolution of the simulated comoving k-modes. Here, $k_{\rm curr} = a(\eta_{\rm curr})\mathcal{H}$ denotes the current horizon-exit mode at the current conformal time step $\eta_{\rm curr}$. As described in Sec. 1.2.1, a k-mode's evolution will depend on the value of their wavenumber relative to $k_{\rm curr}$.

3.1.3 Step-by-Step: How to Solve the Amplitude evolution

Let us now summarize the concrete computational tasks during each conformal time step of the implemented k-mode amplitude evolution solver:

Step I With the numerical solution of the previous conformal time step, calculate the current value of the variance $\langle\Phi^2\rangle(\eta_{\mathrm{curr}})$ as well as the approximate current background field value $\varphi(\eta_{\mathrm{curr}}) \equiv \sqrt{\langle\Phi^2\rangle(\eta_{\mathrm{curr}})}$;

Step II Check the sign of the current curvature mass at the false vacuum $m^2(0, T(\eta_{\mathrm{curr}}))$:

- If $m^2(0, T(\eta_{\mathrm{curr}})) \geq 0$: The thermal barrier still exists, and thus the background field still sits at the false vacuum at $\varphi = 0$. We thus may continue using the curvature mass at false vacuum, i.e. $m^2(0, T(\eta_{\mathrm{curr}}))$.
- If $m^2(0, T(\eta_{\mathrm{curr}})) < 0$, the tachyonic instability has appeared such that the false vacuum has become unstable and will be destabilised by the fluctuations. We therefore need to start using the curvature mass at the approximate background field value $m^2(\varphi(\eta_{\mathrm{curr}}), T(\eta_{\mathrm{curr}}))$. From this moment on, our modes' evolutions become coupled via the inclusion of the variance in their computation.

Step III Evolve each k-mode by a discrete conformal time step (automatically and adaptively handled by the `solve_ivp` solver).

Step IV Check if the variance has reached the maximal cut-off value:

- If $\langle\Phi^2\rangle(\eta_{\mathrm{curr}}) \geq \langle\Phi^2\rangle_{\mathrm{max}}$: The variance shows signs of diverging behaviour, i.e. the k-mode amplitudes are being amplified, such that we have encountered a *slow-roll exit scenario*. The simulation is therefore terminated in a controlled way at this point.
- $\langle\Phi^2\rangle(\eta_{\mathrm{curr}}) < \langle\Phi^2\rangle_{\mathrm{max}}$: The variance has not reached the maximum cut-off value yet, such that the simulation will be continued with the next conformal time step.
  $\rightarrow$ In the case that the simulation is never terminated until the fixed maximal simulation length at $N_{\mathrm{end}} = 50$, we have encountered an *extended inflationary scenario*.

Step V At the end of each simulation, flag the specific model parameter set with the boolean variable `is_terminated` to later distinguish the interesting *slow-roll exit scenarios* from the *extended inflationary scenarios*, in which unphysically large curvature pertubations are produced (see Eq. (1.154)).

Since we are only interested in the scalar field's evolution until the end of the linear regime, i.e. where $\varphi(\eta_{\mathrm{curr}}) \equiv \varphi_{\mathrm{cl}}(\eta_{\mathrm{curr}})$, we need to further differentiate between two principal evolution cases *after* each simulation (see Fig. 3.5):

- **Classical limit already reached at $T_\mathrm{b} = T(\eta_b)$:** The approximate background field value has already reached the end of the linear regime at the moment where the tachyonic instability first occurs. For later usage, the obtained simulation data is therefore truncated at $\eta_\mathrm{cl} \equiv \eta_b$.
- **Classical limit reached only later at $T_\mathrm{cl} < T_\mathrm{b}(\eta_b)$:** The end of the linear regime has not been reached yet at the appearance of the tachyonic instability, such that the mode evolution continues until $\varphi(\eta_\mathrm{curr}) \equiv \varphi_\mathrm{cl}(\eta_\mathrm{curr}) \equiv \eta_\mathrm{cl}$. In this case, the mode amplitudes experience additional efolds $\Delta N = N_\mathrm{cl} - N_\mathrm{b}$ of tachyonic amplification, resulting in an enhancement of the curvature perturbation production. Here, the obtained simulation data is truncated at η_{cl}.

  In the following, we will denote the temperature- or, equivalently, conformal time-dependent curve

$$\varphi_\mathrm{cl}(\eta) \equiv \varphi_\mathrm{cl}(T(\eta)) \quad \text{for} \quad T \in [0, T_\mathrm{b}] \tag{3.16}$$

  obtained by solving Eq. (1.25) as *the classicality line*.

Note that the simulation data in the cases of the *extended inflationary scenarios* will be left untruncated, having a maximal conformal time of the evolution corresponding to $\eta_\mathrm{end} = \eta(N_\mathrm{end} = 50)$.

3.2 Dimensionless Curvature Power Spectrum & GW Energy Density Spectrum

For the computation of the dimensionless curvature power spectrum at the time where the linear or quantum regime ends (see Eq. (1.90)), we will use the truncated versions of the k-mode amplitude evolutions, whose truncation process has been described in Sec. 3.1.3. Note that we will only compute the curvature power spectrum for those model parameter points that did *not* exhibit an extended inflationary scenario. Moreover, we will truncate the resulting curvature power spectrum at the maximum scale $k_\mathrm{max} = k_\mathrm{cl}$ (see Eq. (3.12)), since this is the scale associated to the last k-mode leaving the Hubble horizon at the end of the linear regime, and thus sub-horizon modes with $k > k_\mathrm{cl}$ should yield no contribution.

Lastly, the scalar-induced GW energy density spectrum from Eq. (1.91) is obtained from the truncated curvature power spectrum. The featured double integral is computed numerically with the `quad` integrator from `SciPy`, in which we employ a smooth interpolation of the truncated curvature power spectrum. Due to the fact that we have a discrete and upper-bounded k-interval for which we have numerical data available, we manually set the super-horizon contributions to the double integral to zero to keep the original integration boundaries of the inner integral.

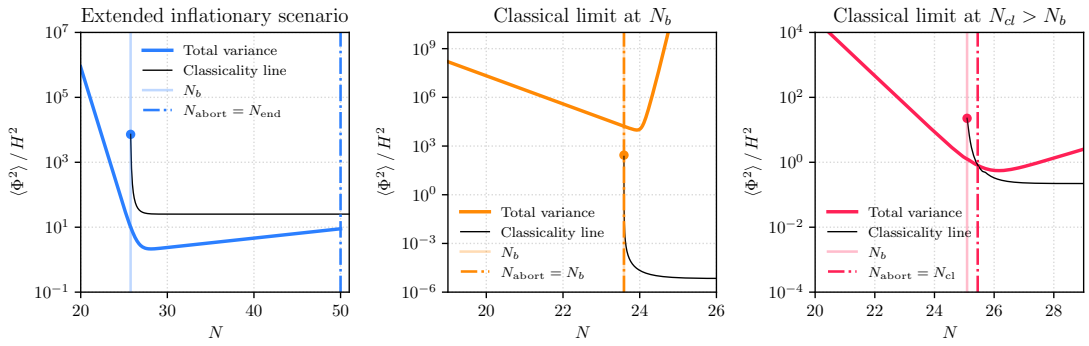

Figure 3.5: Different scenarios of the variance's evolution and the corresponding truncation criteria as described in Sec. 3.1.3. Here, note that we will use the corresponding efold numbers $N(\eta)$ for the following description of the different cases.
Left: If the total variance is *below* the classicality line for all $N \in [N_{\mathrm{start}}, N_{\mathrm{end}}]$, the simulation is aborted at N_{end} and all simulation data is to be truncated at N_{end}. In this case, we encounter an extended inflationary scenario. *Middle:* In case the total variance is *above* the classicality line for all $N \in [N_{\mathrm{start}}, N_{\mathrm{end}}]$, the simulation is to be aborted when the variance hits the maximal safety value, and the simulation data shall be truncated at N_{end}. In this case, the evolution of the scalar field has already reached the end of its linear regime at N_{b}. *Right:* If the total variance is *below* the classicality line at N_{b}, the simulation is to be aborted at $N_{\mathrm{cl}} > N_{\mathrm{b}}$, where it first crosses the classicality line again, and simulation data to be truncated at N_{cl}. This corresponds to the more interesting case where the background field dynamics have not reached the end of the linear regime yet, resulting in additional efolds of tachyonic mode amplification.

Chapter 4

Results

In this final chapter, we will present the obtained results from our study of the linear or quantum regime of the QCD-sourced tachyonic phase transition in the Classically Conformal $\mathrm{B}-\mathrm{L}$ model. We will present the scalar-induced curvature power spectrum obtained from the simulated k-mode amplitude evolutions, and the resulting GW energy density spectrum. By comparing our reslts to the Power Law Integrated Sensitivity (PLI) curves from a number of future GW observatories, we will estimate the detectability of our calculated GW spectra and therefore the ability to probe our BSM model.

4.1 Mode Amplitude & Variance Evolution

Firstly, we will discuss the characteristics of a typical variance evolution in the cases where the end of the linear regime of the background field dynamics is reached after a finite number of efolds $N_{\mathrm{b}} \leq N_{\mathrm{cl}} \ll 50$ (cf. middle and right plot in Fig. 3.5). In Fig. 4.1, we depict the evolution of comoving k-mode amplitudes together with the resulting variance evolution for the case where the linear regime end at $N_{\mathrm{b}} = N(T_{\mathrm{b}})$ (top panel) and $N_{\mathrm{cl}} > N_{\mathrm{b}}$ (bottom panel), respectively.

Generally, we observe that the variance evolution is initially dominated by its thermal contribution (see Eq. (1.152)) $\langle\Phi^2\rangle_{\mathrm{T}} \approx T^2/12$, which is rapidly decreasing due to the cooling of the universe during the inflationary period. All super-horizon k-modes maintain their oscillatory behaviour with a constant amplitude, which, when normalised by the scale factor $a(N) \propto \exp(N)$, decrease linearily in the log-log representation. As soon as the universe cools down to T_{b}, at which the tachyonic instability due to the vanishing thermal potential barrier appears, the false vacuum becomes unstable and vacuum fluctuations become (in fact more than) *simultaneously* exponentially amplified with the same growth factor $\Gamma^{\mathrm{BL}}_{\mathrm{growth}}$ (see Eq. (2.15)), which corresponds to the steep rise of the k-mode amplitudes from N_{b} onwards. This is also reflected in the steep increase of the vacuum variance contribution, which then starts to take over the dominant role in the total variance's evolution. Note that the offset between the k-mode amplitudes is given by their inverse proportionality w.r.t. k (cf. Eqs. (1.67) and (1.68)), i.e., k-modes

with smaller comoving wavenumber k (IR-modes) will have a larger initial amplitudes than those with large comoving wavenumbers k (UV-modes).

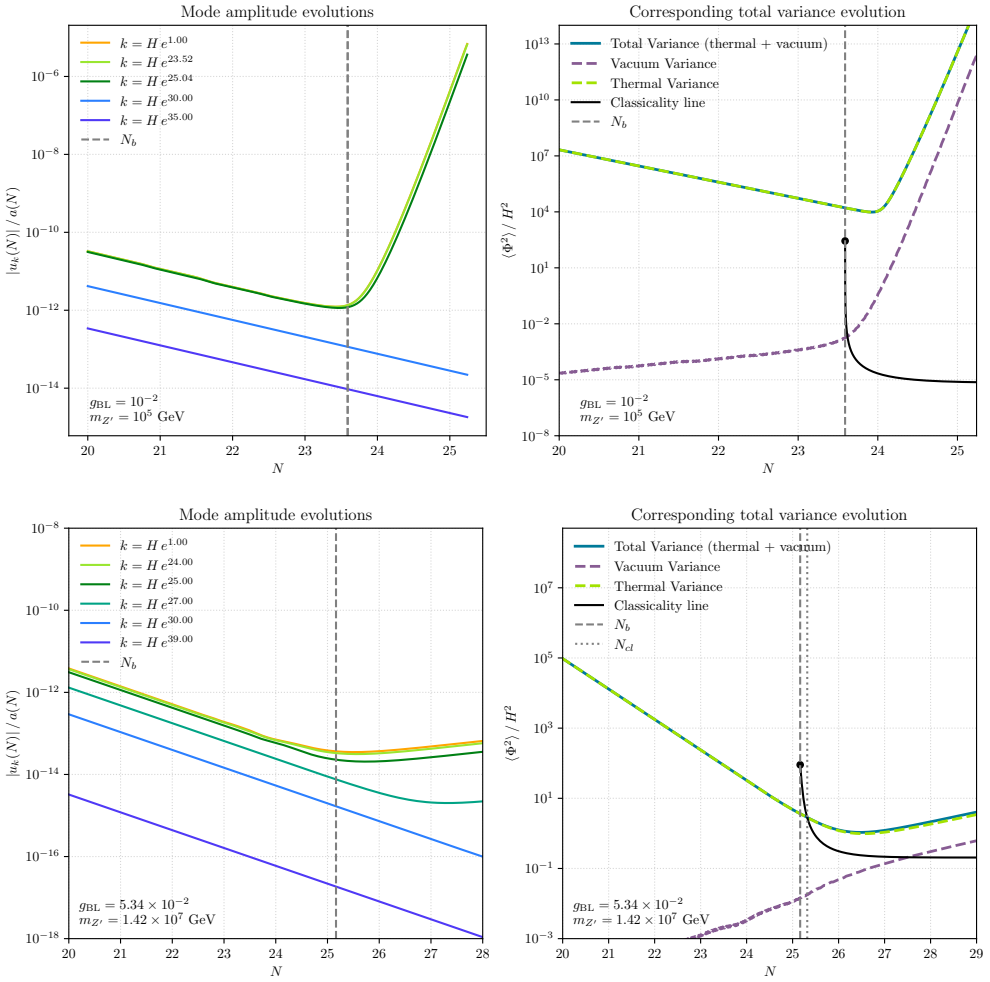

Figure 4.1: Example of the evolution of the comoving k-modes' amplitudes $|u_k(\eta)|/a(\eta)$ (*left*), and the resulting evolution of the dimensionless total variance $\langle\Phi^2\rangle/H^2$ (*right*) and its individual contributions for $g_{\rm BL} = 10^{-2}$ and $m_{\rm Z'} = 10^5$ Gev. *Top panel:* A case where the linear regime ends already at the efold number $N_{\rm b}$ associated to the tachyonic temperature $T_{\rm b}$. Note that the three lowest k-mode amplitudes lie on top of each other, since they are simultaneously amplified with the same growth rate. *Bottom panel:* Scenario in which the linear regime ends at $N_{\rm cl} > N_{\rm b}$ after the thermal potential barrier has vanished, giving the k-mode amplitudes more time to experince tachyonic growth.

In the first case where the linear regime ends already at $N_{\rm cl} = N_{\rm b}$, we see that only the comoving super-horizon k-modes with $k \leq k_{\rm b}$ become sufficiently amplified, while sub-horizon k-modes with $k > k_{\rm b}$ remain oscillatory with a constant amplitude. In the second case with $N_{\rm cl} > N_{\rm b}$, the evolution continues for a fraction of an efold, meaning that the curvature mass in the DEQ frequency has more time to become more negative such that a couple of k-modes with $k_{\rm b} < k < k_{\rm cl}$ experience tachyonic growth as well.

Model Parameter Dependence of the Evolutions We may also study how the k-mode amplitude and thus variance evolution change under a variation of the model parameters $g_{\rm BL}$ and $m_{\rm Z'}$, which is shown for two exemplary parameter point sets in Fig. 4.2. This will allows us to already learn a lot about where to find what magnitude of the generated curvature perturbations and the resulting GW energy density spectra in the tachyonic parameter subspace (cf. Fig. 2.3.1).

Generally, we would expect a model ($g_{\rm BL}$, $m_{\rm Z'}$) to generate variance evolutions more and more similar to the left plot in Fig. 3.5 as we approach the $|\Delta m_{\rm QCD}|/H \sim 1$ line in Fig. 2.3.1. In particular, this means that an increase in $m_{\rm Z'}$ will subsequently flatten out the variance evolution for $N \geq N_{\rm b}$ due to an insufficient mode amplification (cf. Eq. (2.15)), until it eventually leads to an extended inflationary scenarios featuring an almost completely flat variance for $N_{\rm b} \leq N \leq 50$. For $m_{\rm Z'} \gtrsim 10^6$ GeV, a steady decrease in $g_{\rm BL}$ should have the same effect since one then also approached the $|\Delta m_{\rm QCD}|/H \sim 1$ line. Both of these aspects can already clearly be seen in Fig. 4.2. Let us now summarize the most important conclusions from our study in Fig 4.2 with the inclusion of the results from Fig. 4.1:

Key Findings I

- The variation of $m_{\rm Z'}$ largely impacts the offset of the total variance, the efold number $N_{\rm b}$, the classical field value $\varphi(N_{\rm b})$, and the tachonic growth rate $\Gamma^{\rm BL}_{\rm growth}$.
  - Models with small $m_{\rm Z'}$-value start with a higher offset (due to a smaller Hubble parameter $\mathcal{H} \sim m^2_{\rm Z'}$), have a small $N_{\rm b}$-value, a large growth factor for tachyonic amplification (cf. Eq. (2.15)), and a small value for $\varphi_{\rm cl}(N_{\rm b})$. Their total variances show a very steep rise after $N_{\rm b}$, which corresponds to a fast growth of the k-modes and a fast end of the linear regime where the background field starts its "classically rolling" phase. Due to the fast dynamics in these specific cases, i.e., $\varphi'(\eta)$ becomes large, we expect the curvature perturbation production to be suppressed since.
  - Models with increasing $m_{\rm Z'}$ show a delayed tachyonic instability, i.e., an increase in $N_{\rm b}$, a smaller tachyonic growth factor, and larger values for $\varphi_{\rm cl}(N_{\rm b})$. The variance curve becomes less and less steep after $N_{\rm b}$ due to a slower tachyonic growth of the k-mode amplitudes. Due to the subsequent increase in $\varphi_{\rm cl}(N_{\rm b})$, we will start encountering models (cf. red line in top plot in Fig. 4.2) in which the linear regime ends only after $N_{\rm b}$, giving more k-modes more time to experience tachyonic amplification, which therefore feature an

enhanced production of curvature perturbations. Note also that the maximal super-horizon scale $k_{\rm max} = k_{\rm cl}$ also increases with $N_{\rm b}$. Followingly, these are the scenarios in which we expect the largest curvature perturbations. The physically sensible models are those where the maximum of their curvature power spectrum does not reach unity, i.e., $\max(\Delta_\zeta(k, \eta_{\rm cl})) \leq 1$. As we will see in Sec. 4.2, the actual corresponding exclusion region will extend the one found in [60] (cf. Fig. 2.3.1) to slightly smaller $m_{Z'}$-values. These excluded models typically feature extended inflationary scenarios, where the variance curve is almost completely flattened out after $N_{\rm b}$ (see e.g., the orange line in the top plot of Fig. 4.2). Physically, this means that the growing fluctuations are unable still to small to sufficiently destabilize the background field from the unstable false vacuum, and therefore cannot provide an exit out of the inflationary period.

- The variation of $g_{\rm BL}$ significantly impacts the classical field value $\varphi_{\rm cl}(N_{\rm b})$ and the tachyonic growth rate $\Gamma^{\rm BL}_{\rm growth}$, and less dominantly the value of $N_{\rm b}$.
  - Models with larger $g_{\rm BL}$-value show show an equivalent behaviour to the one explained above with with smaller $m_{Z'}$-values, namely a large tachyonic growth factor and small value for $\varphi_{\rm cl}(N_{\rm b})$, and thus fast dynamics with a quick end of the linear regime at small $N_{\rm b}$. Similarly, we expect a suppression of the curvature perturbation production for large $g_{\rm BL}$ at fixed $m_{Z'}$.
  - As $g_{\rm BL}$ decreases, we find models with similar $N_{\rm b}$-values, decreasing tachyonic growth factor and increasing value for $\varphi_{\rm cl}(T_{\rm b})$. Physically, the same happens as if we were to increase the $m_{Z'}$-value: the tachyonic growth of the k-mode amplitudes is slowed subsequently until we begin finding models with a delayed termination of the linear regime (see light solid and dash-dotted purple lines in bottom plot of Fig. 4.2) and thus enhanced curvature perturbation production. This time, however, the maximal scale $k_{\rm max} = k_{\rm cl}$ of the dimensionless curvature power spectrum is not significantly increased since $N_{\rm b} \approx$ const.. Note that this is due to the fact that a decrease in $g_{\rm BL}$ at fixed $m_{Z'}$-value equals approaching the $m/H < 1$ line in Fig. 2.3.1 or, equivalently, the new magenta $\max(\Delta_\zeta(k, \eta_{\rm cl})) = 1$ line in Fig. 4.5.

With this new knowledge at hand, we may now inspect the resulting scalar-induced dimensionless curvature power spectra and study especially their peak amplitudes.

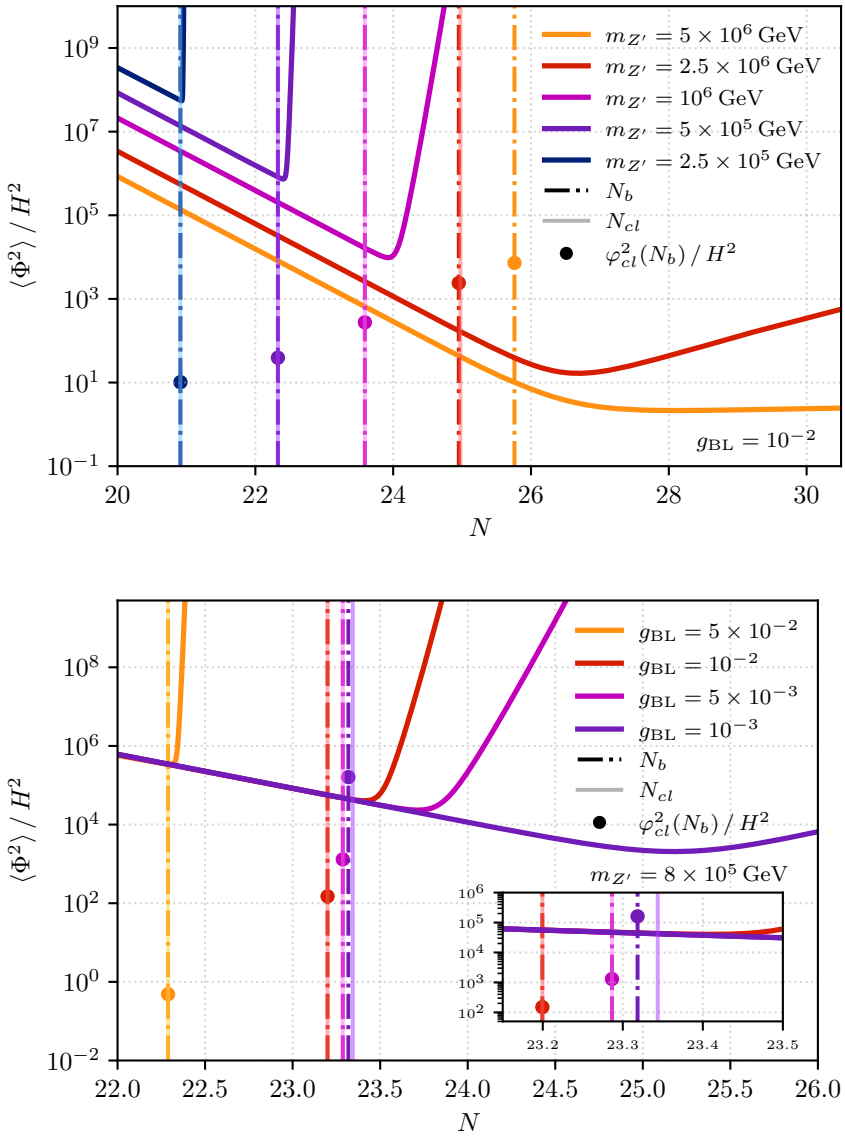

Figure 4.2: Evolution of the dimensionless total variance $\langle \Phi^2 \rangle / H^2$ under variation of the gauge boson mass $m_{Z'}$ (*top*) and the gauge coupling g_{BL} (*bottom*). Additionally, we depict the tachyonic efold number $N_{\mathrm{b}} = N(T_{\mathrm{b}})$ (*dash-dotted line*), the corresponding classical field value $\varphi_{\mathrm{cl}}(N_{\mathrm{b}})$ (*dot*), and the efold N_{cl} number where the linear regime ends (*light solid line*). The latter becomes larger than N_{b} especially for increasing g_{BL}. The offsets between the curves in the top panel are due to an increasing Hubble constant $\mathcal{H}$ with increasing $m_{Z'}$. Moreover, we expected the largest values for $\varphi_{\mathrm{cl}}(N_{\mathrm{b}})$ for large $m_{Z'}$ and g_{BL}.

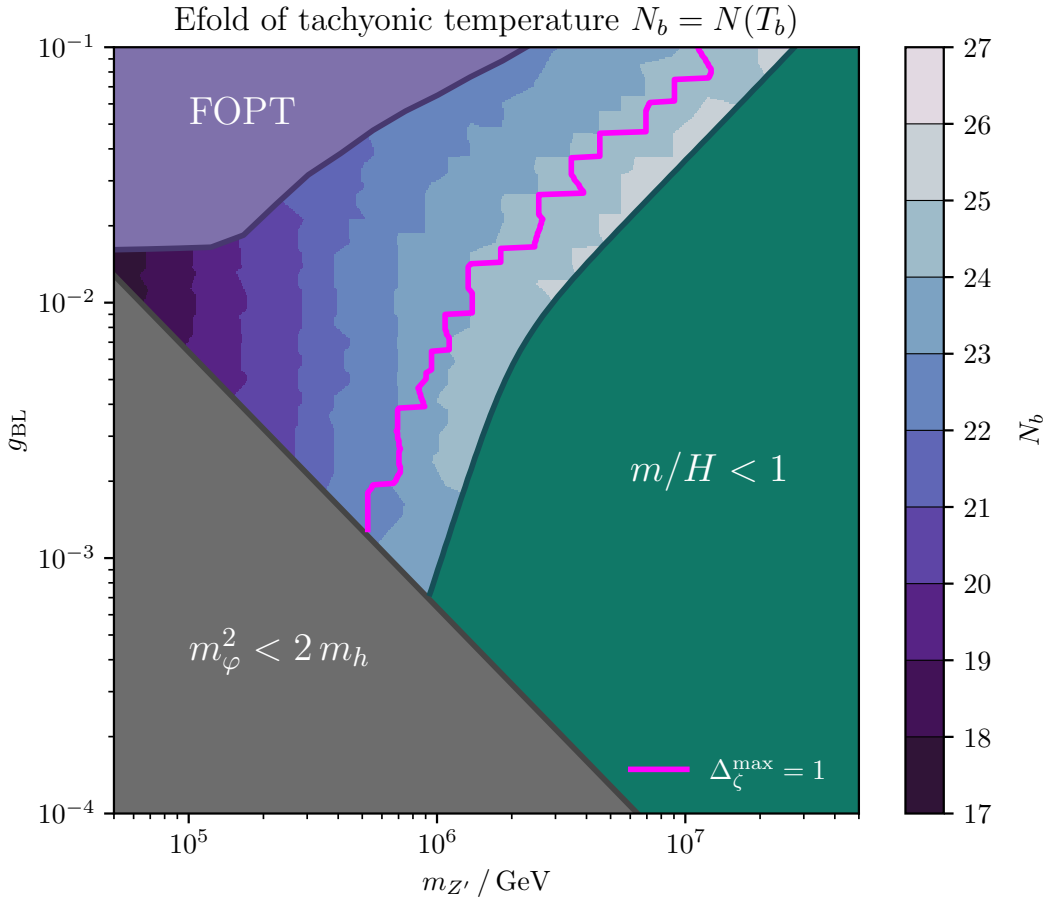

Figure 4.3: Parameter space plot showing the (interpolated) efold number $N_{\rm b}$ associated to the tachyonic temperature $T_{\rm b}$, at which the thermal potential barrier melts. An increase in $N_{\rm b}$ is mainly due to an increase in $m_{Z'}$; an increase in $g_{\rm BL}$ has only little effect on $N_{\rm b}$ in most of the non-excluded area of interest. The magenta-coloured curve is a *new* exclusion bound due to unphysically large curvature perturbations in Fig. 4.5, which extends the pre-existing $m/H < 1$ exclusion line found in [60] (cf. Fig. 2.3.1) to smaller $m_{Z'}$-values.

4.2 Curvature Power Spectrum $\Delta_\zeta(k, \eta_{\rm cl})$

Generally, the expected shape of the scalar-induced curvature power spectra in our set-up is estimated should strictly increase and peak at the maximal wavenumber scale $k_{\rm max} = k_{\rm cl}$ associated to the efold at which the linear regime has ended in the corresponding model. Now as a next step, following our preceding discussion on the total variance's evolution, we will verify our therefrom derived expectations on the model parameter dependence of the resulting scalar-induced dimensionless curvature perturbation spectra. The latter is depicted for again two benchmark parameter point sets in Fig. 4.4. The most important features are:

Key findings IIa

- As $g_{\rm BL}$ is decreased and $m_{Z'}$ is increased, we approach the $m/H < 1$ line in Fig. 2.3.1, such that we recover slower tachyonic growth of the k-mode amplitudes as well as larger values for $\varphi_{\rm cl}(N_{\rm b})$. As previously noted, we then expect the production of curvature perturbations to be enhanced, and thus larger overall values for the resulting dimensionless curvature power spectra. Naturally, we recover this prediction in the top as well as the bottom plot in Fig. 4.4.

- Additionally, we saw from Figs. 4.2 and 4.1 that an increase in $m_{Z'}$ causes an increase in $N_{\rm b}$ and followingly in $N_{\rm cl}$. This means that the maximal super-horizon wavenumber scale $k_{\rm max} = k_{\rm cl}$ is also increased. Since the smallest super-horizon wavenumber is given by the Hubble parameter $\mathcal{H} \propto m_{Z'}^2$, this results in an overall shift of the curvature power spectrum towards larger comoving wavenumbers k, or equivalently, a higher comoving frequencies $f \propto k/2\pi$. This is particular can be observed in the top plot in Fig. 4.4.

After this preliminary analysis, we performed a scan of the non-excluded part of the tachyonic parameter subspace (cf. Eq. 2.14) and computed the corresponding peak amplitudes of the curvature power spectra. This constitutes one of the main results of this work and is showcased in Fig. 4.5. We summarize:

Key findings IIb

- As predicted, the largest curvature perturbations can be found upwards along the $m/H < 1$ line from Fig. 2.3.1 for generally larger $m_{Z'}$- and $g_{\rm BL}$-values. Their peak values range over roughly 20 orders of magnitude.

- In the left corner between the FOPT and decay exclusion regions from [60], we find that curvature perturbations are clearly suppressed due to comparably fast dynamics of the background field, leading to a quick end of the linear regime. Followingly, we do not expect sizable amplitudes in the GW energy density spectra generated by the models in this parameter space region. Note that the colouring in this area appears a little irregular, which is most probably due to numerical uncertainties or issues during the simulation of the k-mode amplitude evolutions.

- Note that the upper right corner of the unconstrained tachyonic parameter subspace between the FOPT and $m/H < 1$ exclusion region contains a higher abundance of models in which the linear regime ends after $N_{\rm b}$. Consequently, we observe higher peak magnitudes in the curvature power spectra and also in the GW energy density spectra.

- Additionally, we find that the actual physically excluded line with respect to unphysically large curvature perturbations, i.e., $\max(\Delta_\zeta(k, \eta_{\rm cl})) = 1$, extends the $m/H < 1$ region towards smaller $m_{Z'}$-values whilst (approximately) preserving the original shape. This is depicted as the magenta-coloured line in Figs. 4.1, 4.5, 4.8, and 4.9.

  Estimating the unphysical curvature power spectrum exclusion line with $m/H = 1$ is strictly only valid if one assumes a slow-roll scenario and imposes the super-horizon expressions for the k-mode amplitudes. The latter are only valid way outside the Hubble horizon. Since we however include their full solution from the numerical evolution including the tachyonic amplification, this could be a potential source of the deviation from the simpler analytic BD estimate. Moreover, the thermal contribution featuring the Bose-Einstein distribution in Eq. (1.49) could also add a contribution to the latter. Eventually, a more thorough investigation regarding this is left for future work.

- In the area to the left and close to of the new magenta-coloured exclusion line, we observe a "sweet spot" band of intermediate peak values of the dimensionless curvature power spectrum, ranging roughly from 10^{-14} to 10^{-1}. This is the most interesting parameter space region with regards to sizable and potentially probable GW energy density spectra.

As we have now successfully analysed the most important features of the dimensionless curvature power spectra and the most interesting areas in the tachyonic parameter subspace of the $\mathrm{B} - \mathrm{L}$ model, we will continue with studying the resulting GW energy density spectra.

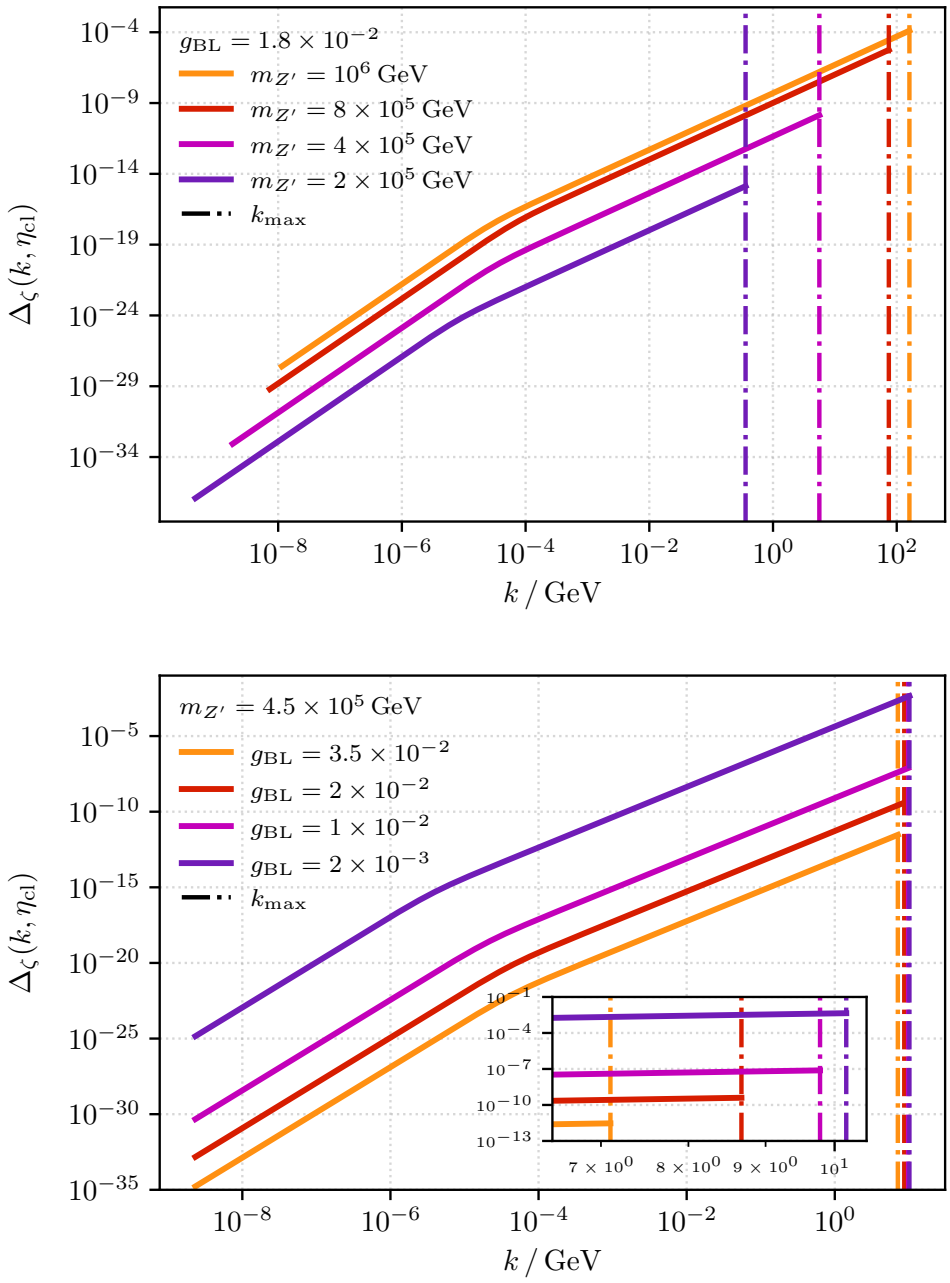

Figure 4.4: Scalar-induced dimensionless curvature power spectra $\Delta_\zeta(k, \eta_{\mathrm{cl}})$ for different gauge boson masses $m_{Z'}$ (*top*) and gauge couplings g_{BL} (*bottom*). The main takeaways are that decreasing g_{BL} and increasing $m_{Z'}$ leads to a larger peak amplitude, and mostly the increase in $m_{Z'}$ leads to a larger maximal physical cut-off wavenumber scale $k_{\mathrm{max}} = k_{\mathrm{cl}}$.

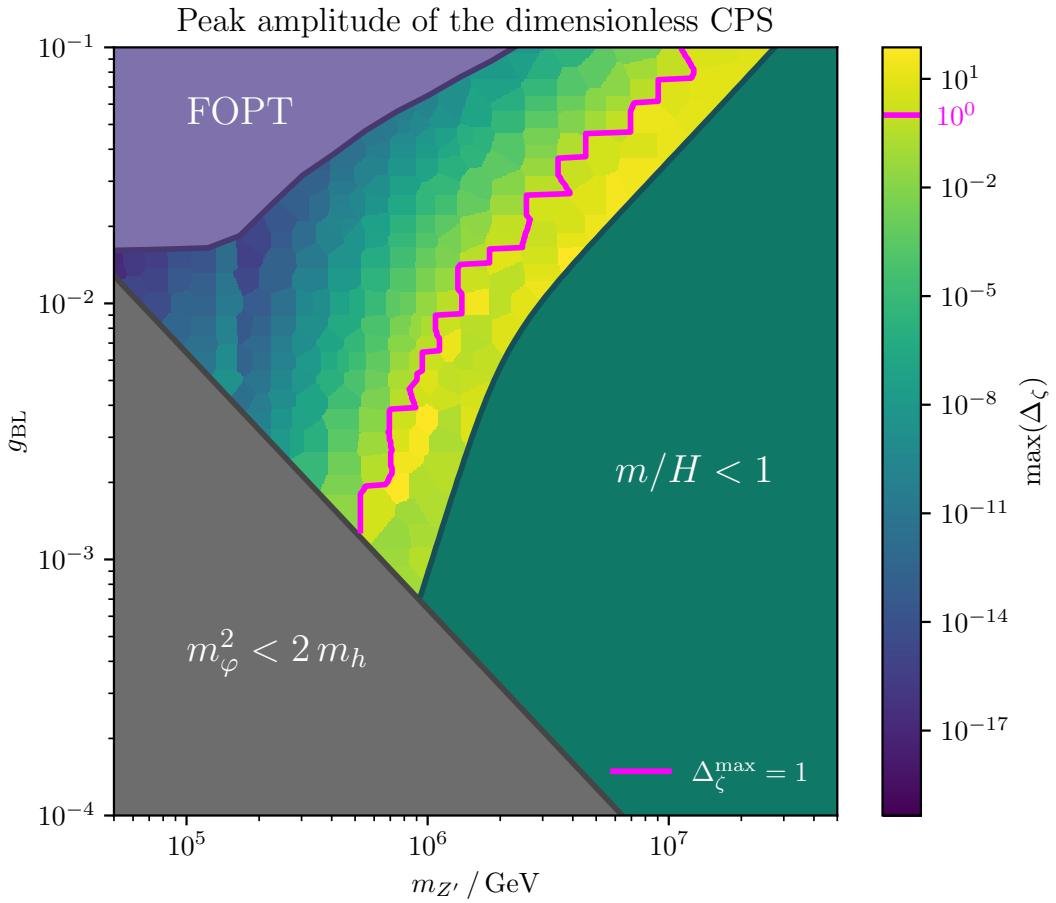

Figure 4.5: Parameter space plot showing the (interpolated) maximal amplitude of the scalar-induced dimensionless curvature power spectrum $\Delta_\zeta(\eta_{\rm cl})$, where we employed the excluded parameter space regions from [60] (cf. Fig. 2.3.1). To the right of the magenta-coloured curve, we find models with unphysically large curvature perturbation, i.e., $\max(\Delta_\zeta(\eta_{\rm cl})) \geq 1$. Note that the curve follows the shape of the pre-existing exlusion line found in [60] (cf. Fig 2.3.1) and extends the $m/H < 1$ exclusion region to slightly smaller $m_{Z'}$ values.

4.3 GW Energy Density Spectrum $h^2\Omega_{\mathrm{GW}}^{\mathrm{SI}}(f)$

As in the previous sections, we will start with a study of the resulting scalar-induced GW energy density spectra's model parameter dependence to the verification of our predictions from Sec. 4.2. The correpsonding spectra are shown in Figs. 4.6 and 4.7. Their general shape is directly related to the form of the curvature power spectra, which are linearily increasing in log-log space and cut-off at the maximum wavenumber scale k_{cl} that leaves the Hubble horizon at N_{cl} when the linear regime ends. Thus we expect the GW energy density spectrum to peak at the corresponding redshifted frequency. Shortly beyond the latter, around $k \sim 2k_{\mathrm{max}}$ due to momentum conservation, it should fall off to zero.

Furthermore, we will now also asses the ability to probe the SGWBs from our special set-up within the $\mathrm{B}-\mathrm{L}$ model by comparing the computed GW peak amplitudes and frequencies with the Power Law Integrated Sensitivity Curves (PLIs) of future GW observatories. More precisely, we will include experiments such as the Laser Interferometer Space Antenna [8], the Big Bang Observer (BBO) [69], the Deci-Hertz Interferometer Gravitational Wave Observatory (DECIGO) [70,71], the Einstein Telescope (ET) [72,73], the Square Kilometer Array (SKA) [74], and μAres [75].

Let us first gather our conclusions obtained from the first part of the analysis in this section:

Key findings IIIa

- All GW energy density spectra look as predicted via the typical model parameters scaling of the peak magnitudes and wavenumbers of the dimensionless curvature power spectra in Sec. 4.2:
  An increase in $m_{Z'}$ and g_{BL} increases the GW peak amplitude by several orders of magnitude. However, only an increase in $m_{Z'}$ can enforce a shift of the GW peak frequency towards higher frequencies within the millihertz regime. Note that the small ripples shortly before the peak amplitude are most likely due to numerical uncertainties and not of physical origin.

- As g_{BL} and $m_{Z'}$ are simultaneously increased, one ends up yet again at the upper end of the new magenta-coloured exclusion line, where we have more cases of a prolonged linear regime with enhanced tachyonic amplification. These scenarios yield the highest visbility with regards to the included GW observatories, featuring record peak amplitudes ranging roughly from $\max(h^2\Omega_{\mathrm{GW}}^{\mathrm{SI}}) \in [10^{-10}, 10^{-5}]$ (cf. Fig. 4.6 and the upper plot in Fig. 4.7).

- Models which feature a suppressed curvature perturbation production (see lower plot in Fig. 4.7) consequently show a strongly suppressed GW energy density spectrum that is out of reach of all included future GW experiments.

Following the philospophy of Sec. 4.2, we will now also conclude with a parameter space scan with regards to the GW peak amplitudes and frequencies. These are depicted

in Fig. 4.8 and Fig. 4.9, respectively.

Key findings IIIb

- The peak frequencies of all calculated GW energy density spectra range between 10^{-4} and 10^{-1}, which makes them potentially probable with μAres, LISA, BBO, and DECIGO. Note that the "sweet spot" area as denoted in Sec. 4.2 is however rather constrained to $f_{\rm peak}^{\rm GW} \in [10^{-3}, 2 \times 10^{-2}]$.
- By comparing with the the overall GW peak amplitude distribution in Fig. 4.8, we observe that the parameter points in the "sweet spot" paremeter space region, which closely follow the new magenta-coloured exclusion line, should also be within the reach of the aforementioned future GW experiments. The GW energy density spectra's visibility w.r.t. the latters increases with simultaneously increasing $g_{\rm BL}$- and $m_{Z'}$-values.
- More explicitly, this means that the SGWBs from the linear regime of the QCD-sourced tachyonic phase transition in the $\mathrm{B}-\mathrm{L}$ model are in principle detectable with a couple of future GW observatories!

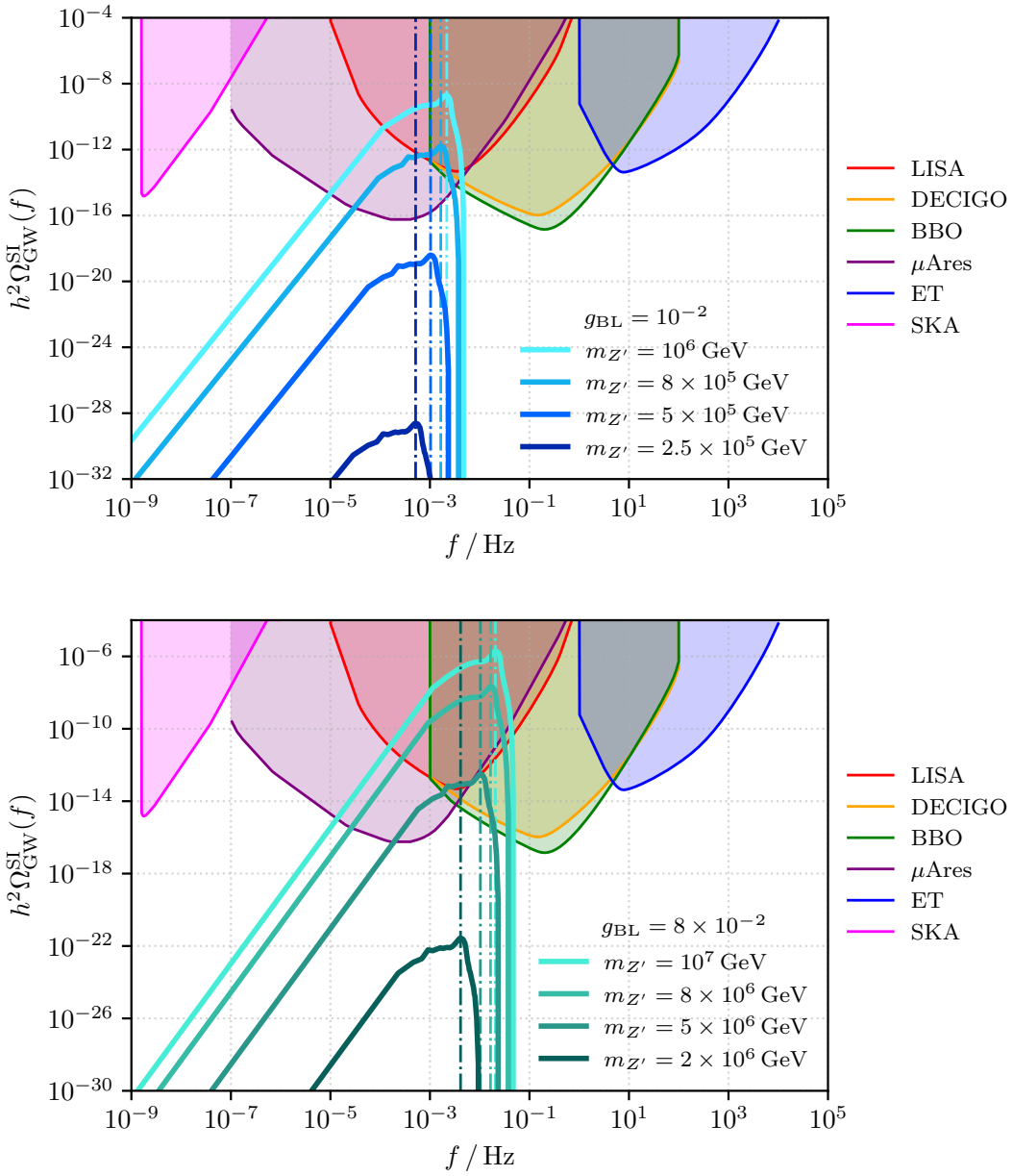

Figure 4.6: Scalar-induced GW energy density spectra $h^2\Omega_{\rm GW}^{\rm SI}(f)$ for two benchmark gauge couplings $g_{\rm BL} = 10^{-2}$ (*top*) and $g_{\rm BL} = 8 \times 10^{-2}$ (*bottom*) and varying gauge boson mass $m_{Z'}$. Evidently, an increase in $m_{Z'}$ increases the peak amplitude and peak frequency of the GW energy density spectra, which is perfectly in line with the results from the dimensionless curvature power spectra in Fig. 4.4. A simultaneous increase in $g_{\rm BL}$ shifts the peak frequencies even more towards the millihertz region, which is e.g., the design frequency band for the LISA experiment.

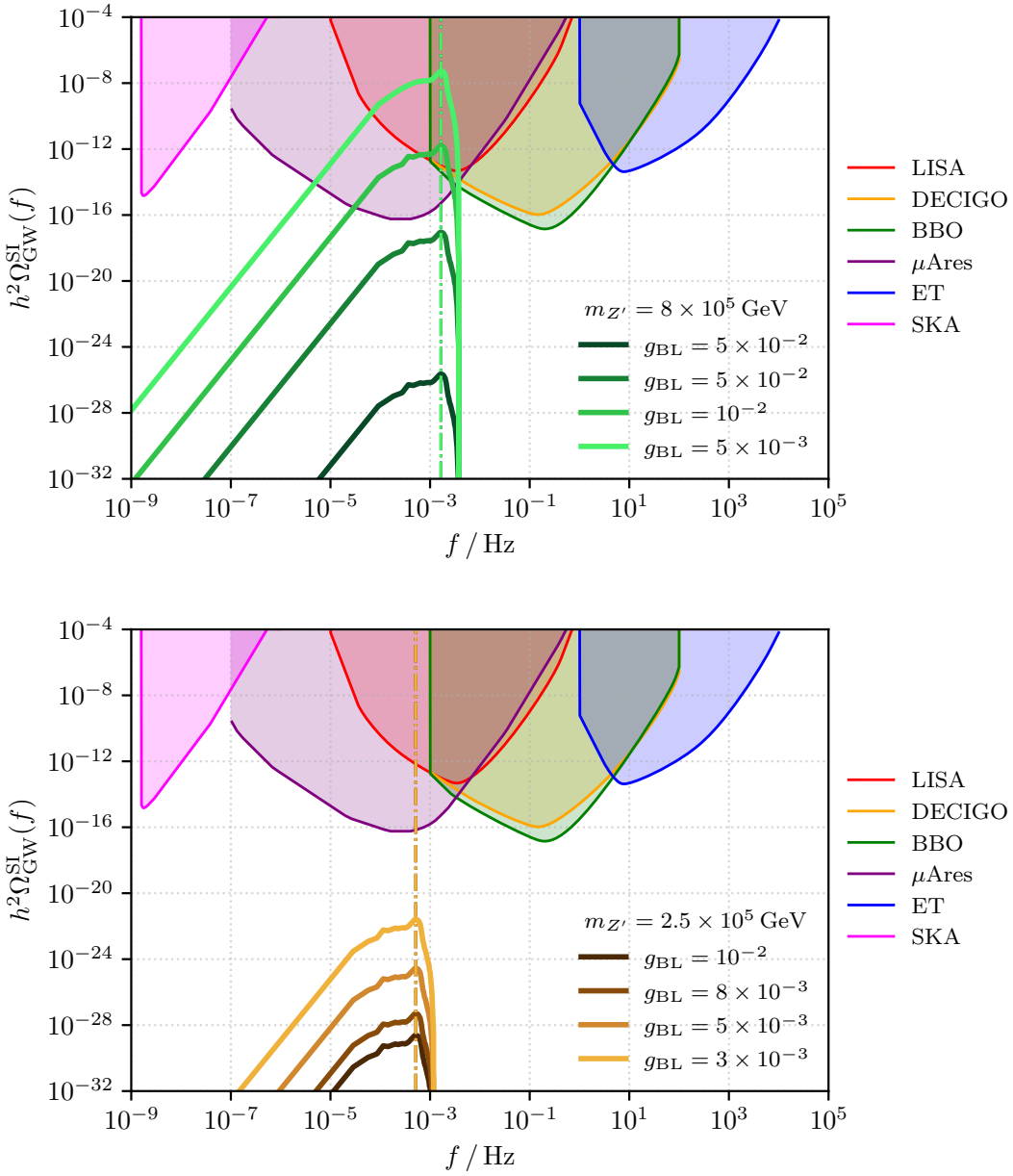

Figure 4.7: Scalar-induced GW energy density spectra $h^2\Omega_{\rm GW}^{\rm SI}(f)$ for two benchmark gauge boson masses $m_{Z'} = 8 \times 10^5\,\text{GeV}$ (*top*) and $m_{Z'} = 2.5 \times 10^5\,\text{GeV}$ (*bottom*) and varying gauge coupling $g_{\rm BL}$. An increase in $g_{\rm BL}$ increases the peak amplitude while leaving the peak frequency constant, which related to the fact that $N_{\rm b}$ and thus $N_{\rm cl}$ is mostly determined by $m_{Z'}$ rather than $g_{\rm BL}$ (cf. Fig. 4.1).

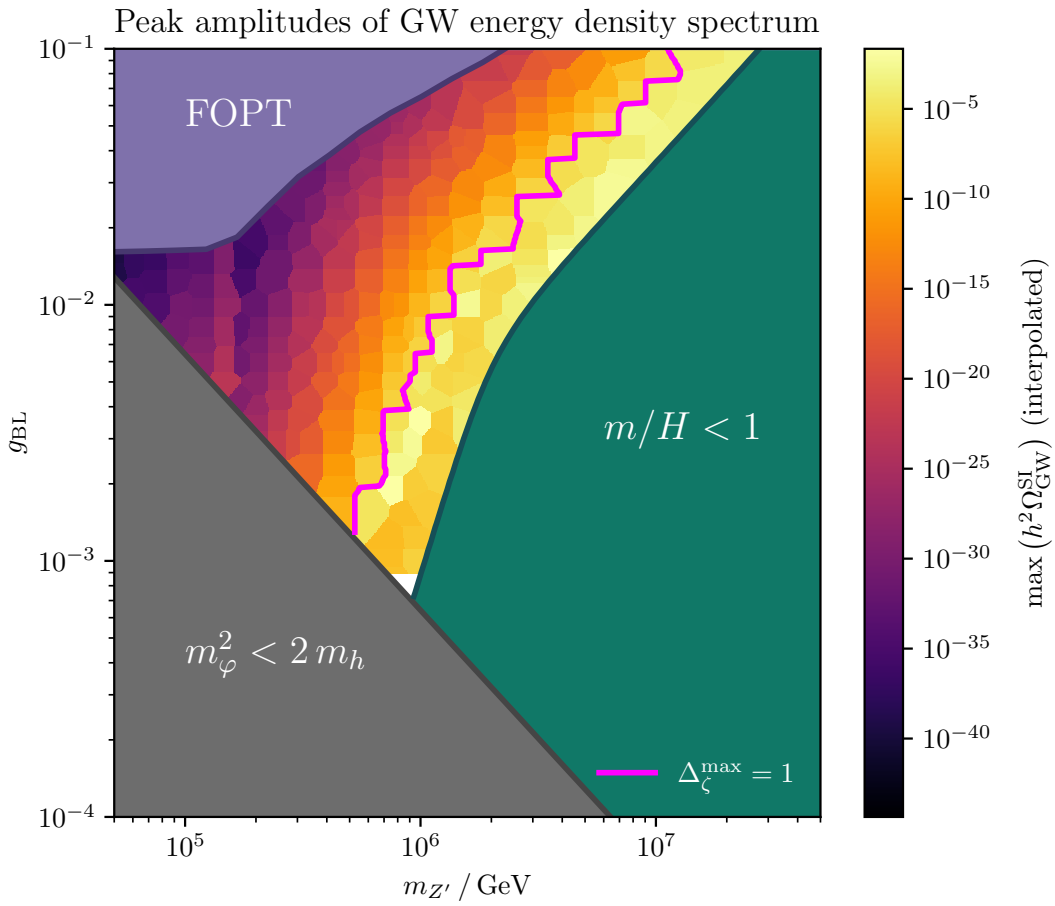

Figure 4.8: Parameter space plot showing the (interpolated) peak amplitude of the scalar-induced GW energy density spectrum $h^2\Omega_{\mathrm{GW}}^{\mathrm{SI}}$, where we employed the excluded parameter space regions from [60] (cf. Fig. 2.3.1). To the right of the pink curve, we find models with $\max(\Delta_\zeta(\eta_{\mathrm{cl}})) \geq 1$, which we exclude since they corresponds to extended inflation scenarios.

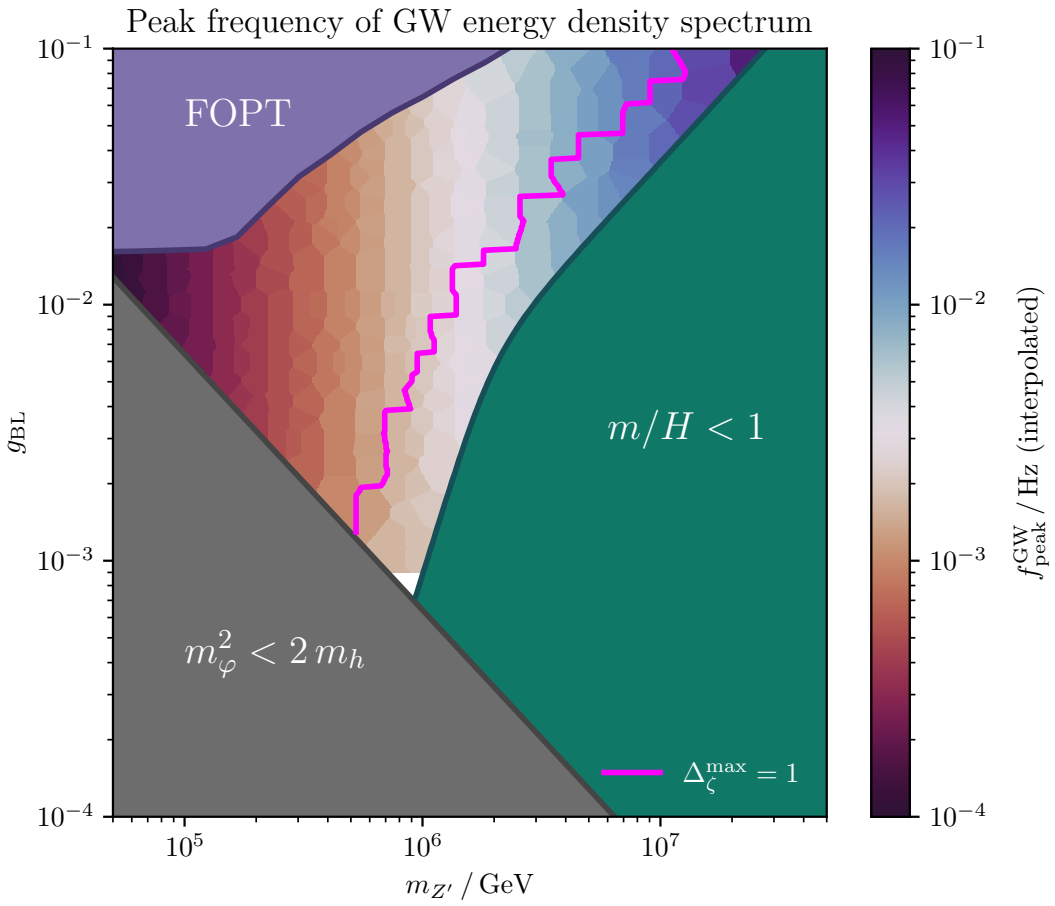

Figure 4.9: Parameter space plot showing the (interpolated) peak frequency of the scalar-induced GW energy density spectrum $h^2\Omega_{\mathrm{GW}}^{\mathrm{SI}}(f)$, where we employed the excluded parameter space regions from [60] (cf. Fig. 2.3.1). The "sweet spot" parameter space subset is located in the millihertz frequency band, which makes the SGWBs potentially probable with μAres, LISA, BBO, and DECIGO in the future.

Chapter 5

Conclusion & Outlook

In this work, we have successfully explored the linear-regime dynamics of a supercooled, QCD-sourced tachyonic phase transition in the Classically Conformal B − L SM extension. After a thorough initial code design and testing phase, we were finally able to resolve the individual k-mode amplitude evolutions throughout the tachyonic instability in the thermal inflation period. This enabled us to study the production of scalar-induced curvature perturbations and the resulting GW energy density spectra associated with SGBWs as a function of our two free model parameters: the gauge coupling g_{BL} and the gauge boson mass $m_{\mathrm{Z}'}$. Whilst scanning the allowed tachyonic parameter subspace (see Eq. (2.14)) defined by the preexisting exclusion regions from [60], we have found that curvature perturbations and thus GWs are produced in sizable amounts along in the "sweet spot" area close to the new magenta-coloured exclusion curve in Figs. 4.5 and 4.8, along which g_{BL} *and* $m_{\mathrm{Z}'}$ subsequently increase. While both model parameters can equally impact the peak amplitude of the GW energy density spectra, the corresponding peak frequency is almost exclusively controlled by $m_{\mathrm{Z}'}$. The peak frequencies of all calculated GW energy density spectra lie around the milliherzt band (cf. Fig. 4.9), i.e., $f_{\mathrm{peak}}^{\mathrm{GW}} \in [10^{-4}, 10^{-1}]$, which makes the corresponding SGWBs likely detectable with future GW observatories like μAres, LISA, BBO, and DECIGO. All models which lie very close to the magenta-coloured exclusion line should also be within the reach of the above mentioned experiments with respect to their peak GW amplitudes, which roughly range from $\max(h^2\Omega_{\mathrm{GW}}^{\mathrm{SI}}) \in [10^{-15}, 10^{-5}]$.

In the future, we would like to continue investigating this topic by complementing this work by the following aspects:

I **Accounting for post-inflationary, matter-dominated phase in parameter space:** As elaborated in Sec. (1.2.2), the expression we have used for the calculation of the present-day scalar-induced GW energy density spectrum (cf. Eq. (1.91)) is only valid in the case where our thermal inflation period is followed by a radiation-dominated era (after instantaneous reheating). However, this might be problematic for models which lie close decay constraint region in Fig. 2.3.1, since

they exhibit additional short matter-dominated phases. Thus, more research is needed in order to correctly account for the individual model's cosmological pathways in the GW energy density spectrum.

II **Going beyond the linear regime of the scalar field's background evolution:** The approach we have followed in this work only captures scalar field's dynamics until the onset of its "classical rolling" phase. It would therefore be interesting to extend the ability of the code to start simulating the background field EOM (cf. (1.54)) *together* with the *general* Mukhanov-Sasaki equation (cf. Eq. (1.61)) from $N_{\rm cl}$ onwards for a little while. At some point, we will also need to take into account the backreactions of the scalar fluctuations during the reheating period, from which we would expect another SGWB contribution from the sub-horizon k-modes via the generation of gradients in the scalar field's energy density. The latter would complement the GW energy density spectra obtained in this work at even higher wavenumbers k or frequencies f. Note, however, that the calculation of this reheating signal requires the simulations on a discretised spacetime lattice, and is therefore left for future work.

III **Estimating the primordial black hole production in our set-up:** Lastly, it should be noted that the production of sizable curvature perturbations during a thermal inflation period may also lead to the production of so-called primordial black holes [34]. The latter constitute dark matter candidates in form of macroscopic objects, whose properties are being continuously constrained by observational data [76, 77]. Including these would give us another opportunity to further constrain the $\mathrm{B}-\mathrm{L}$ parameter space.

Appendix

A The Legendre-Fenchel Transformation

Since Legendre-Fenchel transforms play a crucial role in statistical physics and therefore in equilibrium TQFT (see Secs. 1.3.1 and 1.3.4), we want to recap what effect it has on a function and how it relates to the Hemlholtz and Gibbs free energies, for example.

- **Definition of a convex function:**
  A function $f : C \subset \mathbb{R}^n \to$ is called *convex*, if for all $x, y \in C$ and $\alpha \in [0, 1]$ we have: $f(\alpha x + (1-\alpha)y) \leq \alpha f(x) + (1-\alpha)f(y)$.

Pictorially, this means that any line connecting two points on the graph $f(C)$ lies above it. Analogously, a *concave* function fulfills the opposite relation with $\geq$.

- **Definition of the Legendre-Fenchel transformation:**
  If $f(x) : \mathbb{R} \to \mathbb{R}$ is a function, the result of a Legendre-Fenchel transform (LFT) of f is a new function with

$$(f(x))^\star = f(k) = \sup_{x \in \mathbb{R}} \left[kx - f(x)\right] , \quad k = f'(x) . \tag{1}$$

  That means that with a LFT, we can find an expression of our original function in terms of its derivative. This is possible since no information is lost during the transformation operation. Note that the resulting function $f(k)$ is then *convex*, and also the latter's LFT, i.e., $(f(x))^{\star\star}$, is also *convex*. The latter is therefore also called the *convex hull* of $f(x)$. This is visualised in Fig. 1.

From Fig. 1, we learn that if the function f is non-convex on a finite interval $D = [a, b]$, then its LFT will have a corresponding non-analyticity/ discontinuous derivative at the k-value equal to the slope of the tangent to the graph $f([a, b])$. This non-analyticity then reflects in the second LFT, the convex hull of $f(x)$, as a flattened graph in the region where $f(x)$ is non-convex. With this at hand, we may now make the analogy to statistical physics and TQFT:

- The left function $f(x)$ with the non-convexity can be interpreted as the constraint quantum effective potential $U_{\text{con}}(\varphi, T) = V_{\text{eff}}(\varphi, T)$, or the Landau free energy density $g(\theta, T)$, for $T < T_{\text{c}}$. Followingly, we have $x = \varphi$ and $k = J$.

- Their LFT, namely $f(k)$, corresponds to the Helmholtz free energy density $f(J,T)$, whose derivative features a discontinuity at $k_c = J_c$. In TQFT language, this would correspond to the Euclidean connected generating functional $W[J_\varphi, T]$.
- Lastly, the convex hull of $f(x)$ can be associated to the Gibbs free energy density $g[\varphi_J, T]$, or its quantum analogue, the quantum effective potential $U(\varphi, T)$.
- We see that the quantum effective potential $U(\varphi)$ is the convex hull of the non-convex constraint quantum effective potential $V_{\text{eff}}(\varphi, T)$.

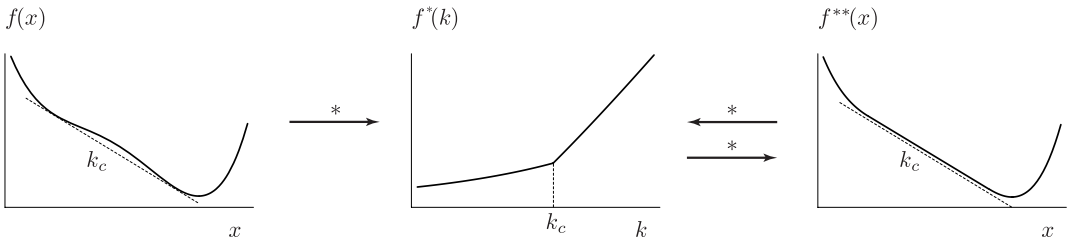

Figure 1: Visualisation of the effect of a Legendre-Fenchel transformation and its subsequent application. Here, $f(x)$ is our original function which is transformed, the resulting object $f^\star(k)$ is then a function of the derivative of f, i.e., $k = f'(x)$. Figure taken from [78].

B Simulated model parameter points $(m_{Z'}, g_{BL})$

For completion, we will lastly show all computed model parameter points in the tachyonic parameter subspace. In total, we completed 281 simulations, which have been the basis for the interpolated heatmaps in Figs. 4.1, 4.5, 4.8, and 4.9. The interpolations have been calculated using the `nearest` method of the native griddata-function of `Python`'s common plotting package `matplotlib` [79]. Some numerically unstable but also physically uninteresting points (in the yellowish region) have been removed to improve the accuracy of the interpolation. In this discrete landscape, the new magenta-coloured exclusion line has been calculated by finding the minimal $m_{Z'}$ value at which $\max(\Delta_\zeta(k, \eta_{\mathrm{cl}})) = 1$ for each computed g_{BL} line.

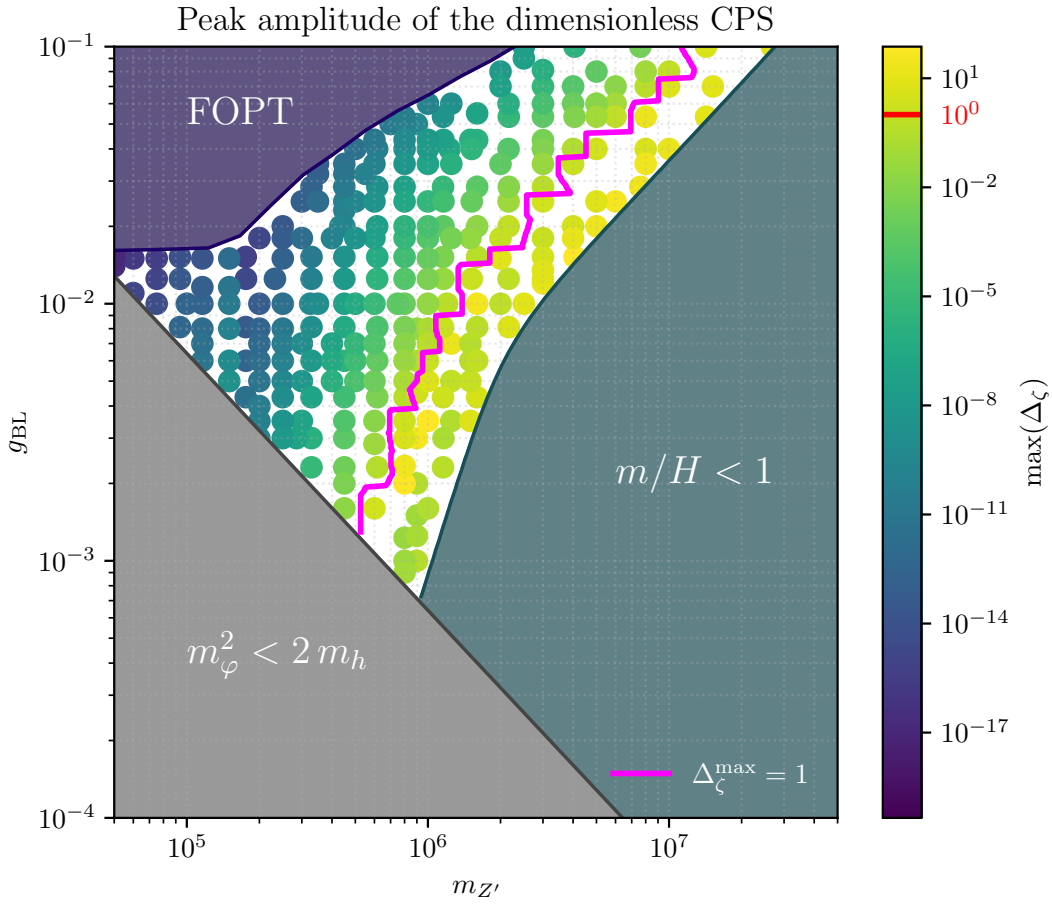

Figure 2: Overview of all simulated parameter points.

Aknowledgements

First and foremost, I dedicate this work to

my parents, Barbara & Luis,
my siblings, Sara & Nicolas,
my partner, Niklas,
and lastly, myself.

I have been blessed with the most caring, enthusiastic, and humble family one could imagine, and I am grateful for every one of you every single day. With certainty, I could not have finished this Master's degree without your constant support.

I want to thank Prof. Dr. Laura Sagunski for welcoming me in her group during my Bachelor degree and letting me continue working on topics in the fascinating field of phase transitions in the early Universe. Moreover, I thank her for continuously fostering me in many different ways, be it attending interesting conferences, workshops & schools as a very young student, organising diversity-related actions together, supporting me in pursuing career opportunities abroad, or lastly, offering me a PhD position in Frankfurt!

My second supervisor, Dr. Daniel Schmitt, has not only been a fantastic collaborator and mentor during my Bachelor's and now Master's degree, but has also been a great friend with tons of helpful advice on physics and life in general. Thank you for the many inspiring physics discussions and for giving me such an interesting research topic for my Master thesis, for enduring my everlasting and stubborn interest in convex effective potentials (I've got it now!), and lastly, for not letting me fall into any more rabbit holes before my thesis submission. You have always given me the feeling that we were equal research collaborators and that there were no stupid questions, which I value *a lot*. I am very much looking forward to continuing working with you during my PhD.

I want to thank the members of the DMGW research group, especially Yannik Schaper, Robin Diedrichs, and Jannis Simon, who have also become close friends of mine over the years we have spent together making coffee and discussing physics, among other things. Yannik, I promise I will always keep my personal computer updated and the coffee jar filled with exquisite coffee beans. Robin, I will try to keep your warm *Cheersguy* spirit alive in the group. Jannis, thank you for your open and honest manner, from which I have learned a great deal. From the befriended research group of Prof. Dr. Jürgen Schaffner-Bielich, I want to thank Sarah Louisa Pitz, Selina Kunkel, and Ishfaq Rather for being relatively new but no less amazing and supportive friends. Looking forward to invading your office on a daily basis for the best coffee in the institute!

The people who I have started studying physics with almost 8 years ago, who have accompanied me ever since, also deserve a special mention here. Many thanks go especially to Janina, Marie, and Franz, with whom I have experienced the unique ups and downs of this degree as well as of our lives in the past couple of years.

I want to thank my friends Patrick, Franca, Julie, Jemma, Carlos, Lilith, and Luise for being there for me and for getting me outside the physics bubble from time to time.

Lastly, I want to thank again Niklas Zorbach, my partner, my love, who inspires me every day and believes in me, especially when it is hard for me to do it myself. You know me better than anyone else and therefore fully understand what obtaining this degree means to me. Without your support, this would not have been possible. Your passion and unique and deep understanding of the details in physics inspire me every day to keep asking deeper and deeper questions, and led me here in the first place. I will always be grateful to you for introducing me into this world, in which one strives for the incomparable satisfaction in understanding the most basic and yet most fascinating aspects of our Universe. I love you.

See where you have gotten me now!
I am even starting a PhD!

Bibliography

[1] Albert Einstein. Näherungsweise Integration der Feldgleichungen der Gravitation. *Sitzungsber. Preuss. Akad. Wiss. Berlin (Math. Phys.)*, 1916:688–696, 1916.

[2] Albert Einstein. Über Gravitationswellen. *Sitzungsber. Preuss. Akad. Wiss. Berlin (Math. Phys.)*, 1918:154–167, 1918.

[3] LIGO Collaboration. Gw150914: The advanced ligo detectors in the era of first discoveries, 2015.

[4] George David Birkhoff and Rudolph Ernest Langer. *Relativity and Modern Physics*. Harvard University Press, 2nd edition, 1927.

[5] . The Laser Interferometer Gravitational Wave Observatory (LIGO) Collaboration. https://www.ligo.caltech.edu/page/ligo-scientific-collaboration. Accessed: 23.02.2026.

[6] . The VIRGO Collaboration. https://www.virgo-gw.eu/about/scientific-collaboration/. Accessed: 23.02.2026.

[7] . The KAGRA Collaboration. https://gwcenter.icrr.u-tokyo.ac.jp/en/about-kagra-project. Accessed: 23.02.2026.

[8] . The Laser Interferometer Space Antenna (LISA). https://www.esa.int/Science_Exploration/Space_Science/LISA. Accessed: 23.02.2026.

[9] . The North American Nanohertz Observatory for Gravitational Waves (NANOGrav). https://nanograv.org. Accessed: 23.02.2026.

[10] . The European Pulsar Timing Array (EPTA) Collaboration. https://www.epta.eu.org/goals.html. Accessed: 23.02.2026.

[11] . The African Pulsar Timing Array (APTA) Collaboration. https://africanpulsartiming.github.io. Accessed: 23.02.2026.

[12] . The Indian Pulsar Timing Array Project. https://inpta.iitr.ac.in. Accessed: 23.02.2026.

[13] . The International Pulsar Collaboration. https://inpta.iitr.ac.in. Accessed: 23.02.2026.

[14] NASA. The gravitational wave spectrum.

[15] M. Tristram, A. J. Banday, M. Douspis, X. Garrido, K. M. Górski, S. Henrot-Versillé, L. T. Hergt, S. Ilić, R. Keskitalo, G. Lagache, C. R. Lawrence, B. Partridge, and D. Scott. Cosmological parameters derived from the final Planck data release (PR4). *Astronomy & Astrophysics*, 682:A37, January 2024.

[16] Planck Collaboration. Planck 2018 results: VI. Cosmological parameters. *Astronomy & Astrophysics*, 641:A6, September 2020.

[17] Tamara Caldas Cifuentes. Gravitational wave probes of a classically conformal standard model extension. https://dmgw.space/pdfs/thesis/bachelor_thesis_tamara_caldas.pdf, 2022. Accessed: XX.02.2026.

[18] Marco Cirelli, Alessandro Strumia, and Jure Zupan. Dark matter, 2025.

[19] Douglas Clowe, Maruša Bradač, Anthony H. Gonzalez, Maxim Markevitch, Scott W. Randall, Christine Jones, and Dennis Zaritsky. A direct empirical proof of the existence of dark matter. *The Astrophysical Journal*, 648(2):L109–L113, August 2006.

[20] Vera C. Rubin and W. Kent Ford. Rotation of the andromeda nebula from a spectroscopic survey of emission regions. *The Astrophysical Journal*, 159:379–403, 1970.

[21] Peter W. Higgs. Broken Symmetries and the Masses of Gauge Bosons. *Phys. Rev. Lett.*, 13:508–509, 1964.

[22] Observation of a new particle in the search for the standard model higgs boson with the atlas detector at the lhc. *Physics Letters B*, 716(1):1–29, September 2012.

[23] Y. Aoki, G. Endrődi, Z. Fodor, S. D. Katz, and K. K. Szabó. The order of the quantum chromodynamics transition predicted by the standard model of particle physics. *Nature*, 443(7112):675–678, October 2006.

[24] K. Kajantie, M. Laine, K. Rummukainen, and Mikhail E. Shaposhnikov. Is there a hot electroweak phase transition at $m_H \gtrsim m_W$? *Phys. Rev. Lett.*, 77:2887–2890, 1996.

[25] Daniel Baumann. *Cosmology*. Cambridge University Press, 7 2022.

[26] Anson Hook, John Kearney, Bibhushan Shakya, and Kathryn M. Zurek. Probable or improbable universe? correlating electroweak vacuum instability with the scale of inflation. *Journal of High Energy Physics*, 2015(1), January 2015.

[27] V.F. Mukhanov, H.A. Feldman, and R.H. Brandenberger. Theory of cosmological perturbations. *Physics Reports*, 215(5):203–333, 1992.

[28] James M. Bardeen. Gauge Invariant Cosmological Perturbations. *Phys. Rev. D*, 22:1882–1905, 1980.

[29] T. S. Bunch and P. C. W. Davies. Quantum Field Theory in de Sitter Space: Renormalization by Point Splitting. *Proc. Roy. Soc. Lond. A*, 360:117–134, 1978.

[30] Marek Lewicki, Marco Merchand, Laura Sagunski, Philipp Schicho, and Daniel Schmitt. Impact of theoretical uncertainties on model parameter reconstruction from GW signals sourced by cosmological phase transitions. *Phys. Rev. D*, 110(2):023538, 2024.

[31] Kazunori Kohri and Takahiro Terada. Semianalytic calculation of gravitational wave spectrum nonlinearly induced from primordial curvature perturbations. *Physical Review D*, 97(12), June 2018.

[32] J.R. Espinosa, D. Racco, and A. Riotto. A cosmological signature of the sm higgs instability: gravitational waves. *Journal of Cosmology and Astroparticle Physics*, 2018(09):012–012, September 2018.

[33] Keisuke Inomata and Takahiro Terada. Gauge independence of induced gravitational waves. *Physical Review D*, 101(2), January 2020.

[34] Konstantinos Dimopoulos, Tommi Markkanen, Antonio Racioppi, and Ville Vaskonen. Primordial black holes from thermal inflation. *Journal of Cosmology and Astroparticle Physics*, 2019(07):046–046, July 2019.

[35] N. Goldenfeld. *Lectures On Phase Transitions And The Renormalization Group.* CRC Press., 1st edition, 1992.

[36] Landau, L. D. On the theory of phase transitions. *Zh. Eksp. Teor. Fiz.*, 7:19–32, 1937.

[37] Ginzburg, V. L. and Landau, L. D. On the Theory of superconductivity. *Zh. Eksp. Teor. Fiz.*, 20:1064–1082, 1950.

[38] A. S. Wightman. Quantum Field Theory in Terms of Vacuum Expectation Values. *Phys. Rev.*, 101:860–866, Jan 1956.

[39] Konrad Osterwalder and Robert Schrader. Axioms for Euclidean Green's Functions. 2. *Commun. Math. Phys.*, 42:281, 1975.

[40] Michael E. Peskin and Daniel V. Schroeder. *An Introduction to quantum field theory.* Addison-Wesley, Reading, USA, 1995.

[41] L. O'Raifeartaigh, A. Wipf, and H. Yoneyama. The constraint effective potential. *Nucl. Phys. B*, 271:653–680, 1986.

[42] Yasushi Fujimoto, Andreas Wipf, and Hiroshi Yoneyama. Symmetry Restoration of Scalar Models at Finite Temperature. *Phys. Rev. D*, 38:2625, 1988.

[43] Mikko Laine and Aleksi Vuorinen. *Basics of Thermal Field Theory*, volume 925. Springer, 2016.

[44] Sidney Coleman and Erick Weinberg. Radiative Corrections as the Origin of Spontaneous Symmetry Breaking. *Phys. Rev. D*, 7:1888–1910, Mar 1973.

[45] Andrei D. Linde. Decay of the False Vacuum at Finite Temperature. *Nucl. Phys. B*, 216:421, 1983. [Erratum: Nucl.Phys.B 223, 544 (1983)].

[46] Andrei D. Linde. Fate of the False Vacuum at Finite Temperature: Theory and Applications. *Phys. Lett. B*, 100:37–40, 1981.

[47] John Ellis, Marek Lewicki, and Ville Vaskonen. Updated predictions for gravitational waves produced in a strongly supercooled phase transition. *Journal of Cosmology and Astroparticle Physics*, 2020(11):020–020, November 2020.

[48] Arthur Kosowsky, Michael S. Turner, and Richard Watkins. Gravitational radiation from colliding vacuum bubbles. *Phys. Rev. D*, 45:4514–4535, Jun 1992.

[49] Arthur Kosowsky and Michael S. Turner. Gravitational radiation from colliding vacuum bubbles: Envelope approximation to many-bubble collisions. *Physical Review D*, 47(10):4372–4391, May 1993.

[50] Gary Felder, Juan García-Bellido, Patrick B. Greene, Lev Kofman, Andrei Linde, and Igor Tkachev. Dynamics of Symmetry Breaking and Tachyonic Preheating. *Physical Review Letters*, 87(1), June 2001.

[51] Gary N. Felder, Lev Kofman, and Andrei D. Linde. Tachyonic instability and dynamics of spontaneous symmetry breaking. *Phys. Rev. D*, 64:123517, 2001.

[52] Alexander Vilenkin. Quantum fluctuations in the new inflationary universe. *Nuclear Physics B*, 226(2):527–546, 1983.

[53] J.S Langer. Theory of spinodal decomposition in alloys. *Annals of Physics*, 65(1):53–86, 1971.

[54] John W Cahn. On spinodal decomposition. *Acta Metallurgica*, 9(9):795–801, 1961.

[55] Tomasz P. Dutka, Tae Hyun Jung, and Chang Sub Shin. What happens when supercooling is terminated by curvature flipping of the effective potential? *Journal of High Energy Physics*, 2025(5), May 2025.

[56] Planck Collaboration. Planck2018 results: X. Constraints on inflation. *Astronomy & Astrophysics*, 641:A10, September 2020.

[57] Yago Bea, Jorge Casalderrey-Solana, Thanasis Giannakopoulos, Aron Jansen, Sven Krippendorf, David Mateos, Mikel Sanchez-Garitaonandia, and Miguel Zilhão. Spinodal Gravitational Waves. *Journal of High Energy Physics*, 2025(11), November 2025.

[58] Carlos Tamarit, Wen-Yuan Ai, Juan S. Cruz, and Bjoern Garbrecht. The limits of the strong CP problem. In *Proceedings of 7th Symposium on Prospects in the Physics of Discrete Symmetries, DISCRETE 2020-2021 — PoS(DISCRETE2020-2021)*, DISCRETE2020-2021, page 084. Sissa Medialab, May 2022.

[59] Satoshi Iso, Nobuchika Okada, and Yuta Orikasa. Classically conformal B–L extended Standard Model. *Physics Letters B*, 676(1–3):81–87, June 2009.

[60] Daniel Schmitt and Laura Sagunski. QCD-sourced tachyonic phase transition in a supercooled Universe. *JCAP*, 02:075, 2025.

[61] Satoshi Iso, Pasquale D. Serpico, and Kengo Shimada. QCD-Electroweak First-Order Phase Transition in a Supercooled Universe. *Physical Review Letters*, 119(14), October 2017.

[62] K. Kajantie, M. Laine, K. Rummukainen, and Mikhail E. Shaposhnikov. Generic rules for high temperature dimensional reduction and their application to the standard model. *Nucl. Phys. B*, 458:90–136, 1996.

[63] Valentin V. Khoze, Christopher McCabe, and Gunnar Ro. Higgs vacuum stability from the dark matter portal. *Journal of High Energy Physics*, 2014(8), August 2014.

[64] Maciej Kierkla, Alexandros Karam, and Bogumiła Świeżewska. Conformal model for gravitational waves and dark matter: a status update. *Journal of High Energy Physics*, 2023(3), March 2023.

[65] M.N. Spijker. Stiffness in numerical initial-value problems. *Journal of Computational and Applied Mathematics*, 72(2):393–406, 1996.

[66] J. R. Cash. Review paper: Efficient numerical methods for the solution of stiff initial-value problems and differential algebraic equations. *Proceedings of the Royal Society A: Mathematical, Physical and Engineering Sciences*, 459(2032):797–815, 04 2003.

[67] . SciPy: Fundamental algorithms for scientific computing in Python. https://scipy.org. Accessed: 03.03.2026.

[68] Marek Lewicki, Oriol Pujolàs, and Ville Vaskonen. Escape from supercooling with or without bubbles: gravitational wave signatures. *The European Physical Journal C*, 81(9), September 2021.

[69] Jeff Crowder and Neil J. Cornish. Beyond lisa: Exploring future gravitational wave missions. *Phys. Rev. D*, 72:083005, Oct 2005.

[70] Seiji Kawamura, Masaki Ando, Naoki Seto, Shuichi Sato, Mitsuru Musha, Isao Kawano, Jun'ichi Yokoyama, Takahiro Tanaka, Kunihito Ioka, Tomotada Akutsu, Takeshi Takashima, Kazuhiro Agatsuma, Akito Araya, Naoki Aritomi, Hideki Asada, Takeshi Chiba, Satoshi Eguchi, Motohiro Enoki, Masa-Katsu Fujimoto, Ryuichi Fujita, Toshifumi Futamase, Tomohiro Harada, Kazuhiro Hayama, Yoshiaki Himemoto, Takashi Hiramatsu, Feng-Lei Hong, Mizuhiko Hosokawa, Kiyotomo Ichiki, Satoshi Ikari, Hideki Ishihara, Tomohiro Ishikawa, Yousuke Itoh, Takahiro Ito, Shoki Iwaguchi, Kiwamu Izumi, Nobuyuki Kanda, Shinya Kanemura, Fumiko Kawazoe, Shiho Kobayashi, Kazunori Kohri, Yasufumi Kojima, Keiko Kokeyama, Kei Kotake, Sachiko Kuroyanagi, Kei ichi Maeda, Shuhei Matsushita, Yuta Michimura, Taigen Morimoto, Shinji Mukohyama, Koji Nagano, Shigeo Nagano, Takeo Naito, Kouji Nakamura, Takashi Nakamura, Hiroyuki Nakano, Kenichi Nakao, Shinichi Nakasuka, Yoshinori Nakayama, Kazuhiro Nakazawa, Atsushi Nishizawa, Masashi Ohkawa, Kenichi Oohara, Norichika Sago, Motoyuki Saijo, Masaaki Sakagami, Shin ichiro Sakai, Takashi Sato, Masaru Shibata, Hisaaki Shinkai, Ayaka Shoda, Kentaro Somiya, Hajime Sotani, Ryutaro Takahashi, Hirotaka Takahashi, Takamori Akiteru, Keisuke Taniguchi, Atsushi Taruya, Kimio Tsubono, Shinji Tsujikawa, Akitoshi Ueda, Ken ichi Ueda, Izumi Watanabe, Kent Yagi, Rika Yamada, Shuichiro Yokoyama, Chul-Moon Yoo, and Zong-Hong Zhu. Current status of space gravitational wave antenna DECIGO and B-DECIGO, 2020.

[71] Seto, Naoki and Kawamura, Seiji and Nakamura, Takashi. Possibility of Direct Measurement of the Acceleration of the Universe Using 0.1 Hz Band Laser Interferometer Gravitational Wave Antenna in Space. *Physical Review Letters*, 87(22), November 2001.

[72] The Einstein Telescope Collaboration. The Science of the Einstein Telescope, 2025.

[73] . The Einstein Telescope. https://www.et-gw.eu. Accessed: 02.03.2026.

[74] Gemma Janssen, George Hobbs, Maura McLaughlin, Cees Bassa, Adam Deller, Michael Kramer, Keija Lee, Chiara Mingarelli, Pablo Rosado, Sotirios Sanidas, Alberto Sesana, Lijing Shao, Ingrid Stairs, Ben Stappers, and Joris Verbiest. Gravitational Wave Astronomy with the SKA. *PoS*, AASKA14:037, 2015.

[75] Sesana, Alberto et. al. Unveiling the gravitational universe at μ-Hz frequencies. *Exper. Astron.*, 51(3):1333–1383, 2021.

[76] Marc Oncins. Constraints on pbh as dark matter from observations: a review, 2022.

[77] Bernard Carr, Antonio J. Iovino, Gabriele Perna, Ville Vaskonen, and Hardi Veermäe. Primordial black holes: constraints, potential evidence and prospects, 2026.

[78] Hugo Touchette. The Legendre-Fenchel Transform. https://ise.ncsu.edu/wp-content/uploads/sites/9/2015/07/or706-LF-transform-1.pdf. Accessed: 01.03.2026.

[79] . Matplotlib: Visualization with Python. https://matplotlib.org. Accessed: 03.03.2026.